Cosmological consequences of interacting dark energy models

Cameron C Thomas

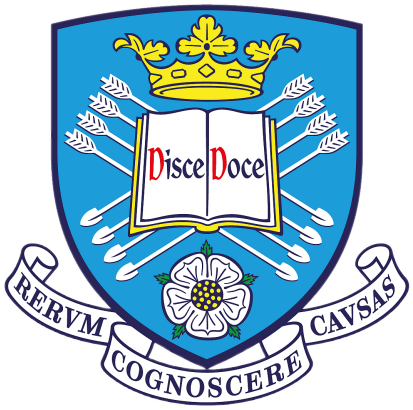

A thesis submitted for the degree of
Doctor of Philosophy

School of Mathematics and Statistics
Faculty of Science
University of Sheffield

Supervised by Professor Carsten van de Bruck

January 2023

Declaration

I hereby declare that this thesis is my own work, that this work has not been presented for an award at this or any other university, and that I have acknowledged the work of others appropriately. This thesis includes nothing which is the outcome of work done in collaboration except in chapter 4 which is based on an unpublished paper, chapter 5 which is based on [1, 2] and chapter 6 which is based on an unpublished paper. I declare that all the work presented in this thesis that has formed jointly-authored publications and unpublished papers is my own, including text and figures.

Abstract

The standard model of cosmology, ΛCDM, is in excellent agreement with almost all present-day cosmological observations, however, there are serious theoretical problems relating to its underpinnings. Moreover, some observations in recent years have caused tensions to arise in the concordance model. It is therefore natural that we look beyond the ΛCDM model and explore the consequences of such extensions.

We explore the possibility of dark energy being in the form of a quintessence scalar field and consider an interacting dark energy model whereby the minimally coupled quintessence scalar field is conformally coupled to dark matter. We explore its dynamical evolution and cosmological imprints, and then confront the model with recent cosmological data, finding that the strength of the coupling is constrained to be unappealingly small.

This naturally leads to the exploration of new forms of couplings, such as couplings with minima. We show that such a coupling can lead to a growing fifth-force in the dark sector which has been negligible until recent times, with the onset of dark energy domination. We confront this model with cosmological observations and find that background and linear perturbation level data allow for a far stronger fifth-force in comparison. We then venture into cosmology at the smaller, non-linear scale, where we expect that the effects of a growing fifth-force will be highly significant. We conclude by speculating on the role of cosmological N-body simulations in the future of cosmology and the part that growing fifth-force models may play in it.

Contents

List of Figures

List of Tables

For those who never give up hope

Acknowledgements

I would like to start by thanking Professor William Derek Collins R.I.P. and his family for providing me with this opportunity through the Derek Collins Scholarship. Without Professor Collins' generous legacy to the University, none of this would have been possible.

I would also like to thank my supervisor Professor Carsten van de Bruck who, on top of being a brilliant physicist, turns out to be a brilliant man too. My thanks further go out to Elsa and the whole CRAG team for the laughs, inspiring moments, and fruitful discussions.

Finally, I would like to thank my family and Larra, you guys have been great.

1 — Introduction

Plato once wrote that wonder is the origin of all philosophy [5], and nature in all her manifold forms and arrays can not offer one more instantaneously rapturous display than that of a starry night sky. When the sun had settled and the duties of the day had been complete, man looked up to this vast hidden world above them and pondered the existence of it all. From times of old, the rulers and higher powers of the cosmos were said to live 'out there', among the planets and stars, with the origin of our planet and very selves being thought to have its answer lying somewhere out there in the realm of the cosmos. Throughout space and time, cultural attitudes have changed and different theories have been concocted, however, what has remained constant is the undying feeling that the answers to the deepest questions in life, our existence, our origin, and our future, lie out there in the shining night sky.

Cosmology then is surely one of the most humbling ventures a seeker of wisdom can undertake, and coincidentally has some of the most profound consequences of any discipline of human endeavour, so profound that they may even appear prideful to those unaware of the deep complexity and thorough underpinnings of this most daring discipline. For cosmology claims to do nothing less than to make reasoned judgements on the very origin, history, present-day state, and future of our universe. Cosmology is therefore all-encompassing as it stretches the limits of human imagination from the beginning of time to eternity, from one end of the universe to the other, from the universe in its smallest state to its largest, and consequently requires insight from all areas of physics.

One may wonder how it is possible at all that we may make confident predic-

tions and proclamations about our universe, or provide explanations for events that happened billions of years ago, yet with a few theoretical underpinnings, such claims can be made and explanations provided. One may attack the theoretical framework of cosmology, however, one would be naive to think that such a task would be anything but mammoth, with continual rigorous testing, internal consistency, and incredible agreement with high precision present-day observations, modern cosmology has firmly established itself as a force to be reckoned with and demanding the attention of any lover of wisdom.

In this chapter we introduce a foundational pillar of cosmology and one of the greatest theoretical achievements of physics, General Relativity. We introduce the theory of General Relativity in section 1.1 and look at how it may be applied to cosmology; in section 1.2 we look at another key ingredient of modern cosmology, the hot Big Bang model, and see how together these lead to the standard model of cosmology as presented in section 1.2.3; finally, we conclude in section 1.3.

1.1 Gravity, geometry, and cosmology

The general theory of relativity, also known as General Relativity, is without a doubt one of the most beautiful and successful theories in all of modern physics. The theory of General Relativity was developed by Albert Einstein over the course of approximately eight years, starting from 1907 to finally being presented on 25 November 1915 to the Prussian Academy of Sciences [6] in the form recognised today. General Relativity is our greatest theory of gravity today, and despite over a hundred years of increasingly rigorous and precise testing, it remains unaltered and withstanding to all experiments thus far.

Like all paradigm-shifting theories, General Relativity was first met with no small amount of scepticism. Perhaps, in part, this initial scepticism was owing to the introduction of a new and complex language, differential geometry. This new language was understood by so few initially that a popular anecdote survives where one of the early supporters of the theory, Sir Arthur Eddington, in response to being told that he is one of only three people alive who actually understands

General Relativity, pauses for a long while as if troubled, and upon further questioning as to his concerned look, he replies *"I'm trying to figure out who the third person is!"* [7]. Now whether or not this conversation actually took place, one may grasp that the mathematical elegance and beauty of this strange new theory was not enough for the scientific community to accept it in place of Newton at a whim, and so it could not come without some serious observational ammunition. Indeed Einstein himself presented three tests [6] in his original paper, two of which we outline below, which could potentially falsify General Relativity.

The first test proposed was concerned with the anomalous perihelion precession of Mercury's orbit. This anomality was first pointed out as a problem for Newtonian celestial mechanics in 1859 by Urbain Le Verrier [8]. Perhaps the most plausible solution among the many offered was the existence of a hitherto undiscovered planet between Mercury and the Sun, named Vulcan after the Roman god of fire, however, no evidence for such a planet was found and the problem remained at large. A disagreement of approximately 40 arcseconds per century existed between theoretical predictions of Newtonian mechanics and observation, with no clear solution in sight. In the seminal paper of 1915, Einstein actually calculated what this perihelion shift would be under General Relativity and came up with a figure of 43 arcseconds per century, in close agreement with the observed quantity. This prediction of General Relativity has further been tested, and more recent and accurate measurements [9] report a value of 42.9799 ± 0.0009 arcseconds per century.

Again in the same 1915 paper, a second test was proposed concerned with the deflection of light by the Sun. It had been in discussion since at least the early 1800s [10] of how light may bend around a massive object under Newtonian mechanics, and a deflection angle was calculated for the Sun to be approximately 0.875 arcseconds. Einstein visited this problem, but this time with his new theory of General Relativity and found instead the deflection angle should be twice the answer given by Newtonian dynamics, that is, approximately 1.75 arcseconds. The deflection angle had not yet been measured but Sir Arthur Eddington and his collaborators [11] set to the task of measuring the deflection during the total

solar eclipse of 29 May 1919. Eddington and his team confirmed the prediction of Einstein, and Einstein, together with the theory of General Relativity, quickly became famous and well known all across the world. General Relativity became far more accepted after this result and has since stood up against more recent tests [12, 13, 14] to extraordinary accuracy, claiming its place as a pillar of modern physics.

One of the key ideas of General Relativity is that gravitation is an effect of the curvature of spacetime itself, and at the heart of General Relativity are a set of equations, often called the Einstein field equations, which intrinsically relate the geometry of spacetime to the energy and momentum content of spacetime. Before we begin introducing the mathematical framework of General Relativity, it is important to note another foundational aspect of General Relativity which is the equivalence principle. The equivalence principle, together with the search for a properly geometric theory of gravity, were key markers for Einstein in his long quest for a consistent theory of gravity [15].

The equivalence principle is often stated in three different ways according to varying degrees of conditions and restrictions imposed. The weakest form of the equivalence principle is aptly named the weak equivalence principle. One way of stating this principle is that the inertial and gravitational mass of any object are equivalent. This implies that the acceleration of a test body due to gravity is independent from the test body's mass, composition, and structure, and therefore so too is the trajectory of a test body, where here the test bodies are taken to be subject to gravity alone and not to any other additional forces. One of the consequences of the weak equivalence principle is then that the local effects of motion of test bodies subject to a gravitational field are the same as that in a frame that is being uniformly accelerated [16]. The Einstein equivalence principle takes this principle on and further states that in a laboratory that is free-falling, the results of local, non-gravitational, experiments are independent of the location and velocity of that laboratory [17], this means that one cannot infer the existence of a gravitational field through local, non-gravitational, experiments. The Einstein equivalence principle then suggests that gravity itself should be seen

as an effect of the curvature of spacetime. Finally, the most restrictive equivalence principle of the three is named the strong equivalence principle, which takes on the Einstein equivalence principle but further extends it to include gravitational local experiments as well.

So far we have seen how the need for General Relativity can arise upon consideration of the equivalence principle and the need for a geometric explanation of gravity. We now are at a point where we can introduce the mathematical framework required to express this physical theory of gravity. The language of General Relativity is differential geometry and so we will review some key definitions and results of the theory.

We begin with recalling that a type (m, n) tensor T is a multilinear map from a collection of m dual vectors and n vectors to the set of real numbers $\mathbf{R}$,

$$T = T^{\mu_1 \cdots \mu_m}{}_{\nu_1 \ldots \nu_n} \partial_{\mu_1} \otimes \cdots \otimes \partial_{\mu_m} \otimes \mathrm{d}x^{\nu_1} \otimes \cdots \otimes \mathrm{d}x^{\nu_n}, \tag{1.1}$$

where $\partial_\mu \equiv \partial/\partial x^\mu$ and $\mathrm{d}x^\nu$ are the basis of the vector space and dual vector space respectively. The coordinate transformation of a tensor T then has the following components

$$T^{\mu'_1 \cdots \mu'_m}{}_{\nu'_1 \ldots \nu'_n} = \frac{\partial x^{\mu'_1}}{\partial x^{\mu_1}} \cdots \frac{\partial x^{\mu'_m}}{\partial x^{\mu_m}} \frac{\partial x^{\nu_1}}{\partial x^{\nu'_1}} \cdots \frac{\partial x^{\nu_n}}{\partial x^{\nu'_n}} T^{\mu_1 \cdots \mu_m}{}_{\nu_1 \ldots \nu_n}, \tag{1.2}$$

where we note that the tensor product is symmetrised. Some of the operations on tensors to note include the tensor product $\otimes$ as seen in eq. (1.1), the addition and subtraction of tensors of the same type, and the contraction of a tensor. A tensor is said to be symmetric in some indicies if it is invariant under an exchange of said indices, and anti-symmetric if the sign of the tensor changes under an exchange of indices. For a type $(2, 0)$ tensor this translates to $T^{\mu\nu} = T^{\nu\mu}$ for a symmetric tensor and $T^{\mu\nu} = -T^{\nu\mu}$ for an anti-symmetric tensor.

A fundamental tensor which will appear frequently in this thesis is the metric tensor $g_{\mu\nu}$. The metric tensor plays an extremely important role in General Relativity as it supplants the flat Minkowski metric $\eta_{\mu\nu}$, as seen in Special Relativity, to now provide a metric, and thus define a line element, for a curved spacetime.

The metric tensor is a type $(0,2)$ tensor which is symmetric, has a non-zero determinant $g = |g_{\mu\nu}|$, and has an inverse $g^{\mu\nu}$ defined by $g^{\mu\nu}g_{\nu\alpha} = g_{\beta\alpha}g^{\beta\mu} = \delta^{\mu}_{\alpha}$, therefore if $g_{\mu\nu}$ is symmetric then so is its inverse $g^{\mu\nu}$. The metric tensor $g_{\mu\nu}$ may be used to raise and lower indices on tensors, as can its inverse $g^{\mu\nu}$, for example

$$T^{\mu_1\ldots\mu_m\sigma}{}_{\nu_2\ldots\nu_n} = T^{\mu_1\ldots\mu_m}{}_{\nu_1\ldots\nu_n}g^{\nu_1\sigma}. \tag{1.3}$$

As mentioned above, the metric tensor defines the line element by

$$ds^2 = g_{\mu\nu}\mathrm{d}x^{\mu}\mathrm{d}x^{\nu}. \tag{1.4}$$

Note that throughout this thesis, we will be setting the speed of light $c = 1$ and using the 'mostly positive' $(-,+,+,+)$ signature for the metric unless specified otherwise.

In order to relate vectors of tangent spaces that are close to each other, we require a 'connection', and such an object is fundamental in defining the covariant derivative, which generalises the partial derivative to a curved spacetime. The connection coefficients appear in the definition of the covariant derivative, and in General Relativity we require a torsion-free and metric compatible connection, which leads to a specific type of connection called the Christoffel connection, with the connection coefficients given by the Christoffel symbol

$$\Gamma^{\sigma}_{\mu\nu} = \frac{1}{2}g^{\sigma\rho}(\partial_{\mu}g_{\nu\rho} + \partial_{\nu}g_{\rho\mu} - \partial_{\rho}g_{\mu\nu}). \tag{1.5}$$

It is important to note that, despite its appearance, the Christoffel symbol $\Gamma^{\sigma}_{\mu\nu}$ is *not* a tensor as may be seen by applying a coordinate transformation to eq. (1.5). Note that precisely because the partial derivative ∂_{μ} acting on tensors does not transform like a tensor is the reason why we now need a covariant derivative. The covariant derivative ∇_{μ} acting on a general tensor is given by

$$\begin{aligned}\nabla_\sigma T^{\mu_1\cdots\mu_m}{}_{\nu_1\ldots\nu_n} =& \partial_\sigma T^{\mu_1\cdots\mu_m}{}_{\nu_1\ldots\nu_n} \\ &+ \Gamma^{\mu_1}_{\sigma\lambda} T^{\lambda\mu_2\ldots\mu_m}{}_{\nu_1\ldots\nu_n} + \Gamma^{\mu_2}_{\sigma\lambda} T^{\mu_1\lambda\ldots\mu_m}{}_{\nu_1\ldots\nu_n} + \cdots \\ &- \Gamma^{\lambda}_{\sigma\nu_1} T^{\mu_1\mu_2\ldots\mu_m}{}_{\lambda\nu_2\ldots\nu_n} - \Gamma^{\lambda}_{\sigma\nu_2} T^{\mu_1\mu_2\ldots\mu_m}{}_{\nu_1\lambda\ldots\nu_n} - \cdots .\end{aligned} \tag{1.6}$$

Note that we may sometimes use the comma and semicolon notation for partial and covariant derivatives, that is,

$$\partial_\sigma T^{\mu_1\cdots\mu_m}{}_{\nu_1\ldots\nu_n} \equiv T^{\mu_1\cdots\mu_m}{}_{\nu_1\ldots\nu_n,\sigma} \quad , \qquad \nabla_\sigma T^{\mu_1\cdots\mu_m}{}_{\nu_1\ldots\nu_n} \equiv T^{\mu_1\cdots\mu_m}{}_{\nu_1\ldots\nu_n;\sigma}. \tag{1.7}$$

The covariant derivative allows us to define parallel transport of a tensor T along the path $x^\mu(\lambda)$ to be

$$\frac{dx^\sigma}{d\lambda} \nabla_\sigma T^{\mu_1\cdots\mu_m}{}_{\nu_1\ldots\nu_n} = 0, \tag{1.8}$$

where λ is an affine parameter. Then, the parallel transport of the tangent vector $V^\mu = dx^\mu/d\lambda$ yields the geodesic equation

$$\frac{d^2x^\mu}{d\lambda^2} + \Gamma^\mu_{\rho\sigma} \frac{dx^\rho}{d\lambda} \frac{dx^\sigma}{d\lambda} = 0, \tag{1.9}$$

which may be seen as a generalisation of Newton's second law for a test particle with zero net force acting upon it. We are now able to introduce the Riemann tensor, which is a fundamental tensor containing all we need to know about the curvature of a manifold, coincidentally, it is this tensor that is instrumental in constructing the Einstein tensor as appears in the fundamental equations of General Relativity, the Einstein field equations.

The Riemann tensor $R^\rho{}_{\sigma\mu\nu}$ may be motivated in several ways, one of the most popular is by considering the parallel transport of a vector V^μ around a closed infinitesimal loop in curved space. This leads to the equation $(\nabla_\mu\nabla_\nu - \nabla_\nu\nabla_\mu)V^\rho = R^\rho{}_{\sigma\mu\nu}V^\sigma$ where we identify the Riemann tensor as

$$R^\rho{}_{\sigma\mu\nu} = \partial_\mu\Gamma^\rho_{\nu\sigma} - \partial_\nu\Gamma^\rho_{\mu\sigma} + \Gamma^\rho_{\mu\lambda}\Gamma^\lambda_{\nu\sigma} - \Gamma^\rho_{\nu\lambda}\Gamma^\lambda_{\mu\sigma}. \tag{1.10}$$

Note that despite eq. (1.10) containing partial derivatives of Christoffel coefficients and products of Christoffel coefficients, that is, objects that are not tensors, the Riemann tensor itself is a tensor. Further, the Riemann tensor satisfies numerous properties, the most useful of which for this discussion are

$$R_{\rho\sigma\mu\nu} = g_{\rho\lambda}R^{\lambda}_{\sigma\mu\nu}, \quad R_{\rho\sigma\mu\nu} = -R_{\sigma\rho\mu\nu}, \quad R_{\rho\sigma\mu\nu} = -R_{\rho\sigma\nu\mu}, \quad R_{\rho\sigma\mu\nu} = R_{\mu\nu\rho\sigma}, \tag{1.11}$$

and hence we see that summing up cyclic permutations of the last three indices results in the identity

$$R_{\rho\sigma\mu\nu} + R_{\rho\mu\nu\sigma} + R_{\rho\nu\sigma\mu} = 0. \tag{1.12}$$

Taking these into consideration, one may see that the Riemann tensor has 20 independent components in four dimensions. A further useful identity is the Bianchi identity which results from permutations of the covariant derivative of the Riemann tensor. It is given by

$$\nabla_{\lambda}R_{\rho\sigma\mu\nu} + \nabla_{\rho}R_{\sigma\lambda\mu\nu} + \nabla_{\sigma}R_{\lambda\rho\mu\nu} = 0. \tag{1.13}$$

We may contract the Riemann tensor to obtain the Ricci tensor given by

$$R_{\mu\nu} = R^{\lambda}{}_{\mu\lambda\nu}, \tag{1.14}$$

which is manifestly symmetric owing to the symmetries of the Riemann tensor as described above. Note that since the Ricci tensor has indices and is symmetric, it therefore has 10 independent components. We may further take the trace of the Ricci tensor to get the Ricci scalar given by

$$R = R^{\mu}{}_{\mu} = g^{\mu\nu}R_{\mu\nu}. \tag{1.15}$$

If we now contract the Bianchi identity twice (eq. (1.13)) we get

$$\nabla^{\mu}\left(R_{\mu\nu}-\frac{1}{2}Rg_{\mu\nu}\right)=0, \tag{1.16}$$

which may be stated in terms of the Einstein tensor

$$\nabla^{\mu}G_{\mu\nu}=0, \qquad G_{\mu\nu}:=R_{\mu\nu}-\frac{1}{2}Rg_{\mu\nu}, \tag{1.17}$$

where $G_{\mu\nu}$ is known as the Einstein tensor and is manifestly symmetric owing to the symmetry of the Ricci tensor and metric tensor. It is this tensor that will appear in the Einstein field equations, which tells us how the geometry of spacetime is related to the presence of energy-momentum in spacetime. On the side of the equation encapsulating the geometry of spacetime will be this Einstein tensor, whereas on the side representing the energy-momentum content of spacetime we are still in need of a tensor. Note that in the absence of energy-momentum being present, we may arrive at the vacuum field equations given by

$$G_{\mu\nu}=0. \tag{1.18}$$

Similarly to how the equations of motion may be derived through the principle of least action in classical field theory for a flat space-time, the Einstein field equations may be derived through an appropriately defined action. The action which when varied with respect to the metric yields the Einstein field equations in a vacuum is the Einstein-Hilbert action [18]

$$S_{EH}=\frac{1}{2\kappa^2}\int R\sqrt{-g}\,d^4x, \tag{1.19}$$

where $\kappa=\sqrt{8\pi G}$ with G being Newton's gravitational constant ensures that in the weak field limit Newtonian gravity is recovered. Then to derive the Einstein field equations in the presence of energy-momentum, we add an action for matter S_m with matter Lagrangian $\mathcal{L}_m$ and then vary the action with respect to the

metric as above. Consider the total action

$$S = S_{EH} + S_m = \frac{1}{2\kappa^2} \int R\sqrt{-g}\, d^4x + \int \mathcal{L}_m \sqrt{-g}\, d^4x, \tag{1.20}$$

then varying this with respect to the metric $g_{\mu\nu}$ we arrive at

$$G_{\mu\nu} = \kappa^2 T_{\mu\nu}, \tag{1.21}$$

where $T_{\mu\nu}$ is the energy-momentum tensor defined by

$$T_{\mu\nu} = \frac{-2}{\sqrt{-g}} \frac{\delta S_m}{\delta g^{\mu\nu}}. \tag{1.22}$$

Note that the twice-contracted Bianchi identity $\nabla_\mu G^{\mu\nu} = 0$ is consistent with the law of conservation of energy-momentum in curved space-time

$$\nabla_\mu T^{\mu\nu} = 0. \tag{1.23}$$

As we will discuss in more detail later, sometimes an additional constant term appears in the Einstein field equations. This constant Λ is called the cosmological constant and may be interpreted as a vacuum energy of spacetime, having originally been added in order to find a static solution to the field equations. The full action of theory then reads

$$S = \frac{1}{2\kappa^2} \int (R - 2\Lambda)\sqrt{-g}\, d^4x + \int \mathcal{L}_m \sqrt{-g}\, d^4x, \tag{1.24}$$

which upon varying with respect to the metric $g_{\mu\nu}$ gives the equations of motion known as the Einstein field equations

$$G_{\mu\nu} + \Lambda g_{\mu\nu} = \kappa^2 T_{\mu\nu}. \tag{1.25}$$

Having arrived at the field equations of General Relativity we will now look at how this beautifully elegant theory may be applied to our universe to eventually arrive at the standard model of cosmology known as the Λ cold-dark-matter

(ΛCDM) or concordance model. Naturally, this path in history found itself to be filled with theoretical aspirations confronted with observational realities, of human prejudices and philosophical objections, of extreme scepticism and rapid acceptance, and perhaps more so than any other branch of physics, since cosmology wrestles with the deepest questions of life: our origin, our place in this universe, and our future.

Ultimately, however, a scientist's quest is a quest for truth, and so whatever diverse and elaborate theories a scientist may hold to be true must be confronted with the natural world. This is a painful experience for some no doubt, but a true scientist must continually be open to new ideas of the universe even if that means discounting years of hard work, giving up on strongly held beliefs, and acknowledging that one was wrong, both publicly and privately. In the next section we will briefly overview the history of modern cosmology, remarking on keystone achievements which helped establish this discipline, and finally arrive to the standard cosmological model of present-day, the ΛCDM model.

1.2 The birth of ΛCDM

Since the time of Newton, it has been recognised that, on large enough length scales, it is the elusive force of gravity that dominates interactions, and so the problems of the largest length-scales conceivable at a given time are chiefly gravitational problems: the orbits of planets, satellites, stars, galaxies, galaxy clusters, and so on. Therefore whatever scientific theory that tries to tackle the universe as a whole must have at its heart a coherent, accurate, and consistent theory of gravity. General Relativity provided a paradigm-shift in that gravitation was no longer considered as one force among others, but an effect stemming from the very nature of spacetime itself, and so now if the different forces of the universe could be seen as players on a flat playing field, gravity went from being a player to being an effect of a now curved playing field, with the curving of the field being dependent on the players and their interactions, and hence gravity alters all the interactions that occur since they all play on the same field. To that effect,

gravity is inescapable and universal, coupling to all energy and momentum.

Therefore the birth of General Relativity is often taken as the birth of modern cosmology. It is immediately apparent that if General Relativity is valid on cosmological length scales, then the governing behaviour of our universe, past, present, and future, is determined by the field equations. Indeed not long after General Relativity was published in 1915, Einstein discussed its cosmological applications some two years afterwards in 1917 [19] where he found a solution to the field equations describing a closed and static universe. As mentioned earlier, in order to arrive at this solution Einstein had to introduce the cosmological constant Λ into the field equations which may be interpreted as a vacuum energy, whereby if matter has a decelerating effect on expansion due to gravity, then Λ has an opposite "repulsive effect" [20], the two effects cancelling each other out in Einstein's solution.

Another guiding principle of Einstein's in his development of General Relativity was Mach's principle which briefly stated is that the large-scale distribution of matter in the universe determines the local frame of reference, or that *"the inertia of one body is caused by the presence of all others"* [21], or more generally that *"local physical laws are determined by the large-scale structure of the universe"* [22]. Einstein thought that his new theory of gravitation inherently embedded this principle, especially through the introduction of Λ, whereby no static solutions could be found in a matter-free universe. Very soon after, however, Willem de Sitter [23] found a well-defined solution to the field equations for a closed universe with no matter at all present in the universe leading him to ask *"If no matter exists apart from the test body, has this inertia?"*. Later on in 1922, Kornel Lanczos [24] showed that de Sitter's closed, matter-free universe could be seen as an expanding universe through a coordinate transformation.

Then soon after, still in the year of 1922, Alexander Friedmann published a pivotal paper [25] where he derived a general solution for the field equations describing an expanding curved universe, of which the Einstein universe and de Sitter universe were special cases. Einstein thought Friedmann had made an error in his solutions, however, Friedmann corrected Einstein showing him to have

in fact made an error, and Einstein publicly withdrew his objection. Georges Lemaître, a Belgian Catholic priest, derived Friedmann's solutions independently in 1927 [26] and noted that there should exist an approximately linear relation between the recessional velocity and distance of a distant galaxy stating *"the receding velocities of extragalactic nebulae are a cosmical effect of the expansion of the Universe"* . This approximately linear relation between the recession velocity of a galaxy and its distance is known as Hubble's law after Edwin Hubble who conducted foundational measurements of distant galaxies [27, 28] and proposed such a linear relationship in 1929, unaware of Lemaître's earlier theoretical work. The constant of proportionality is known as the Hubble constant and was calculated to approximately be $500\text{kms}^{-1}\text{Mpc}^{-1}$ by Hubble [28].

Note that Einstein's initial hesitancy to accept an expanding solution was not a mere matter of personal prejudice or philosophical conviction but was in fact supported by the observational data of the time. However, with mounting theoretical evidence from work by Lemaître, Friedmann, and others, alongside observational confirmation from work by Hubble and others, many were accepting the new expanding universe model over the static model. Einstein, despite the observational evidence, was still holding to his belief in a static universe and it was only until 1930, when he was shown that such a static model is unstable by Eddington [29], that he finally accepted an expanding universe.

Einstein's first choice of an expanding model was the oscillating solution of Friedmann's, as presented in Friedmann's 1922 paper, of a matter-filled universe which is positively curved and with no cosmological constant. In 1932, Einstein and de Sitter [30] constructed a model of the universe known as the Einstein-de Sitter universe. This cosmological model went further than Friedmann's oscillating model to now have zero curvature too, resulting in a flat universe composed of matter alone. This cosmological model, the Einstein-de Sitter universe, quickly became the dominant model of cosmology up until the end of the 20th century, when observations on supernovae cast this model into serious doubt and demanded the reintroduction of the long-abandoned cosmological constant Λ, giving rise to the current standard model of cosmology, the ΛCDM model.

Solutions to the field equations naturally give rise to the question of origin and with the static universe model being superseded by an expanding universe model, questions of the age of the universe began to arise. One cosmological solution which allows for a universe that has existed for eternity, such as in the static universe model, but is able to explain the observations of Hubble and others was one sought by Eddington [31] in 1931. This describes a universe that has existed for all eternity in an pseudo-static state, but then at some point in time becomes unstable and begins to expand. This model was in fact favoured by Einstein after his conversion into believing in an expanding universe by Eddington, although he remarked to Eddington that despite this model being *"only possibility"* that *"no man would believe this"* [32].

It was in 1931 that Lemaître [33] reasoned that if the universe is expanding, and has always been expanding and cooling down, then going back in time the universe must have been more dense, hot, and contracted such that at a certain point there would exist a *"primeval atom"* with a mass equal to the total mass of the universe, which upon disintegration produces the universe. Lemaître devised a model similar to Eddington's in that there existed a stagnatory period and then expansion, however, in Lemaître's model this stagnatory period was finite, not eternal, where after the "Big Bang", a term coined by the notable steady-state proponent Fred Hoyle in 1940, the attractive force of gravity and repulsive force of Λ balanced each other out to create a stagnatory period, before Λ would take over so that the universe would continue expanding again. The notion of a genesis point or *creatio ex nihilo* no doubt raised the hairs on the backs of many a physicists neck, especially so when the chief proponent was an ordained Catholic priest; but a true lover of wisdom will go wherever the evidence leads them, and as we shall see the hot Big Bang model treads a long and weary journey before finally being accepted and adopted as part of the concordance model of present day cosmology.

In an effect to explain the uniformity of the abundances of chemical elements in stars and the origin or nucleosynthesis of the chemical elements given that the star's interior was apparently not hot enough for such production, serious

attention was paid to the hot Big Bang model. The main idea being that going back in time, temperatures and densities were higher, and so there existed a point in time hot and dense enough for the nucleosynthesis of the chemical elements to occur, such that at some point afterwards the temperature and densities will lower causing the ratio of abundances to be frozen.

The idea of tackling the problem of the origin of chemical elements through Lemaître's *"primeval atom"* was first taken seriously by Subrahmanyan Chandrasekhar and Louis Henrich in 1942 [34], however, there was a large mismatch between theoretical predictions of abundances and observations, and it wasn't until the mid to late-1940s period that George Gamow, alongside Ralph Alpher, Hans Bethe, and Robert Herman, [35, 36], conducted pioneering work that found agreement with observations, owing further credence to the existence of a hotter, denser period in earlier cosmic history. In 1948, Alpher and Herman [37] reasoned that at sufficient temperatures the universe would be radiation-dominated as opposed to matter-dominated and further that there should be remnant thermal background radiation today of around 5 Kelvin (K). And so the Big Bang model of the universe as beginning in a hot, dense state, expanding and cooling to produce chemical elements, and further expanding and cooling leaving behind a remnant cosmic background radiation began to take hold.

The key features of the Big Bang model that differentiate it from other generic expanding models are the abundance predictions of light nuclei owing to primordial nucleosynthesis in a hot, dense state and the existence of a relic background radiation detectable today of roughly 5 K. In the post-World War II period, the Big Bang model was still in its earliest stages, and despite being able to predict the abundances of chemical elements to a reasonable degree of accuracy, it was far from being the dominant model of cosmology. A more popular expanding model was proposed by Hermann Bondi, Thomas Gold and Fred Hoyle [38, 39] in 1948 called the steady-state model. In this model, the universe is expanding but instead of the universe becoming cooler and less dense with expansion, matter is created with expansion at such a rate that the overall density of the universe remains the same, thus the large structure of the universe looks the same at all

times, and thus also the universe is allowed to be infinite in age. Moreover, during the 1950s, papers by Margaret Burbidge, Geoffrey Burbidge, William Fowler, and Hoyle [40, 41] suggested that the abundance of chemical elements was possible through stellar nucleosynthesis, thus taking away the need for a earlier hot and dense phase in cosmic history. And so Big Bang cosmology was far from the most favourable model of the universe as for many, depending perhaps on religious or philosophical beliefs, an eternal universe was easier to stomach than one of finite age. That was until 1965 when Arno Penzias and Robert Wilson [42] discovered a pesky microwave signal of 3.5 ± 1.0 K no matter where they looked at in the sky with their telescope. This was quickly recognised by Robert Dicke and his group [43] to be the blackbody background radiation that Big Bang theory predicted. This led to rapid acceptance of the Big Bang model as the favoured model of the universe, forming an integral part of the concordance model of cosmology today.

1.2.1 The Friedmann-Lemaître-Robertson-Walker metric

Recalling the field equations of General Relativity (eq. (1.25)), we see that these are a complicated system of ten non-linear second order coupled partial differential equations. If we turn our attention to the left-hand side of the equation, we note that this can be fully written out in terms of the metric $g_{\mu\nu}$ and partial derivatives thereof, therefore highlighting the metric's important place as a necessary ingredient of any solution to the equations. If we wish to apply these field equations to a cosmological model, we require a metric that satisfies the various large-scale properties we observe from our universe.

One property we have seen is that the universe is expanding, so that must be included in the metric, furthermore we do not know the precise geometry of the universe so we must allow for an open, closed, or flat universe in the general case. Two more properties drawn from observational data are the homogeneity and isotropy of the universe at large enough length scales. What is meant by the universe being homogeneous is that at a given point in time the universe looks the same in any location, and what is meant by the universe being isotropic is that at a given point in time the universe looks the same in any direction.

Together these form the cosmological principle, that on large enough cosmological length scales, the universe is homogeneous and isotropic, looking approximately the same in any location or direction. The cosmological principle may also be derived from combining the Copernican principle, that we are not in a unique position in the universe, with the fact that the universe looks isotropic from Earth, thus implying that the universe is isotropic everywhere, thus implying that the universe is homogeneous everywhere too.

The cosmological principle implies a great amount of symmetry which considerably reduces the complexity of the metric from ten independent functions to only two, the scale factor $a(t)$ and curvature parameter K. Friedmann derived a solution to Einstein's field equations describing a general expanding curved universe in 1922 which Lemaître independently derived in 1927, then later on during the 1930s Howard Robertson and Arthur Walker [44, 45] proved that the solutions found by Friedmann and Lemaître are implied by a metric that is uniquely determined by the cosmological principle, proving that any spacetime geometry that is spatially homogeneous and isotropic must have a metric, known as the Friedmann-Lemaître-Robertson-Walker (FLRW) metric, of the following form

$$ds^2 = -\mathrm{d}t^2 + a^2(t)\left(\frac{\mathrm{d}r^2}{1-Kr^2} + r^2(\mathrm{d}\theta^2 + \sin^2(\theta)\mathrm{d}\phi^2)\right) \tag{1.26}$$

in comoving spherical coordinates where t is cosmic time and $\{r, \theta, \phi\}$ are the spatial spherical coordinates. Note that the comoving spatial coordinates are not time-dependent, with the scale factor $a(t)$ alone encapsulating the expansion of the universe and with its dynamics being determined by the field equations of General Relativity. One can see from this metric that the physical distance between any two points of constant comoving distance increases with time owing to the expansion of spacetime described by $a(t)$, where $a(t)$ is normalised today to $a(t_0) \equiv a_0 = 1$, with the subscript of 0 indicating a present day value for cosmic time t and scale factor $a(t)$. The spatial curvature of the three-dimensional space is quantified by the parameter K, which can be normalised to $\{+1, 0, -1\}$ through redefining the scale factor $a(t)$ and radial coordinate r, corresponding to positive, zero, and negative curvature on three-space.

An important phenomenon in an expanding FLRW universe is that photons lose energy with the expansion of the universe, scaling like $E \propto a^{-1}$ where E is the energy, and hence the wavelength of a photon grows with expansion thereby experiencing a redshift [16]. Therefore, by measuring the redshift of an object we may determine how much expansion has taken place between us and the object, and hence use redshift in our measures of time and distance. The relationship between the observed redshift of a photon at present day to the scale factor at time of emission is [16]

$$1 + z = \frac{1}{a}. \tag{1.27}$$

From the FLRW metric we may now compute the different components of the left-hand side of Einstein's field equations (eq. (1.25)) describing the geometry of spacetime, however, we have yet to specify the right-hand side $T_{\mu\nu}$ of the equation describing the energy-momentum content of spacetime. It is after an appropriate definition of $T_{\mu\nu}$, alongside specifying particular energy species, that we will arrive at the Friedmann equations and continuity equations which govern the dynamical evolution of the universe. We will then discuss how the anisotropies of the cosmic microwave background (CMB) radiation are sensitive to cosmological models, what the most important parameters in determining the anisotropies are, and how these parameters, together with parameters describing the different energy densities of the universe, make up the six parameter standard model of modern cosmology: the ΛCDM model.

1.2.2 Friedmann's equations

The large-scale homogeneity and isotropy of the universe lead to a general form of the energy-momentum tensor $T_{\mu\nu}$ that describes a perfect fluid i as

$$T^{(i)}_{\mu\nu} = (\rho_i + P_i)U_\mu U_\nu + P_i g_{\mu\nu}, \tag{1.28}$$

where ρ_i and P_i are the fluid's energy density and pressure respectively, and where U_μ is the four-velocity of the fluid. Taking the trace of the energy-momentum

tensor we find that $T^{(i)} = T^{(i)\mu}_{\ \ \mu} = -\rho_i + 3P_i$. Therefore using the FLRW metric together with the total energy-momentum tensor, found by summing up the individual energy-momentum tensors for each species i, we arrive at the Friedmann equations [25, 46], describing how the evolution of the scale factor is related to the energy content of the universe

$$H^2 = \frac{\kappa^2}{3}\rho_{\text{tot}} - \frac{K}{a^2} + \frac{\Lambda}{3} \tag{1.29}$$

$$\frac{\ddot{a}}{a} = -\frac{\kappa^2}{6}(\rho_{\text{tot}} + 3P_{\text{tot}}) + \frac{\Lambda}{3} \tag{1.30}$$

where $H \equiv \dot{a}/a$ is the Hubble parameter describing the rate of expansion, and $\rho_{\text{tot}}, P_{\text{tot}}$ are the total energy density and total pressure found by summing up over different energy species i. Furthermore, the energy conservation equation (eq. (1.23)) implies

$$\dot{\rho}_{\text{tot}} + 3H(\rho_{\text{tot}} + P_{\text{tot}}) = 0 \tag{1.31}$$

which is also known as the continuity equation. A particular species of energy i may be characterised by its equation of state w_i which is a constant describing the relationship between the pressure of a fluid and its energy density

$$P_i = w_i \rho_i, \tag{1.32}$$

and so, assuming each species i individually satisfies energy conservation, we may write the continuity equation for a particular fluid as

$$\dot{\rho}_i + 3H(1 + w_i)\rho_i = 0, \tag{1.33}$$

and solve it to find a relation between the energy density of a fluid and the scale factor

$$\rho_i \propto a^{-3(1+w_i)}. \tag{1.34}$$

Some examples of fluids which appear in many cosmological models of our universe, including the concordance model, are non-relativistic matter (m), radiation (r), and the cosmological constant (Λ). Non-relativistic, collisionless par-

ticles, known as dust or matter in cosmology, where the pressure is very small compared to energy density, are specified by a zero pressure $P_m = 0$ and so have an equation of state $w_m = 0$. This implies then that the energy density of matter scales like

$$\rho_m \propto a^{-3}, \tag{1.35}$$

which can be seen as the number density of matter particles decreasing as the universe expands. What is called radiation in cosmology refers to electromagnetic radiation *and* relativistic particles. By considering the energy-momentum tensor in terms of the electromagnetic field strength tensor $F_{\mu\nu}$

$$T^{\mu\nu}_{(r)} = F^{\mu\lambda}F^{\nu}{}_{\lambda} - \frac{1}{4}g^{\mu\nu}F^{\lambda\sigma}F_{\lambda\sigma}, \tag{1.36}$$

we may take the trace and find that $T_{(r)\mu}{}^{\mu} = 0$ which upon equating with the trace of a perfect fluid's energy-momentum tensor gives an equation of state $w_r = 1/3$. Thus the energy density of radiation scales like

$$\rho_r \propto a^{-4}, \tag{1.37}$$

and so similarly to matter, the energy density of radiation decreases with expansion however at a faster rate due to the energy lost as the radiation particles are redshifted with the expansion of the universe.

By considering the cosmological constant term in Einstein's field equations (eq. (1.25)) as a vacuum energy, it may be moved to the right hand side and written in terms of an energy-momentum tensor

$$T^{(\Lambda)}_{\mu\nu} = -\rho_\Lambda g_{\mu\nu}, \tag{1.38}$$

where $\rho_\Lambda = \Lambda/\kappa^2$, such that the trace $T^{(\Lambda)\mu}{}_{\mu} = -4\rho_\Lambda$ which upon equating with the trace of a perfect fluid yields $w_\Lambda = -1$, thus the cosmological constant is characterised by a negative pressure fluid. The energy density of the vacuum energy is then

$$\rho_\Lambda \propto a^0, \tag{1.39}$$

that is, constant. The curvature term appearing in the first Friedmann equation (eq. (1.29)) may be written in the form of a fictitious fluid, in which case $\rho_K = -3Ka^{-2}/\kappa^2 \propto a^{-2}$ and from the second Friedmann equation (eq. (1.30)) we require $\rho_K + 3P_K = 0$, giving an effective equation of state $w_K = -1/3$. The first Friedmann equation (eq. (1.29)) is often written in terms of dimensionless density parameters Ω_i which describes the ratio of the energy density of a species i to the critical energy density ρ_{crit} where

$$\rho_{\text{crit}} = \frac{3H^2}{\kappa^2}, \tag{1.40}$$

and so for a species i we have

$$\Omega_i = \frac{\rho_i}{\rho_{\text{crit}}} = \frac{\kappa^2}{3H^2}\rho_i. \tag{1.41}$$

Thus, for a universe containing radiation (r), matter (m), a cosmological constant (Λ), and curvature (K), the first Friedmann equation (eq. (1.29)) may be written as

$$\Omega_r + \Omega_m + \Omega_\Lambda + \Omega_K = 1, \tag{1.42}$$

which is also known as the constraint equation. Using the relation between the energy density and scale factor (eq. (1.34)) for a general fluid i with equation of state w_i, we may write the dimensionless density parameters Ω_i in terms of the evolution of the scale factor a giving

$$\Omega_i = \frac{\kappa^2}{3H^2}\rho_i = \left(\frac{H_0}{H}\right)^2 \Omega_{i,0} a^{-3(1+w_i)}, \tag{1.43}$$

recalling that a subscript of zero indicates the present-day value. Substituting this into the constraint equation (eq. (1.42)) we get

$$H^2 = {H_0}^2 \left(\Omega_{r,0}a^{-4} + \Omega_{m,0}a^{-3} + \Omega_{\Lambda,0} + \Omega_{K,0}a^{-2}\right), \tag{1.44}$$

giving the first Friedmann equation (eq. (1.29)) in a form frequently seen in cosmology.

Recall back to the beginning of this chapter where we noted that the Einstein-de Sitter universe was the dominant cosmological model up until the late twentieth century, which modeled the universe as having no curvature or cosmological constant Λ. One parameter of particular interest to cosmologists in addition to the expansion rate $\dot{a}$, contained in H, was the rate of change of the expansion rate, $\ddot{a}$, contained in dimensionless deceleration parameter q whose sign determines if the expansion rate is increasing or decreasing and therefore if the universe is expanding at an accelerating or decelerating rate. Note that because the prevailing cosmological model of the time predicted a decelerating universe, that is, $\ddot{a} < 0$, the deceleration parameter was defined with a minus sign such that it is positive when the expansion of the universe is decelerating. The deceleration parameter is defined by [16]

$$q \equiv -\frac{a\ddot{a}}{\dot{a}^2}, \tag{1.45}$$

which evaluated today becomes

$$q_0 = -\frac{\ddot{a}_0}{{H_0}^2}, \tag{1.46}$$

therefore the second Friedmann equation (eq. (1.29)) may be written as

$$\begin{aligned} q_0 &= \frac{1}{2} \sum_{i=r,m,\Lambda,K} \Omega_{i,0}(1+3w_i) \\ &= \Omega_{r,0} + \frac{\Omega_{m,0}}{2} - \Omega_{\Lambda,0}, \end{aligned} \tag{1.47}$$

which for the comparably negligible present-day radiation energy density $\Omega_{r,0}$ omitted may be approximated by

$$q_0 = \frac{\Omega_{m,0}}{2} - \Omega_{\Lambda,0}, \tag{1.48}$$

and so if the universe were experiencing a decelerating expansion rate at present times then $q_0 > 0$ which implies that we should see $\Omega_{\Lambda,0} < \Omega_{m,0}/2$. Note that if a particular fluid dominated the current energy budget today and the universe

were found to be accelerating in expansion $q_0 < 0$ then eq. (1.47) implies this fluid must have an equation of state $w_i < -1/3$ which would rule out matter, radiation, or curvature as the dominating energy species.

During the late 1990s, two independent collaborations, the Supernova Cosmology Project (SCP) [47] and the High-z Supernova Search Team (HZT) [48] used supernovae Type Ia (SNIa) measurements to determine the deceleration parameter q_0. Remarkably, the HZT team found that at the 2.8σ confidence level $q_0 < 0$ and further that by allowing for the existence of a cosmological constant term $\Omega_{\Lambda,0} > 0$ at the 3.0σ confidence level. Similarly the SCP team found that $0.8\Omega_{m,0} - 0.6\Omega_{\Lambda,0} \approx -0.2 \pm 0.1$ in strong support of the existence of a cosmological constant term $\Omega_{\Lambda,0} > 0$, furthermore they found at a 1σ confidence level that $\Omega_{m,0} = 0.28^{+0.09}_{-0.08}$ for a flat cosmology. These results quickly led to the acceptance of an accelerating universe and the adoption of Λ into cosmological models, further showing that we are in an era of Λ-domination which happened at redshift $z \approx 0.3$ [49] and that the universe has been in a stage of accelerated expansion since $z \approx 0.7$ [49]. Thus, Λ has secured its place in the standard model of cosmology, even appearing in the name of the concordance model, which today is known as the ΛCDM model.

1.2.3 The six parameter model

The ΛCDM model is a cosmological model of only six parameters [50], which together can explain present-day cosmological data to an extremely high degree of accuracy. Indeed, part of the success of the ΛCDM model lies in its simplicity. Two of these parameters are easily motivated, being energy densities of matter species populating the energy-momentum content of the universe, whereas the other four parameters are motivated by considering other key parameters affecting the cosmic microwave background radiation.

As we saw earlier, the energy densities appearing in the Friedmann equations (eq. (1.29), eq. (1.30)) are the radiation density Ω_r, the matter density Ω_m, the cosmological constant energy density Ω_Λ, and the curvature density Ω_K. Observational data has severely constrained Ω_K [50] such that it is now generally

assumed the universe is flat, thus the ΛCDM model considers a flat FLRW metric as its baseline model. Moreover the radiation density Ω_r, the present-day value of which is negligibly small, is determined by [51]

$$\Omega_r h^2 = \Omega_\gamma h^2 \left(1 + \frac{7}{8}\left(\frac{4}{11}\right)^{4/3} N_{\text{eff}}\right), \tag{1.49}$$

where h is the dimensionless reduced Hubble parameter defined by

$$H_0 = 100\, h\ \text{kms}^{-1}\text{Mpc}^{-1}, \tag{1.50}$$

Ω_γ is the photon energy density determined by the CMB photon temperature $T_0 = 2.7255K$ [52], and N_{eff} is the effective number of species of neutrinos where $N_{\text{eff}} = 3.046$ in the baseline model [53, 54]. Hence this leaves only considering Ω_m as a cosmological parameter, with the energy density of Λ being determined by the constraint equation (eq. (1.42)) $\Omega_\Lambda = 1 - \Omega_m - \Omega_r$. The matter energy density is approximately 30% of the total energy budget in ΛCDM cosmology [50], meaning roughly 70% of the universe's energy density is taken up by the cosmological constant. The concordance model further describes the matter sector as being composed of two chief components, baryonic matter and cold dark matter, where baryonic here means ordinary non-relativistic, collisionless, pressureless matter, and cold dark matter is non-baryonic, non-relativistic, collisionless, pressureless matter which interacts only via gravity.

Although accounting for approximately 85% of the total matter density [50], meaning roughly 25% of the total energy density of the universe, the exact nature of dark matter is still unknown, however we may still consider its effects in cosmological models and in the evolution of the universe. We denote the energy density of baryons, which take up approximately 5% of the total energy density [50], by Ω_b and of cold dark matter by Ω_{cdm}, thus we have $\Omega_m = \Omega_b + \Omega_{\text{cdm}}$. The inclusion of cold dark matter is a vital ingredient in the standard model of cosmology, hence the namesake Λ-cold-dark-matter or ΛCDM. And so we require only two energy density parameters, Ω_b and Ω_{cdm} out of the four parameters, $\{\Omega_b, \Omega_{\text{cdm}}, \Omega_r, \Omega_\Lambda\}$, to appear as independent parameters in the ΛCDM model.

Now let us look at how the other four parameters of the ΛCDM model arise when considering the greatest cosmological observational data source to date, the Cosmic Microwave Background radiation, and specifically the anisotropies therein. The CMB spectrum itself presents an almost perfect black body spectrum and has been measured to the highest degree of precision out of any black body spectrum found in the universe [55]. The anisotropies of the CMB spectrum are particularly sensitive to cosmological models and in particular to a set of four parameters which will form the remainder of the six parameter concordance model. In order to constrain the parameters of a cosmological model using the observed spectrum of CMB temperature anisotropies, we require a theory that is able to predict the theoretical spectrum of the CMB temperature anisotropies based on a set of cosmological parameters. Such a prediction is possible by considering the linear perturbation of a FLRW universe, and the evolution of the perturbations of the particular energy species therein.

Linear cosmological perturbation theory was first introduced in 1946 by Evgeny Lifshitz [56], and not too long after the unexpected discovery of the CMB in 1965, it was applied to the CMB temperature anisotropy spectrum in 1970 by James Peebles and his graduate student Jer Yu [57]. Solving the theoretical CMB temperature anisotropy power spectrum then amounts to solving a large set of coupled differential equations in an infinite Boltzmann hierarchy. The standard method [58] of solving these equations was extremely computationally expensive, often taking several days to run. However, in 1996 a new line-of-sight integral method was presented by Uros Seljak and Matias Zaldarriaga [59] which saved a considerable amount of CPU time, reducing the run time to a matter of minutes. This new approach was implemented in the `CMBFAST` [59] Boltzmann code by Seljak and Zaldarriaga and is used by the two most popular Boltzmann codes in cosmology at present, `CAMB` [60] and `CLASS` [61].

The first clear measurement of the CMB temperature anisotropy was in 1977 by George Smoot, Marc Gorenstein, and Richard Muller [62], followed by two more papers in 1979 [63, 64], however, this detection was of the dipole anisotropy caused by the peculiar motion of the Earth and not the anisotropies of smaller

scale which are caused by density fluctuations as predicted by cosmological perturbation theory. It is these smaller scale anisotropies that are of interest, and it wasn't until two decades later with the launch of the *Cosmic Background Explorer* (COBE) satellite in 1989, that in 1992 [65] anisotropies of the order 10^{-5} were reported. This breakthrough discovery resulted in COBE scientists George Smoot and John Mather being awarded the Nobel Prize in Physics in 2006 [66]. The next big breakthrough in the detection of CMB anisotropies was with the release of the *Wilkinson Microwave Anisotropy Probe* (WMAP) satellite in 2001 which reported its first results in 2003 [67, 68], and later with the release of the *Planck* [69] satellite in 2009 which presented its first results in 2013 [70]. With each release of a next generation satellite, first COBE, then WMAP, and now *Planck*, the resolutions and sensitivities of the anisotropies increased substantially, allowing cosmological models to be ever more constrained, and for the ΛCDM model to further secure its place as the standard model of cosmology.

Now that we have established that the CMB anisotropies can be theoretically predicted from cosmological models to a high degree of accuracy using publicly available codes, and that the CMB anisotropies themselves have been observationally measured to a high resolution and sensitivity thereby allowing for a tight constraining of parameters in cosmological models, let us turn our attention to the key cosmological parameters, epochs, and processes that affect the CMB anisotropy power spectrum in order to decide the minimal set of parameters to appear in the concordance model of cosmology.

Let us look at the epoch of recombination during which protons and electrons combine for the *first* time to form neutral hydrogen, and when subsequently photons decouple from matter and are able to stream freely for the first time, thus forming the CMB. At hotter temperatures in earlier times in cosmic history, photons were tightly coupled to electrons via Compton scattering and electrons were tightly coupled to protons via Coulomb scattering. As the universe expanded and temperatures cooled, the electrons began to be able to be captured by hydrogen nuclei thus recombining to form neutral hydrogen atoms. This meant that the abundance of free electrons, that is electrons not bound by atomic nuclei, be-

gan to drop significantly and hence the rate at which photons used to Compton scatter off electrons began to decrease. As the scattering rate of photons off electrons decreases there comes a time when the rate of scattering becomes less than the rate of expansion. It is during this era when photons then decouple and can for the first time freely stream, making the universe transparent, and it is these same photons that have redshifted to form the CMB as we see it today, sometimes called the CMB photons [51].

If the epoch of recombination at $z \approx 1000$ may be characterised by a deionisation of electrons as they are captured by nuclei to form neutral atoms, then a more recent epoch at $z \approx 10$ during which objects such as dwarf galaxies, quasars, and stars began to ionise neutral hydrogen may aptly be called the epoch of reionisation [51]. This reionisation created an increase in the abundance of free electrons which subsequently recoupled CMB photons with electrons, however, by that time the number density of electrons had decreased significantly and so the photon-electron Compton scattering rate did not increase to be comparable with the rate of expansion, hence the universe remained transparent. This reionisation of electrons causes a rescattering of CMB photons, leading to the suppression of anisotropies at smaller scales in the CMB temperature spectrum and hence a parameter giving a quantifiable measure of the effect of reionisation makes an excellent addition to any cosmological model seeking to use the CMB anisotropy spectrum in order to constrain the model. A parameter which successfully encapsulates the effect of reionisation is the optical depth [59] to reionisation τ_{reio} which is given by

$$\tau_{\text{reio}} := \tau(\eta_{\text{reio}}) = \int_{\eta_{\text{reio}}}^{\eta_0} a n_e X_e \sigma_T \mathrm{d}\eta, \tag{1.51}$$

where τ is the optical depth measuring the opaqueness of the universe at a time η from present-day time η_0, η is the conformal time defined by $d\eta = dt/a(t)$, a is the scale factor, n_e is the number density of electrons, X_e is the ionisation fraction of electrons, and σ_T is the Thomson cross section.

Recall that before the era of recombination, the electrons and protons were

tightly coupled through Coulomb scattering to form an electron-proton fluid, which in turn was tightly coupled to photons through Compton scattering, thus together forming a single oscillating baryon-photon fluid. This baryon-photon fluid then has an associated sound speed of [51]

$$c_s = \sqrt{\frac{1}{3(1+R)}}, \tag{1.52}$$

where $R \equiv 3\rho_b/(4\rho_\gamma)$ is a ratio of baryon to photon energy density. We can see that the sound speed is sensitive to the baryonic energy density, with an increasing baryon density decreasing the sound speed of the baryon-photon fluid. The comoving distance travelled by an acoustic wave by some time η is known as the sound horizon and is given by

$$r_s(\eta) = \int_0^\eta \mathrm{d}\eta' c_s(\eta'), \tag{1.53}$$

and so the physical sound horizon at decoupling is $d_s(\eta_{\rm dec}) = a(\eta_{\rm dec}) r_s(\eta_{\rm dec})$. We may now define the next parameter appearing in the ΛCDM model, which is the angular size of the sound horizon at decoupling

$$\theta_s = \frac{d_s(z_{\rm dec})}{D_A(z_{\rm dec})}, \tag{1.54}$$

where the angular diameter distance $D_A(t)$ is

$$D_A(t) = a(t) \int_t^{t_0} \frac{\mathrm{d}t'}{a(t')} \tag{1.55}$$

in a flat universe where $\Omega_k = 0$. The fact that θ_s contains a ratio of two parameters, one depending on pre-recombination dynamics and the other on post-recombination dynamics, makes it an excellent probe of not only matter densities, such as $\Omega_b h^2$ and $\Omega_{\rm cdm} h^2$, but also of the cosmological constant energy density Ω_Λ which dominates the late time energy density budget of the universe.

We now introduce the last two parameters in the six parameter model con-

tained in the definition of the dimensionless primordial power spectrum of the curvature perturbations

$$\Delta^2_\zeta(k) = A_s \left(\frac{k}{k_0}\right)^{n_s-1}, \tag{1.56}$$

where ζ are curvature perturbations, k is the wavenumber of perturbations, $\Delta^2_\zeta(k)$ is the dimensionless power, A_s is the amplitude of the primordial curvature power spectrum, n_s is the spectral index of this spectrum, and the pivot scale k_0 is fixed to $k_0 = 0.05\text{Mpc}^{-1}$. This spectrum describes the primordial spectrum of density perturbations, most typically thought to be set by inflation, which seeded and provided the initial conditions for large scale structure, such as stars and galaxies, in the universe. These primordial fluctuations leave signatures in the anisotropies of the CMB temperature and polarisation spectrum and hence the amplitude of the primordial power spectrum A_s and spectral index of scalar perturbations n_s can be constrained through CMB as measured, for example, by *Planck* [50]. The baseline ΛCDM model is therefore a cosmological model of only six parameters, this set of parameters being $\{\Omega_b h^2, \Omega_{\text{cdm}} h^2, \theta_s, \tau_{\text{reio}}, n_s, A_s\}$.

1.3 Conclusions

In this chapter we introduced the greatest theory of gravity to date, General Relativity, and its applications to cosmology. We then looked at how the hot Big Bang model emerged and was adopted as part of the standard model owing to its theoretical consistency and predictions of the abundance of light nuclei and remnant radiation left over from an earlier era, the Cosmic Microwave Background radiation. We also saw how the cosmological principle leads to the Friedmann-Lemaître-Robertson-Walker metric and looked at some of the implications of this for a universe filled by radiation, baryons, cold dark matter, curvature, and a cosmological constant. Finally we gathered this all together and, upon consideration of the CMB anisotropy spectrum, saw how the six parameter ΛCDM model emerges.

The ΛCDM model is a triumph of modern science, akin to the standard model

of particle physics, however, like the standard model of particle physics, there are some issues which cannot be overlooked and have lead many cosmologists to search beyond the ΛCDM model for an explanation. In the next chapter we will look at some of the issues of ΛCDM cosmology and see if any can be better explained in an extended framework.

2 — Beyond the ΛCDM model

Before we begin exploring some of the problems in the standard model of cosmology, let us first note its triumphs and astounding concordance with present-day state of the art observational data. With only six parameters, the ΛCDM model can explain a whole wealth of current observational data to extraordinary precision [50], and, with the exception of some notable data sources [71, 72, 73, 74, 75], is consistent with all cosmological observations thus far. What we mean by consistent here is that the parameter constraints coming from independent data sets agree with one another, or put another way, the allowed parameter values inferred from differing data sets are not in *tension* with one another. Furthermore, statistical model selection and data analysis in general finds no preference for extensions to the baseline, flat, six-parameter ΛCDM model [76, 77]. If ΛCDM is extended by allowing for curvature and for the cosmological constant term to be replaced by a general fluid with equation of state w, then data analysis using CMB, baryon acoustic oscillations (BAO), and supernovae type Ia (SNIa) data favours a cosmological model which is consistent with a flat universe, $\Omega_{K,0} = 0.001 \pm 0.002$ and a cosmological constant $w = -1.03 \pm 0.03$ [50], that is, the ΛCDM model.

The concordance model does have some issues, however, and these issues have led cosmologists to look for extensions to the standard model of cosmology in order to resolve them. We will first look at some problems associated with the hot Big Bang model in section 2.1 and then look problems within the ΛCDM model. In particular, we will look at tensions in the concordance model in section 2.2 and then problems surrounding the enigmatic cosmological constant term Λ in section 2.3, finally concluding in section 2.4.

2.1 Problems in standard Big Bang cosmology

As we have previously noted, current observations [50] are consistent with our universe being flat, that is, that $\Omega_{K,0}$ is very close to zero. This in fact creates a problem for the standard Big Bang model and it was first recognised as a major problem by the great Robert Dicke in 1969 [78]. The essence of the problem lies with that fact that the curvature density parameter $|\Omega_K|$ grows with time in a matter or radiation dominated universe, and so if we were to measure the curvature density parameter today we should expect it to be a large number, however, the present-day value of the curvature density parameter, $|\Omega_{K,0}|$, is very close to zero which means that it must have been far closer to zero in early cosmic history, presenting a serious case of fine-tuning. We can quantify the level of fine-tuning required by considering the definition of Ω_K (eq. (1.41)) together with the Friedmann equation (eq. (1.44)) and constraint equation (eq. (1.42)) for a universe dominated by an energy species i yielding

$$\Omega_K(z) = \frac{\Omega_{K,0}}{(1-\Omega_{K,0})\,(1+z)^{1+3w_i} + \Omega_{K,0}}. \tag{2.1}$$

So if we make a relaxed requirement of $|\Omega_{K,0}| < 0.1$, then this requires that $|\Omega_K(z_{\rm BBN})| \lesssim 10^{-11}$ at Big Bang nucleosynthesis using $z_{\rm BBN} \sim 10^{10}$, therefore an astonishing amount of fine-tuning in the initial conditions of Ω_K is required. This fine-tuning issue creates a serious problem for standard Big Bang cosmology and it gained the name of the flatness problem.

Another problem of fine-tuning arises when we consider the CMB. The CMB we observe today appears to be homogeneous and isotropic across regions that could never have interacted, in fact, the entire CMB appears to be homogeneous and isotropic. What we should expect to see when we look at the CMB is several smaller regions that are locally homogeneous and isotropic, but not that these independent regions should be homogeneous and isotropic with each other, since these regions have never interacted and therefore should look quite different to one

another. That is, of course, unless we impose a tremendous amount of fine-tuning that requires these causally disconnected regions to have the same exact initial conditions and so despite them evolving independently, they all look the same to one another. We can explore this problem at a deeper level by introducing the concept of a particle horizon. The idea of a particle horizon is that since there has been a finite amount of time since the universe began, then there exists a finite amount of distance that a photon could have travelled from the beginning up until some later arbitrary point in time. We may therefore define the particle horizon to be

$$d_{\rm hor}(a) = a \int_0^a \frac{da'}{a'^2 H(a')}, \tag{2.2}$$

which for a universe dominated by an energy species i becomes

$$d_{\rm hor}(a) \sim a^{3(1+w_i)/2}, \tag{2.3}$$

which we note grows faster than the physical distance between comoving objects for a universe dominated by an energy species with $w_i > -1/3$, such as in a radiation-dominated $w_r = 1/3$ or matter-dominated $w_m = 0$ universe, and therefore two regions which are causally disconnected at some point in time must have been causally disconnected at all points in time earlier in a radiation or matter dominated universe. We can calculate the particle horizon at the time of decoupling to be $d_{\rm hor}(a_{\rm dec}) \approx 0.3\,{\rm Mpc}$ for $a_{dec} \sim 10^{-3}$ which implies that regions in the sky separated by an angle of more than $\theta \approx 2^\circ$ could not have interacted before decoupling and hence should not be homogeneous and isotropic with each other [51]. The fact that we do see such homogeneity and isotropy in the CMB therefore amounts to another grave problem for the Big Bang model, known as the horizon problem.

In an attempt to find an answer to these problems, a tactful solution was proposed whereby both problems are solved if the universe undergoes a period of cosmic inflation before the radiation-dominated era of cosmic history. Not only does inflation solve the flatness and horizon problems that standard Big Bang cosmology presents, but inflation also provides an explanation for the initial

inhomogeneities which seeded large scale structure in the universe, as briefly mentioned in section 1.2.3, as tiny quantum fluctuations in the early universe.

In 1979, Alan Guth was trying to solve the magnetic monopole problem that arises in many Grand Unified Theories. The problem is that many Grand Unified Theories propose the production of magnetic monopoles at a density that far exceeds the amount observed in our universe, which is none as of present [79, 80]. He noted [81] that if the universe expanded at an accelerating rate, then the density of magnetic monopoles could be sufficiently diluted in our universe such that it is likely none would be detected. He quickly realised, however, that if the universe underwent a period of accelerated expansion, or inflation as it is commonly known, then this would solve two other problems plaguing cosmology, namely the flatness problem and the horizon problem, leading to an important publication in 1981 [82]. Seminal work in inflationary theory was also conducted by Alexei Starobinsky [83], Andrei Linde [84], Andreas Albrecht [85], and Paul Steinhardt [85] leading to the 2002 Dirac Prize for Guth, Linde, and Steinhardt [86]; the 2012 Breakthrough Prize in Fundamental Physics for Guth and Linde [87]; and the 2014 Kavli Prize for Starobinsky, Linde, and Guth [88]. Furthermore, the idea of linking quantum fluctuations to the origin of large-scale structures within an inflationary paradigm was pioneered in 1981 by the work of Gennady Chibisov and Viatcheslav Mukhanov [89].

To say the universe is expanding at an accelerating rate is to say that $\ddot{a} > 0$. We can immediately see the implication of this on the flatness problem by noting

$$\Omega_K(a) = -\frac{K}{(aH)^2}, \tag{2.4}$$

and so $|\Omega_K|$ grows whenever $(aH)^{-2}$ is an increasing function, which upon inspection of the Friedmann equation (eq. (1.44)) is the case for a universe dominated by a fluid with $w_i > -1/3$ such as matter or radiation. However, if the universe is undergoing an accelerated expansion such that $\dot{a} > 0, \ddot{a} > 0$, then

$$\frac{\mathrm{d}}{\mathrm{d}t}\left(\frac{1}{(aH)^2}\right) < 0, \tag{2.5}$$

therefore $(aH)^{-2}$ is a decreasing function and so $|\Omega_K|$ decreases with time. So we can tentatively see how the flatness problem may be solved by inflation in that the universe may initially have a large $|\Omega_K|$, however, inflation drives the curvature density down sufficiently close to zero, such that after the inflationary era has ended and radiation-domination begins, $|\Omega_K|$ begins to grow again, giving a present-day $|\Omega_{K,0}|$ that is within limits allowed by observational data. The question then remains, for how long does the universe need to undergo inflationary accelerated expansion in order to get, say, $|\Omega_{K,0}| < 0.1$ today? Since the scale factor will be increasing by many orders of magnitude during the inflationary epoch, it is fitting to quantify the increase in terms of the number of e-folds the scale factor undergoes, which is

$$N = \ln\left(\frac{a_f}{a_i}\right), \tag{2.6}$$

where N is the number of e-folds, a_i is the initial value of the scale factor at the start of inflation, and a_f is the final value of the scale factor at the end of inflation. With the assumption that the Hubble parameter $H(a)$ is constant during this period [90, 91], we may then write

$$\begin{aligned} \left|\Omega_K\left(a_f\right)\right| &= \left(\frac{a_f}{a_i}\right)^{-2} \left|\Omega_K\left(a_i\right)\right| \\ &= e^{-2N} \left|\Omega_K\left(a_i\right)\right|, \end{aligned} \tag{2.7}$$

and so requiring $|\Omega_{K,0}| < 0.1$ means that at the end of inflation $a_f \sim 10^{-29}$ [82] we must have $|\Omega_K(a_f)| \lesssim 10^{-59}$ via eq. (2.1), which in turn requires

$$N \gtrsim 68 \tag{2.8}$$

many e-folds to solve the flatness problem, where we have used $|\Omega_K(a_i)| \sim \mathcal{O}(1)$. Note that owing to the logarithmic dependence of N on the curvature density Ω_K, if we impose a much stricter requirement on the current curvature density of say $|\Omega_{K,0}| < 0.001$, then the number of e-folds required increases only to $N \approx 70$

in order to solve the flatness problem.

Now let us look at how inflation can help solve the horizon problem. The horizon problem is concerned with the fact that regions separated by a distance greater than the particle horizon appear to have been in causal contact. Since the particle horizon is a function that increases faster than the physical distance in time for a matter or radiation dominated universe, then two regions that are not in causal contact now could never have been in cosmic history. But what if there was a period in cosmic history where causal regions in the universe universe grew to much larger than the particle horizon? That means then that regions in the sky which are causally disconnected today need not have been so at some point in the past. Note that if the universe is undergoing inflation, then the comoving particle horizon, $(aH)^{-1}$, now becomes a decreasing quantity

$$\frac{d}{dt}\left(\frac{1}{aH}\right) = -\frac{\ddot{a}}{\dot{a}^2} < 0, \tag{2.9}$$

and so it is possible that during inflation, the entire observable universe was brought well within a causal region, thereby solving the horizon problem. Interestingly, the number of e-folds required to solve the horizon problem is similar to that of the flatness problem, typically $N \gtrsim 60$ [92].

2.2 Tensions in ΛCDM

Before we begin exploring tensions in the ΛCDM model, we must first note that although there are only six independent parameters in the baseline concordance model, there exist a number of other cosmological parameters that can be derived from these six. Two of these derived parameters which are of utmost importance to us are the Hubble constant H_0, and σ_8, which is a parameter signifying the root-mean-square mass fluctuation in a sphere of radius $8h^{-1}$Mpc at redshift $z = 0$ defined by $\sigma_8 \equiv \sigma\left(8h^{-1}\text{Mpc}\right)$ where [51]

$$\sigma^2(\mathcal{R}) = \int_0^\infty \frac{dk}{k}\Delta_m^2(k)\left[3\,\frac{j_1(k\mathcal{R})}{k\mathcal{R}}\right]^2, \tag{2.10}$$

where $\mathcal{R}$ is the radius of the sphere, $\Delta^2_m(k)$ is the dimensionless matter power spectrum and $j_1(x)$ is the first spherical Bessel function such that the term in square brackets is the Fourier transform of a sphere of radius $\mathcal{R}$. Furthermore, owing to a degeneracy that arises between the Ω_m and σ_8 parameters in one of the troublesome data sets, it is useful to introduce another derived parameter. This parameter is denoted by S_8, and is based on the σ_8 parameter and the matter energy density parameter Ω_m, being defined by

$$S_8 \equiv \sigma_8 \sqrt{\Omega_m/0.3} \quad . \tag{2.11}$$

As we mentioned earlier, the ΛCDM model is able to explain nearly all data sets, most notably the CMB anisotropy data as measured by *Planck* [50] and background data sets such as from Baryon Acoustic Oscillations (BAO) [93] and supernovae Type Ia (SNIa) [94] measurements, both accurately and consistently, with no apparent tensions in the parameters. There is, however, mounting evidence that there are serious tensions in the ΛCDM model for certain data sets. The two major data sets which are in conflict with the ΛCDM model as determined by *Planck* are the local measurements of the Hubble constant H_0 [71] and the determinations of σ_8 from weak lensing experiments [72, 73, 74].

Perhaps the most famous tension in cosmology at present is the tension between H_0 as inferred by earlier-universe *Planck* CMB measurements [50] and H_0 as inferred by more direct later-universe local measurements, known as the H_0 *tension*. The value of H_0 inferred from assuming a ΛCDM model and using the full Planck temperature, polarisation, cross-correlation, and lensing data set is $H_0 = 67.37 \pm 0.54\,\mathrm{km\,s^{-1}\,Mpc^{-1}}$ at 1σ [50], whereas local distance ladder measurements determine a value of $H_0 = 74.03 \pm 1.42\,\mathrm{km\,s^{-1}\,Mpc^{-1}}$ at 1σ [95], giving a discrepancy of $6.6 \pm 1.5\,\mathrm{km\,s^{-1}\,Mpc^{-1}}$ at 1σ. It is useful to be able to quantify the degree of tension between two determinations of given parameter and one may do so by the following equation

$$T \equiv \frac{\left|\mu_A - \mu_B\right|}{\sqrt{\sigma_A^2 + \sigma_B^2}} \quad , \tag{2.12}$$

where T is the tension in the parameters, μ_A and μ_B are the mean values of the parameter from data sets A and B, and σ_A and σ_B are the 1σ confidence limits or errors, as determined from data sets A and B. Using this equation to explore the tension between H_0 as derived from *Planck* compared to H_0 as inferred from local measurements, we find that there exists a $\sim 4.4\sigma$ tension in H_0 between the measurements when assuming the ΛCDM model. Furthermore, investigations [96] suggest that this discrepancy cannot solely be due to errors in measurement or systematic sources, therefore strongly suggesting that we need to look beyond the ΛCDM model in order to resolve this significant tension. It is important to note here that the larger value of H_0 as determined from local measurements is a model-independent measurement of H_0, whereas the value of H_0 as determined by *Planck* is a model-dependent value. Therefore, any extension to the ΛCDM model that hopes to resolve this tension must obtain a value of H_0 from *Planck* that is significantly larger than the value obtained assuming ΛCDM, such that it is not in tension with the local measurements of H_0.

Some of the most immediate extensions to ΛCDM which appear to help alleviate this tension at least in part include allowing the effective number of neutrino species $N_{\rm eff}$ to vary, thereby accounting for undetected relativistic species, and phantom dark energy, which allows for a fluid with an equation of state $w < -1$, however, there are no shortage of extensions to ΛCDM which appear to help resolve this tension [97]. The principle of Occam's Razor [98], the physical viability and motivation of a model, and statistical model selection analysis will prove which of these many models, if any, provides the solution to this tension in H_0. Great interest should be paid to model if it is able to simultaneously resolve several tensions and problems, such as what inflationary theory did for the flatness problem, the horizon problem, the magnetic monopole problem, and the primordial origin of large-scale structure in the universe.

The second major data set that presents tensions in the ΛCDM model is from the more direct cosmic shear determinations of σ_8 such as that reported by the KiDS-1000 and DES Y3 cosmic shear surveys [72, 73, 74]. Unlike the H_0 tension which is a tension between an inferred model-dependent value and a

directly measured model-independent value, this tension is between two data sets which give a significantly different inferred value of S_8 under the assumption of ΛCDM. Assuming ΛCDM, the inferred value of S_8 using *Planck* measurements is $S_8 = 0.830 \pm 0.013$ at 1σ [50], whereas the inferred value of S_8 using the KiDs-1000 cosmic shear measurements is $S_8 = 0.759^{+0.024}_{-0.021}$ at a 1σ confidence limit under ΛCDM [72, 73], therefore presenting a $\sim 2.7\sigma$ tension in the S_8 parameter assuming the ΛCDM model.

It is important to note too, that the level of tension in this parameter is significantly less than that of H_0, therefore the probability of it being due to statistical fluctuations and systematic issues is higher than with H_0, however, it is still quite possible that this tension is indicative of new physics beyond the standard model of cosmology and therefore solutions in this line of thinking merit attention. It is worthy to note also that a model which extends ΛCDM and infers a result of a parameter, H_0 say, with the same mean value as inferred by ΛCDM but with larger 1σ errors would in fact reduce the tension T but only because of an increase in uncertainty. Furthermore, models which reduce tension in one parameter, say H_0, may increase tension in another parameter, say S_8, but not only that, extensions to ΛCDM increase the degrees of freedom in that model which in turn negatively compensate the model in statistical model selection. Careful attention, therefore, must be paid to extensions of ΛCDM and claims of resolving tensions.

Recall that inflationary theory predicts that our universe should be consistent with a flat universe $\Omega_{K,0} = 0$ to a high degree of accuracy, and indeed, upon the combination of *Planck*, BAO, and SNIa data, we find that $\Omega_{K,0} = 0.001 \pm 0.002$ [50]. It is important to note here that inflationary theory does not predict that our universe should be in fact flat, but that we can expect $\Omega_{K,0}$ to be sufficiently close to zero, such that our universe is consistent with a flat universe under observational and experimental bounds. We also mentioned that the ΛCDM model as determined by *Planck* is consistent with nearly all other data sets, such as from BAO and SNIa measurements, and this too is true.

Strikingly, however, when curvature is allowed to vary, recent *Planck* data [50]

suggests that our universe is in fact closed $\Omega_{K,0} = -0.044^{+0.018}_{-0.015}$ such that $\Omega_{K,0} < 0$ at a $\sim 3.4\sigma$ or more than 99% confidence limit, in contrast to when *Planck* is combined with BAO or SNIa data. A signal of a closed universe does not serve as a death-blow to inflationary theory as a whole, as there exists inflationary models that could produce $\Omega_{K,0} \sim -0.1$ [99], however, these models do require additional fine-tuning in order to achieve such a signal and are therefore unappealing. Recent research [100] has suggested however, that this apparent detection of a closed universe could instead be a consequence of the choice of likelihood code for the *Planck* data and choice of prior on $\Omega_{K,0}$, further noting that *Planck* lensing, BAO, and SNIa data help break geometric degeneracies that exist in the parameters and as a result all of these additional data sets indicate a preference for a flat universe. Clearly, the fact that *Planck* prefers a closed universe cannot easily be dismissed as insignificant and its relationship to other tensions and problems present in ΛCDM cosmology beckons to be explored further.

2.3 The dark sector

We mentioned early that in the concordance model, there exists matter Ω_m, radiation Ω_r, and a cosmological constant Ω_Λ which together make up the total energy budget of the universe. We further remarked that the matter sector Ω_m can be decomposed into two parts, the baryonic sector Ω_b and the cold dark matter sector Ω_{cdm} which is thought to make up $\sim 85\%$ of the total matter energy budget in our universe. In cosmology, baryonic matter refers to ordinary matter composed of atoms, protons, and neutrons; whereas the cold dark matter refers to a hitherto unknown, non-relativistic, non-baryonic matter which interacts via gravity alone. The existence of baryonic objects, such as massive astrophysical compact halo objects (MACHOs) like black holes and neutron stars, being responsible for all of the effects of dark matter has been heavily constrained [101] such that the most popular candidates for cold dark matter are non-baryonic [102]. To be sure, cold dark matter in this context does not refer to non-luminous baryonic matter, but instead refers to non-baryonic matter that requires extensions to the Standard

Model of particle physics to be made.

The existence of dark matter has its origins from as early as 1884 by Lord Kelvin [103], when upon observing the velocity dispersion of stars about the centres of galaxies, he found that there was not enough mass as inferred from luminosity measurements to explain the velocities, so that therefore there must be many non-luminous bodies in our galaxies, concluding that *"Many of our supposed thousand million stars, perhaps a great majority of them, may be dark bodies"*. This discrepancy between the observed mass from luminosity measurements and the mass required in order to explain velocity dispersions and galactic rotation curves was further reported by Jacobus Kapteyn in 1922 [104], Knut Lundmark in 1930 [105], Jan Oort in 1932 [106], and notably Fritz Zwicky in 1933 [107], indicating that there must exist a large amount of invisible, non-luminous mass in the universe. Later studies confirmed these results with two important publications in 1974 by Jaan Einasto and collaborators [108] and Jeremiah Ostriker and collaborators [109] such that by 1980 there was agreement that dark matter must make up a large part of the matter content our universe [110]. Since the 1980s, new techniques and observations have reinforced the existence of dark matter such as measurements from gravitational lensing by galaxy clusters [111], $N-$body structure formation simulations [112], and the matter power spectrum and Cosmic Microwave Background temperature anisotropies power spectrum [113].

Whilst cold dark matter is a fundamental ingredient in concordance cosmology, the nature of dark matter has yet to be identified. Many extensions to the Standard Model of particle physics predict dark matter-like particles [114] such as sterile neutrinos [115], axions [116], and weakly interacting massive particles (WIMPs) [117], and at present, the search for a dark matter-like particle is one of the leading challenges in particle physics [118], being currently sought after in experiments such as the LUX-ZEPLIN experiment [119], the XENON project [120], and the PandaX-II experiment [121].

We now turn our attention to the second ingredient of the dark sector, the cosmological constant Λ. We begin by recalling that the cosmological constant Λ

was first introduced by Einstein in order to obtain a static, closed, matter-filled universe. However, after undeniable evidence for the expansion of the universe began mounting, Λ fell into disfavour within the scientific community, being regarded by some as nothing more than an unnecessary parameter and relic of outdated static-universe theories. In fact, after Einstein's conversion to belief in an expanding universe, Einstein once famously remarked to his friend George Gamow that introducing the cosmological constant was *"the biggest blunder"* of his life [122].

Not all were so quick to abandon Λ all together, however; indeed an expanding universe does not at all rule out the existence of a cosmological constant, but the existence of Λ, whilst being allowed mathematically, was not physically motivated and so many thought it best to be avoided. Some notable proponents of Λ who did not drop their support even after accepting the expansion of the universe include Eddington [29] and Lemaître [123]. Indeed, cosmological models which excluded the cosmological constant Λ all suffered from the same problem, the age problem, which has been noted since at least the early 1930s [29, 123]. The age problem arises in cosmological models without Λ from the fact that they all have an upper bound on the age of the universe which is less than the apparent age of objects found in the universe. We can see this by considering the age of the universe t_0 for the general case

$$t_0 = H_0^{-1} \int_0^1 \frac{da}{a\sqrt{\Omega_{r,0}a^{-4} + \Omega_{m,0}a^{-3} + \Omega_{K,0}a^{-2} + \Omega_{\Lambda,0}}}, \tag{2.13}$$

and so for a radiation-only universe we have $t_0 = (1/3)H_0^{-1}$, for a matter-only universe we have $t_0 = (2/3)H_0^{-1}$, and for a curvature-only universe we have $t_0 = H_0^{-1}$. For a Λ-only universe we note that the age of the universe is infinite, therefore the age of the universe for a cosmological model can be arbitrarily increased by increasing the present-day energy budget of the cosmological constant, $\Omega_{\Lambda,0}$, in that model.

The prevailing cosmological model since the scientific community reached a consensus on the expansion of the universe was the Einstein-de Sitter model

[124, 31], which describes a flat, matter-only universe. In this model, the age of the universe is $t_0 = (2/3)H_0^{-1}$, which using Edwin Hubble's estimate [28] of $H_0 \approx 500\,\mathrm{km\,s^{-1}\,Mpc^{-1}}$ gives an age of the universe of $t_0 \approx 1.3$ billion years which was less than the calculated age of the Earth at the time of at least 2 billion years [125]. We note, however, that the calculated age of the Earth had a large uncertainty to it and so this problem was not seen as too much of a threat to the Einstein-de Sitter model by some. For others, this disagreement between the age of the universe and the age of the Earth was taken more seriously, and it is thought that this was at least in part one of the motivating factors in the development of the steady-state model [124] mentioned in chapter 1. It was noted by Eddington [29] and Lemaître [123] that if the cosmological constant is included in the model, then the age of the universe can be increased to fit observations since

$$\begin{aligned} t_0 &= H_0^{-1} \int_0^1 \frac{da}{a\sqrt{\Omega_{m,0}a^{-3} + \Omega_{\Lambda,0}}} \\ &= \frac{2H_0^{-1}}{3\sqrt{\Omega_{\Lambda,0}}} \sinh^{-1}\left(\sqrt{\frac{\Omega_{\Lambda,0}}{1-\Omega_{\Lambda,0}}}\right), \end{aligned} \tag{2.14}$$

where we have used the constraint equation (eq. (1.42)) $\Omega_{m,0} + \Omega_{\Lambda,0} = 1$, and so in the limit $\Omega_{\Lambda,0} \to 0$ we recover the Einstein-de Sitter age of $t_0 \to (2/3)H_0^{-1}$ whereas in the limit $\Omega_{\Lambda,0} \to 1$ we see that the age is non-finite $H_0 t_0 \to \infty$, therefore any age within $2/3 < H_0 t_0 < \infty$ is allowed with the inclusion of the cosmological constant term in a flat, matter-filled universe, thereby solving the age problem in isolation. Over time, however, refinements in the determinations of the Hubble constant brought it down to lower values [126], such that the age of the universe in the Einstein-de Sitter case increased to acceptable values, thereby reducing any tensions with measurements of old objects in the universe such as the Earth.

During the late 1980s and early 1990s, however, determinations of the age of globular clusters began pushing the minimum age of the universe to ever increasing values [127] which were in tension with the competing values of H_0 at the time coming from independent measurements [128] during a period known as the

"Hubble wars" [129]. This was posing a serious problem for the Einstein-de Sitter model at the time, since independent measurements of H_0 were giving an age of universe $t_0 = (2/3)H_0^{-1}$ which was lower than the age of globular clusters. This rose to be a major outstanding problem in modern cosmology until the pioneering supernovae measurements of the late 1990s [47, 48] strongly supported the inclusion of the cosmological constant into the cosmological standard model thereby solving the age problem, where we note that the value of $\Omega_{\Lambda,0}$ as determined by the most recent *Planck* [50] release gives an age of universe $t_0 \approx 0.95H_0^{-1} \approx 13.8$ billion years in agreement with recent globular cluster measurements [127].

So we see that the introduction of the cosmological constant solved two important problems in cosmology, the age problem and the problem of the late-time accelerated expansion of the universe as inferred by supernovae measurements [47, 48]. However, the cosmological constant brought along with it two new problems that are considered major outstanding problems in cosmology today, these are the coincidence problem and the cosmological constant problem.

We appear to be living at a very special point in time. Bringing the Friedmann equation (eq. (1.44)) to mind for a flat universe and noting the dependence on the scale factor for each energy species, we see that in early times we have an era of radiation-domination, followed by matter-domination, followed finally by Λ-domination. Further, unless one happens to be sat at a unique point in the transitory period from one era of domination to another, the ratios of various energy species to one another will be many orders of magnitude, for example, the ratio of the cosmological constant energy density to matter density scales like $\Omega_\Lambda/\Omega_m \propto a^3$ and so we can expect the ratio to vary drastically depending on the time chosen in cosmic history.

Strikingly, we find that the value of the cosmological constant energy density today is approximately the same as matter energy density [50], that is, that $\Omega_\Lambda/\Omega_m \sim \mathcal{O}(1)$, putting us at a very unlikely point in time. One can see that through the cubic dependence on the scale factor, $\Omega_\Lambda/\Omega_m \propto a^3$, a point in time that is not much earlier or later than now will give a ratio that is magnitudes smaller or larger, therefore presenting a serious problem of fine-tuning. An im-

mediate consequence of this coincidence of energy densities is that the era of accelerated expansion must have happened recently at $z < \mathcal{O}(1)$. The fact that we exist at the time when the energy densities of the cosmological constant and matter sector roughly coincide seems extremely unlikely, hence raising a problem for modern cosmology known as the coincidence problem.

Recall that Einstein introduced Λ into his field equations simply to find a static, closed, matter-filled universe which he later abandoned. Whilst the introduction of Λ was not a mathematically erroneous move, its existence was not physically motivated and it was uncertain what it exactly represented. Some, like Einstein, thought that if cosmology could survive without invoking Λ then all the better for it, whereas others like Eddington, Lemaître, and Richard Tolman [130] thought that one could not be so quick to dismiss the cosmological constant and that it might even represent a new fundamental constant of nature [131].

As we saw in chapter 1, the cosmological constant term can be expressed on the right hand side of the Einstein field equations where its form is the same as that of vacuum energy. In General Relativity, gravity couples to all energy and momentum, and so even the vacuum energy should have a gravitational effect. It is fitting to mention that the problematic role of vacuum energy in cosmology has been in discussion since at least 1926 when Wilhem Lenz [132] calculated that if the vacuum energy of empty space did indeed contribute gravitationally then *"the radius of the observable universe would not reach even to the Moon"*. The gravitational effects of the vacuum were largely disregarded by cosmologists subsequently owing to the fact that the contribution must either be zero or extremely small, far smaller than any theoretical predictions, in order to be consistent with cosmological observations of the time. Yakub Zel'dovich revisited this problem in 1967 [133] armed with the new language of Quantum Field Theory and considered a non-vanishing vacuum energy arising from quantum effects, further exploring the possibility of this non-vanishing vacuum energy contributing to the cosmological constant. Much like Lenz in 1926, however, he found that theoretical predictions of the vacuum energy density far exceeded the upper bounds for the cosmological constant by many orders of magnitude.

This enormous mismatch between theoretical vacuum energy density predictions and the observed cosmological constant energy density is what is known as the cosmological constant problem, and has been described as *"the worst theoretical prediction in the history of physics"* [134], with discrepancies typically being between $\sim 50 - 120$ orders of magnitude [135, 136] or solutions requiring fine-tuning to at least $\sim 50 - 120$ decimal places depending on how the problem is formulated [137]. With the resurgence of Λ in the late 1990s, this problem has been brought to the forefront of physics and remains one of the most important problems in fundamental physics today.

Quantum Field Theory and General Relativity are two pillars of modern physics and both have been rigorously tested to extremely high accuracy, with little evidence that either need to be fundamentally modified in order to explain our observations of nature and the universe thus far [138, 139]. This level of disagreement between the two then poses a serious problem for modern physics, and there are no agreed upon possible solutions that are able to solve this problem whilst also not creating conflicts with other experiments and observations of nature and our universe [140, 141, 142, 143, 144, 145].

In an effort to resolve this issue, some have sought anthropic reasoning [146] which attempts to explain various fine-tuning problems in our universe. The weak anthropic principle [147] commonly invokes the existence of a multiverse containing a possibly infinite number of universes with different properties and then reasons that we observe our particular universe to have certain properties, such as a small cosmological constant, because if our universe did not have those properties, such as if our universe had a large cosmological constant, then intelligent life would not exist and so there would be no observers to observe the universe and ask the question in the first place. Some have criticised this way of reasoning as being unscientific or as simply being a mere tautology that a universe with observers in it, such as humans, *"must be found to possess those properties necessary for the existence of observers"* [148], however, this has not stopped scientists from using this line of reasoning to calculate bounds on certain physical parameters. Steven Weinberg in 1987 [149] notably calculated an

anthropic bound on Λ arguing that if Λ were too large and negative then the universe would collapse before intelligent life could form, whereas if Λ were too large and positive then structures such as stars and galaxies could not form, therefore intelligent life could not exist.

The cosmological constant appears to be the simplest explanation for the recent epoch of accelerated expansion, however, these problems plaguing Λ have led cosmologists to search for other possible possible sources of late-time accelerated expansion, and henceforth a plurality of models have ensued [150]. Because of the many possibilities, cosmologists term any model that seeks to explain the late-time accelerated expansion as *dark energy*, which together with *dark matter*, make up the *dark sector*. The reason why these labels gained the "dark" term is because their existence is inferred via their gravitational effects alone, with the precise microphysical description of dark matter or dark energy unknown as of yet. Whatever dark energy is, we know that it in order for it to agree with cosmological observations, it must mimic the cosmological constant at late-times, aside from this, however, a whole host of possibilities exist [150].

In the search for alternatives to the cosmological constant which, whilst remaining consistent with observations, had a firmer physical grounding and were less plagued by problems, the idea of dark energy being sourced by a dynamical scalar field began to take hold in a model called *quintessence*. In 1988, two seminal papers were released by Bharat Ratra & Jim Peebles [151] and Christof Wetterich [152] where they investigated the cosmological consequences of a slow-rolling scalar field and found that it can mimic the cosmological constant. Then in 1998, when mounting evidence for an accelerated expansion was building up, Robert Caldwell, Rahul Dave, and Paul Steinhardt released a foundational paper [153] where the term *"quintessence"* was coined and described how this quintessence scalar field could replace the time-independent cosmological constant Λ whilst still agreeing with cosmological observations. In particular, if dark energy is due to a quintessence scalar field then this may help to ameliorate the cosmological constant problem [154]. At present, one of the most popular candidates for dark energy is a classical scalar field with a canonical kinetic term and self-interaction

potential, known as quintessence.

If such a scalar field exists, however, then it is expected to couple to all matter fields unless forbidden by some symmetry [155], thereby producing a "fifth force" [156]. Couplings to baryonic matter have been heavily constrained by fifth-force experiments [157, 158, 159], however, couplings to dark matter are not able to be probed by conventional fifth-force experiments and the possibility for a potentially strong coupling between dark energy and dark matter remains [160]. Interestingly, if the quintessence scalar field is allowed to interact with dark matter then this may help to solve the coincidence problem too [161]. Quintessence models usually assume that the scalar field interacts with matter fields via gravity alone, however, there is no reason to assume this is true until nature proves otherwise. Models which allow for an interaction between the quintessence scalar field and matter fields are known as coupled quintessence models [162], or more generally, models allowing for an interaction between dark energy and matter fields are known as interacting dark energy models [163], and it is such models that we will be exploring in depth for the rest of this thesis.

2.4 Conclusions

In this chapter, we explored some of the problems associated with the standard Big Bang model, namely the flatness and horizon problems, and discussed how they may be solved if the universe undergoes a period of accelerated expansion in its very early history, known as the inflationary epoch. We then looked at some of the tensions present in ΛCDM, with the possibility that they hint at having to look beyond the ΛCDM model, and the possible resolutions of the tensions therein. Finally, we explored the enigmatic dark sector and some of the serious problems surrounding the cosmological constant.

The ΛCDM model is our best cosmological model to date, and yet it is in enormous disagreement with predictions of fundamental physics with regards to the vacuum energy density. These considerations and others have propelled cosmologists to look for alternative theories for dark energy. One such model is

a slow-rolling quintessence scalar field able to mimic the cosmological constant at late-times and therefore is consistent with cosmological data at present. If such a scalar field exists then it should couple to and interact with matter fields in what is known as interacting dark energy. A potentially strong interaction between dark energy and dark matter is permitted by current data, therefore it is imperative we explore the possibility of interactions in the dark sector in order to gain further insight into this obscure sector of nature thought to comprise $\sim 95\%$ of the energy budget of universe [50], of which we know little about.

3 — Cosmological evolution and imprints of interacting dark energy

The quintessence scalar field models are some of the most promising candidates for dark energy to date, having a clear physical motivation and having been shown to help alleviate some of the deeply troubling problems affecting the cosmological constant, namely the cosmological constant problem [154] and the coincidence problem [164]. Despite its theoretical flaws, the cosmological constant, which possesses a static, non-dynamical, and constant energy density, is still the simplest model for dark energy, introducing a minimal number of extra degrees of freedom and also strongly agreeing with almost all current cosmological observations [50]. However, cosmological observations are also consistent with a large class of other models, such as quintessence models [165], and so in the absence of the cosmological constant being responsible for dark energy, the next simplest model not plagued by theoretical problems appears to be the dynamical, time-dependent, and canonical quintessence scalar field.

The existence of a light scalar field is a prediction of many fundamental theories of nature such as string theory [166], supersymmetry [167], pseudo-Nambu-Goldstone models [168], and scalar-tensor theories of gravitation [169], and a great deal of effort has been made to try and embed the quintessence scalar field into a more foundational theoretical framework [165]. Moreover, many of these theories predict an explicit long-range coupling between the light scalar field and

the various components of the universe such as baryons, radiation, and dark matter, in a species-dependent manner [170, 167]. It is therefore natural to search for such interactions in our exploration for the origin of dark energy.

It is interesting to note that scalar fields actually have a long history in cosmology, dating back to at least the early 1940s, long before cosmological observations started demanding the existence of a cosmological constant-like term to dominate the energy budget at late-times. One area of cosmology where scalar fields play a foundational role are in so-called *scalar-tensor* theories of gravity [171], which are alternative theories to General Relativity whereby gravity is mediated by both a non-minimally coupled scalar field and a metric tensor field.

These scalar-tensor theories of gravity were founded during the 1940s to 1960s and had a diverse range of motivations, and often quite different interpretations too, with one of the earliest notions of scalar-tensor theory being ascribed to Willy Scherrer in 1941 as motivated by scalar relativistic wave mechanics [172]. Then in 1945, Pascual Jordan [173] presented a scalar-tensor theory which replaced the gravitational constant with a time-varying scalar field, as inspired by Paul Dirac's Large Numbers Hypothesis [174, 175], set in the framework of the five-dimensional Kaluza-Klein unified field theory [176] but in the projective relativity [177] approach. Around the same time, Yves Thiry and collaborators [178, 179, 180] were working on Kaluza-Klein theory but from a more mathematical perspective in a unitary field theory approach and arrived at similar results to Jordan. During the 1950s, Jordan and collaborators began distancing themselves from unified field theory interpretations and motivations, and started to interpret their scalar-tensor theories as extended theories of gravitation.

Then in 1961, inspired by Dirac's Large Numbers Hypothesis, Mach's principle, and the equivalence principle, Carl Brans and Robert Dicke proposed a scalar-tensor theory, named Brans-Dicke theory [181], which they also presented as an extended theory of gravity. Interestingly, the Lagrangian they proposed is the same as proposed by Scherrer in 1941 [172] and the field equations they derived were derived in 1948 by Günther Ludwig and Claus Müller [182, 183]. Brans and Dicke noted that although *"there is a formal connection between this*

theory and that of Jordan...there are differences and the physical interpretation is quite different" [181], with one important difference being that the scalar field and the Lagrangian for matter are not directly coupled in the Brans-Dicke action. This means that, unlike in Jordan's theory, the weak equivalence principle is preserved since all matter species are coupled to the same metric. Note that although in the action for Brans-Dicke theory the scalar field is not coupled to the matter Lagrangian, thus satisfying the weak equivalence principle, there does exist a coupling between the scalar field and matter in the field equations.

The scalar-tensor theory proposed by Brans and Dicke presented itself as a modest extension of General Relativity and didn't invoke grand ideas of unified field theories and hidden extra dimensions, thus, combined with the prestige of the authors, Brans-Dicke theory made a huge impact in the scientific community when it made its first appearance and established itself as the paradigmatic scalar-tensor theory of gravity.

The standard quintessence models of dark energy propose a minimally-coupled scalar field with a canonical kinetic term that is slow-rolling and dynamical such that it can provide the late-time accelerated expansion of the universe and also help to resolve some of the issues surrounding Λ. In a standard Brans-Dicke model of quintessence, however, the scalar field has a non-canonical kinetic term and is non-minimally coupled to gravity whilst being minimally coupled to the matter Lagrangian. The theory presented in this way is said to be in the Jordan frame, which is when there is an explicit non-minimal coupling between the scalar field and gravity. However, we are able to recover the case where the quintessence scalar field is minimally coupled to gravity, known as the Einstein frame, if we perform a conformal transformation [184] of the metric. If we conformally transform the metric, then we can recover a canonical kinetic term for the scalar field too, however, this metric transformation introduces a direct, non-minimal coupling between the scalar field and matter.

In the Einstein frame, this can be seen as the mass of matter particles and the coupling constants now becoming dependent on the scalar field, whereas in the Jordan frame, this was encapsulated with the gravitational constant being

replaced by a dynamical quantity. There are debates about which frame can or should be considered the "physical" frame [185], however, unless stated otherwise, we will be working in the Einstein frame where the scalar field has a canonical kinetic term and is minimally coupled to gravity.

In this context, the standard uncoupled quintessence models can be seen as conformally transformed Brans-Dicke scalar-tensor theories in the Einstein frame, however, in contrast to the Brans-Dicke model, they are only minimally coupled to matter. There is no reason to forbid an interaction between the scalar field and other fields in the universe at a fundamental level, unless of course, there exists some symmetry in nature which we have not discovered yet which forbids such interactions [155]. Although couplings to baryons have been heavily constrained by fifth-force experiments [186], couplings to dark matter have not been so heavily suppressed [187] and given the exotic nature of dark matter and dark energy, should be thoroughly explored. Although there exists a number of ways of introducing an interaction between dark energy and dark matter [187], with some being at a fundamental level and others at a more phenomenological level, we introduce an interaction by allowing the metric describing the dark matter sector to become dependent on the DE scalar field, as seen in Brans-Dicke type theories following a conformal transformation.

In section 3.1 we introduce the action of the interacting dark energy model, whereby cold dark matter is conformally coupled to the quintessence scalar field, and look at its background dynamics. Then in section 3.2, we look at the evolution of perturbations in this theory and discuss their behaviour in the small-scale Newtonian limit in section 3.3. We then look at some of the imprints this IDE model has on the background and perturbation level in section 3.4, finally concluding in section 3.5.

3.1 Model and background evolution

The interaction between the dark energy (DE) scalar field and dark matter (DM) field is introduced in a scalar-tensor theory setup whereby the DM particles travel

along geodesics defined by a DE-dependent metric $\widetilde{g}_{\mu\nu}$. The total action for the IDE theory in the Einstein frame is

$$\begin{aligned}\mathcal{S}_{\rm tot} = &\int d^4x\sqrt{-g}\left[\frac{M_{\rm Pl}^2}{2}R - \frac{1}{2}g^{\mu\nu}\partial_\mu\phi\,\partial_\nu\phi - V(\phi) + \mathcal{L}_{SM}(g_{\mu\nu},\sigma_i)\right] \\ &+ \int d^4x\sqrt{-\widetilde{g}}\,\widetilde{\mathcal{L}}_{DM}(\widetilde{g}_{\mu\nu},\psi_i),\end{aligned} \tag{3.1}$$

where $g_{\mu\nu}$ is the minimally coupled metric with determinant g, $M_{\rm Pl} = \kappa^{-1} = (8\pi G)^{-1/2}$ is the reduced Planck mass such that $M_{\rm Pl} = 2.4 \times 10^{18}$ GeV, G is the Newtonian gravitational constant, and R is the Ricci scalar. The DE scalar field ϕ has a canonical kinetic term and potential $V(\phi)$. The Standard Model (SM) sector is described by the Lagrangian $\mathcal{L}_{SM}$ whereby SM particles travel along geodesics defined by the minimally-coupled metric $g_{\mu\nu}$ where σ_i are the SM fields. The SM Lagrangian can be further decomposed into a relativistic (r) and baryonic sector (b) such that $\mathcal{L}_{SM} = \mathcal{L}_r + \mathcal{L}_b$. Finally, the DM sector is described by the Lagrangian $\widetilde{\mathcal{L}}_{DM}$ whereby DM particles travel along geodesics defined by the modified DE-dependent metric $\widetilde{g}_{\mu\nu}$ where ψ_i are the DM fields. We will assume that there is only one DM field for the rest of this chapter. We see that in this scalar-tensor theory setup, the action in the Einstein frame describes only the DM particles as having a direct interaction with the DE scalar field. The DM particles experience a modified gravitational field $\widetilde{g}_{\mu\nu}$ which depends directly on the DE field ϕ and therefore experience an additional 'fifth-force' as mediated by ϕ. We investigate couplings of the form

$$\widetilde{g}_{\mu\nu} = C(\phi)g_{\mu\nu}, \tag{3.2}$$

where $C(\phi)$ is the conformal coupling function, but remark that, in general, a disformal term is allowed too [188].

Now that we have defined the action of our theory, we may vary it with respect to the metric $g_{\mu\nu}$ to derive the equations of motion. Doing so, we recover the

Einstein field equations

$$R_{\mu\nu} - \frac{1}{2}g_{\mu\nu}R = \kappa^2 \left(T^{\phi}_{\mu\nu} + T^{SM}_{\mu\nu} + T^{DM}_{\mu\nu}\right), \tag{3.3}$$

where the energy-momentum tensors are defined by

$$T^{\phi}_{\mu\nu} := \partial_\mu\phi\partial_\nu\phi - g_{\mu\nu}\left(\frac{1}{2}g^{\rho\sigma}\partial_\rho\phi\partial_\sigma\phi + V(\phi)\right), \tag{3.4}$$

$$T^{SM}_{\mu\nu} := -\frac{2}{\sqrt{-g}}\frac{\delta\left(\sqrt{-g}\mathcal{L}_{SM}\right)}{\delta g^{\mu\nu}}, \qquad T^{DM}_{\mu\nu} := -\frac{2}{\sqrt{-g}}\frac{\delta\left(\sqrt{-\widetilde{g}}\widetilde{\mathcal{L}}_{DM}\right)}{\delta g^{\mu\nu}}, \tag{3.5}$$

for the DE, SM, and DM fields respectively. The SM particles follow the ordinary conservation equation

$$\nabla^\mu T^{SM}_{\mu\nu} = 0, \tag{3.6}$$

however, owing to the interaction between the DE and DM fields, their conservation equations are now altered thus reflecting an exchange of energy between the species. The conservation equations for the DE and DM fluids respectively are

$$\nabla^\mu T^{\phi}_{\mu\nu} = -Q\nabla_\nu\phi, \tag{3.7}$$

$$\nabla^\mu T^{DM}_{\mu\nu} = Q\nabla_\nu\phi, \tag{3.8}$$

where the coupling Q is defined by [189]

$$Q = \frac{1}{2}\frac{\mathrm{d}\ln C}{\mathrm{d}\phi}T_{DM}, \tag{3.9}$$

and where T_{DM} is the trace of the DM energy-momentum tensor. Note that the total energy-momentum tensor $T^{\mathrm{tot}}_{\mu\nu} = T^{\phi}_{\mu\nu} + T^{SM}_{\mu\nu} + T^{DM}_{\mu\nu}$ is conserved, $\nabla^\mu T^{\mathrm{tot}}_{\mu\nu} = 0$, hence is consistent with the twice-contracted Bianchi identity (eq. (1.17))

$\nabla^\mu G_{\mu\nu} = 0$, thus this coupling preserves general covariance.

Now let us specify the metric $g_{\mu\nu}$ to be the flat FLRW metric such that the line element in Cartesian coordinates is given by

$$\mathrm{d}s^2 = g_{\mu\nu}\mathrm{d}x^\mu \mathrm{d}x^\nu = -a^2(\tau)(-\mathrm{d}\tau^2 + \delta_{ij}\mathrm{d}x^i\mathrm{d}x^j) \tag{3.10}$$

where $a(\tau)$ is the scale factor in conformal time τ and δ_{ij} is the Kronecker delta. Furthermore, let us describe each energy species i by the perfect fluid energy-momentum tensor (eq. (1.28))

$$T^{(i)}_{\mu\nu} = (\rho_i + P_i)U_\mu U_\nu + P_i g_{\mu\nu}, \tag{3.11}$$

where ρ_i and P_i are the fluid's energy density and pressure in the Einstein frame respectively, and where U_μ is the four-velocity of the fluid. The conservation equation for the scalar field (eq. (3.7)) implies

$$\Box\phi - V_{,\phi} = -Q, \tag{3.12}$$

which, using the flat FLRW metric (eq. (3.10)), gives the modified Klein-Gordon equation

$$\phi'' + 2\mathcal{H}\phi' + a^2 V_{,\phi} = a^2 Q, \tag{3.13}$$

where a prime signifies a derivative with respect to conformal time and where $\mathcal{H} := a'/a$ is the conformal Hubble parameter. Furthermore, the conservation equations for the SM and DM fluids (eqs. (3.6) and (3.8)) yield

$$\begin{aligned} \rho_r' + 4\mathcal{H}\rho_r &= 0, \\ \rho_b' + 3\mathcal{H}\rho_b &= 0, \\ \rho_c' + 3\mathcal{H}\rho_c &= -Q\phi', \end{aligned} \tag{3.14}$$

and the Friedmann equations are given by

$$\mathcal{H}^2 = \frac{\kappa^2}{3} a^2 \left(\rho_r + \rho_b + \rho_c + \rho_\phi\right), \tag{3.15}$$

$$\mathcal{H}' = -\frac{\kappa^2}{6} a^2 \left(2\rho_r + \rho_b + \rho_c + \rho_\phi + 3P_\phi\right) \ , \tag{3.16}$$

where the relativistic, baryonic, DM, and DE sectors are represented by the subscripts r, b, c and ϕ respectively. If we relax the requirement of $w_c = 0$, then the coupling Q given by eq. (3.9) is

$$Q = -\frac{1}{2}\frac{\mathrm{d}\ln C}{\mathrm{d}\phi}(1 - 3w_c)\rho_c. \tag{3.17}$$

3.2 Perturbations

Let us now look at the evolution of scalar perturbations in our coupled quintessence model where we allow the coupled DM fluid to have a general equation of state w_c. We will start by looking at the evolution of perturbations in the synchronous gauge and then follow on by obtaining the perturbation equations in the conformal Newtonian gauge.

3.2.1 Synchronous gauge

We follow the convention of Chung-Pei Ma and Edmund Bertschinger [190] in this section and start by writing out the line element in the synchronous gauge

$$\mathrm{d}s^2 = a^2(\tau)\left[-\mathrm{d}\tau^2 + (\delta_{ij} + h_{ij})\,\mathrm{d}x^i \mathrm{d}x^j\right], \tag{3.18}$$

where h_{ij} is the metric perturbation. We work in the Fourier-space k, where k is the wavenumber of the Fourier mode, and where the scalar mode of h_{ij} is characterised by the two scalar fields $h(\vec{k}, \tau)$ and $\eta(\vec{k}, \tau)$ such that

$$h_{ij}(\vec{x}, \tau) = \int d^3k e^{i\vec{k}\cdot\vec{x}} \left(\hat{k}_i\hat{k}_j h(\vec{k}, \tau) + (\hat{k}_i\hat{k}_j - \frac{1}{3}\delta_{ij})6\eta(\vec{k}, \tau)\right), \tag{3.19}$$

where wavevector $\vec{k} = k\hat{k}$ and the trace of the metric perturbation h_{ij} is denoted by h in both real and Fourier space. The zeroth-order energy-momentum tensor is

$$T_{\mu\nu} = (\rho + p)\bar{u}_\mu \bar{u}_\nu + p g_{\mu\nu}, \tag{3.20}$$

where ρ and p are the fluid's energy density and pressure respectively and where $\bar{u}_\mu$ is the zeroth-order four-velocity of the fluid. We now perturb the energy-momentum tensor to obtain its first-order perturbation given by

$$\delta T^\mu{}_\nu = (\delta\rho + \delta p)\,\bar{u}^\mu \bar{u}_\nu + \delta p \delta^\mu{}_\nu + (\rho + p)\,(\delta u^\mu \bar{u}_\nu + \bar{u}^\nu \delta u_\nu) + p\Pi^\mu{}_\nu, \tag{3.21}$$

where δu_μ is the first-order perturbation of the four-velocity and $\Pi_{\mu\nu}$ is the traceless anisotropic stress tensor which we allow for in the perturbed fluid. We now perturb the Einstein field equations to obtain

$$\delta G^\mu_\nu = 8\pi G \sum \delta T^\mu{}_\nu, \tag{3.22}$$

where the sum is over the radiation (r), baryon (b), DM (c), and DE (ϕ) fluids. Thus in k-space, the perturbed Einstein field equations lead to

$$\begin{aligned} k^2\eta - \frac{1}{2}\mathcal{H}h' &= -4\pi G a^2 \sum \delta\rho, \\ k^2\eta' &= 4\pi G a^2 \sum \rho(1+w)\theta, \\ h'' + 2\mathcal{H}h' - 2k^2\eta &= -24\pi G a^2 \sum \delta p, \\ h'' + 6\eta'' + 2\mathcal{H}\,(h' + 6\eta') - 2k^2\eta &= -24\pi G a^2 \sum \rho(1+w)\sigma, \end{aligned} \tag{3.23}$$

where a prime denotes a derivative with respect to conformal time; the sum is over the radiation, baryon, DM, and DE fluids; θ is the divergence of the fluid velocity, and $\sigma = 2w\Pi/3(1+w)$ is the anisotropic shear where Π is given by $\Pi_{ij} = (-\hat{k}_i\hat{k}_j + \frac{1}{3}\delta_{ij})\Pi$ [191].

The first-order perturbation of the conservation equations for the uncoupled

relativistic (r) and baryon (b) species reads

$$\delta T^{(i)\,\mu}{}_{\nu;\mu} = 0, \tag{3.24}$$

which leads to

$$\begin{aligned} \delta_i' + 3\mathcal{H}\left(\frac{\delta p_i}{\delta\rho_i} - w_i\right)\delta_i &= -\left(1+w_i\right)\left(\theta_i + \frac{h'}{2}\right), \\ \theta_i' + \left[\mathcal{H}\left(1-3w_i\right) + \frac{w_i'}{1+w_i}\right]\theta_i &= \frac{\delta p_i}{\delta\rho_i}\frac{k^2\delta_i}{1+w_i} - k^2\sigma_i, \end{aligned} \tag{3.25}$$

where species i is either relativistic (r) or baryonic (b) and where $\delta_i = \delta\rho_i/\rho_i$ is the density contrast for species i. Recall that the equation of state relates the pressure of a fluid to its density and is a constant for relativistic and baryonic fluids such that for the fluid describing radiation we have $w_r = \delta p_r/\delta\rho_r = 1/3$ and for the fluid describing non-relativistic baryons we have $w_b = \delta p_r/\delta\rho_r \ll 1$. Furthermore, the baryons have a vanishing shear stress $\sigma_b = 0$ whilst the shear stress of the radiation fluid cannot be neglected.

Now, for the coupled DM fluid (c) with a general equation of state w_c and vanishing shear $\sigma_c = 0$, recall that the conservation equation has been altered due to an interaction with the DE scalar field. The first-order perturbation equations read therefore [192]

$$\begin{aligned} \delta_c' + 3\mathcal{H}\left(\frac{\delta p_c}{\delta\rho_c} - w_c\right)\delta_c &= -(1+w_c)\left(\theta_c + \frac{h'}{2}\right) + \frac{Q}{\rho_c}\phi'\delta_c - \frac{Q}{\rho_c}\delta\phi' - \frac{\phi'}{\rho_c}\delta Q, \\ \theta_c' + \left[\mathcal{H}(1-3w_c) + \frac{w_c'}{1+w_c}\right]\theta_c &= \frac{\delta p_c}{\delta\rho_c}\frac{k^2\delta_c}{1+w_c} + \frac{Q}{\rho_c}\phi'\theta_c - \frac{Q}{\rho_c(1+w_c)}k^2\delta\phi. \end{aligned} \tag{3.26}$$

For the last species, the DE scalar field ϕ, we perturb the conservation equation, $\delta T^{(\phi)\,\mu}{}_{\nu;\mu} = 0$, to obtain the perturbed Klein-Gordon equation in k-space [193]

$$\delta\phi'' + 2\mathcal{H}\delta\phi' + \left(a^2V_{,\phi\phi} + k^2\right)\delta\phi + \frac{h'}{2}\phi' = a^2\delta Q, \tag{3.27}$$

with the first-order perturbation of the coupling Q reading

$$\delta Q = -\frac{C_{,\phi}}{2C}\rho_c\left(\delta_c\left(1-3\frac{\delta p_c}{\delta\rho_c}\right)+\delta\phi\left(\frac{C_{,\phi\phi}}{C_{,\phi}}(1-3w_c)+\frac{2Q}{\rho_c}\right)\right). \tag{3.28}$$

Thus the perturbation equations for the coupled DM and DE fluids (eqs. (3.26) and (3.27)) now read

$$\begin{aligned}\delta_c'+3\left(\frac{\delta p_c}{\delta\rho_c}-w_c\right)\left(\mathcal{H}+\frac{1}{2}(\ln C)_{,\phi}\phi'\right)\delta_c = \\ -(1+w_c)\left(\theta_c+\frac{h'}{2}\right)+\frac{1}{2}(1-3w_c)\left[(\ln C)_{,\phi}\delta\phi'+(\ln C)_{,\phi\phi}\phi'\delta\phi\right],\end{aligned} \tag{3.29}$$

$$\begin{aligned}\theta_c'+\left[\mathcal{H}(1-3w_c)+\frac{w_c'}{1+w_c}+\frac{1}{2}(\ln C)_{,\phi}(1-3w_c)\phi'\right]\theta_c = \\ k^2\left[\frac{\delta p_c}{\delta\rho_c}\frac{\delta_c}{1+w_c}+\frac{1}{2}(\ln C)_{,\phi}\left(\frac{1-3w_c}{1+w_c}\right)\delta\phi\right],\end{aligned} \tag{3.30}$$

for the coupled DM fluid and

$$\begin{aligned}\delta\phi''+2\mathcal{H}\delta\phi'+\left[k^2+a^2V_{,\phi\phi}+\frac{1}{2}a^2\rho_c(1-3w_c)(\ln C)_{,\phi\phi}\right]\delta\phi = \\ -\frac{1}{2}h'\phi'-\frac{1}{2}a^2\rho_c(\ln C)_{,\phi}\left(1-3\frac{\delta p_c}{\delta\rho_c}\right)\delta_c,\end{aligned} \tag{3.31}$$

for the coupled DE fluid.

3.2.2 NEWTONIAN GAUGE

We now derive the perturbation equations in the conformal Newtonian gauge [194]. To begin, let us start with the line element

$$\mathrm{d}s^2 = a^2(\tau)\left[-(1+2\Psi)\mathrm{d}\tau^2+(1-2\Phi)\delta_{ij}\mathrm{d}x^i\mathrm{d}x^j\right], \tag{3.32}$$

where Ψ and Φ are the scalar potentials. We perturb the field equations to get

$$\begin{aligned} k^2\Phi + 3\mathcal{H}(\Phi' + \mathcal{H}\Psi) &= -4\pi G a^2 \sum \delta\rho, \\ k^2(\Phi' + \mathcal{H}\Psi) &= 4\pi G a^2 \sum \rho(1+w)\theta, \\ \Phi'' + \mathcal{H}(\Psi' + 2\Phi') + \Psi(\mathcal{H}^2 + 2\mathcal{H}') + \frac{k^2}{3}(\Phi - \Psi) &= 4\pi G a^2 \sum \delta p, \\ k^2(\Phi - \Psi) &= 12\pi G a^2 \sum \rho(1+w)\sigma, \end{aligned} \tag{3.33}$$

where the sum is over the radiation (r), baryon (b), DM (c), and DE (ϕ) fluids; and where the shear stress is defined as above in the synchronous gauge case. The perturbed conservation equations for the uncoupled radiation and baryon fluids yield

$$\begin{aligned} \delta_i' + 3\mathcal{H}\left(\frac{\delta p_i}{\delta\rho_i} - w_i\right)\delta_i &= -(1+w_i)(\theta_i - 3\Phi'), \\ \theta_i' + \left[\mathcal{H}(1-3w_i) + \frac{w_i'}{1+w_i}\right]\theta_i &= k^2\left[\Psi + \frac{\delta p_i}{\delta\rho_i}\frac{\delta_i}{1+w_i}\right] - k^2\sigma_i, \end{aligned} \tag{3.34}$$

where species i is either relativistic (r) or baryonic (b). For the coupled DM fluid with equation of state w_c and vanishing shear $\sigma_c = 0$ we obtain

$$\begin{aligned} \delta_c' + 3\mathcal{H}\left(\frac{\delta p_c}{\delta\rho_c} - w_c\right)\delta_c &= -(1+w_c)(\theta_c - 3\Phi') + \frac{Q}{\rho_c}\phi'\delta_c - \frac{Q}{\rho_c}\delta\phi' - \frac{\phi'}{\rho_c}\delta Q, \\ \theta_c' + \left[\mathcal{H}(1-3w_c) + \frac{w_c'}{1+w_c}\right]\theta_c &= k^2\left[\Psi + \frac{\delta p_c}{\delta\rho_c}\frac{\delta_c}{1+w_c}\right] + \frac{Q}{\rho_c}\phi'\theta_c - \frac{Q}{\rho_c(1+w_c)}k^2\delta\phi, \end{aligned} \tag{3.35}$$

and for the coupled DE fluid, the perturbed modified Klein-Gordon equation reads

$$\delta\phi'' + 2\mathcal{H}\delta\phi' + (k^2 + a^2 V_{,\phi\phi})\delta\phi = (\Psi' + 3\Phi')\phi' - 2a^2 V_{,\phi}\Psi + a^2\delta Q + 2a^2 Q\Psi. \tag{3.36}$$

The perturbation of the coupling Q in the Newtonian gauge is [189]

$$\delta Q = -\frac{C_{,\phi}}{2C}\rho_c\left(\delta_c\left(1-3\frac{\delta p_c}{\delta\rho_c}\right)+\delta\phi\left(\frac{C_{,\phi\phi}}{C_{,\phi}}(1-3w_c)+\frac{2Q}{\rho_c}\right)\right), \tag{3.37}$$

which means we may write the perturbation equations for the coupled DM and DE fluids as

$$\begin{aligned}\delta_c'+3\left(\frac{\delta p_c}{\delta\rho_c}-w_c\right)\left(\mathcal{H}+\frac{1}{2}(\ln C)_{,\phi}\phi'\right)\delta_c = \\ -(1+w_c)(\theta_c-3\Phi')+\frac{1}{2}(1-3w_c)\left[(\ln C)_{,\phi}\delta\phi'+(\ln C)_{,\phi\phi}\phi'\delta\phi\right],\end{aligned} \tag{3.38}$$

$$\begin{aligned}\theta_c'+\left[\mathcal{H}(1-3w_c)+\frac{w_c'}{1+w_c}+\frac{1}{2}(\ln C)_{,\phi}(1-3w_c)\phi'\right]\theta_c = \\ k^2\left[\Psi+\frac{\delta p_c}{\delta\rho_c}\frac{\delta_c}{1+w_c}+\frac{1}{2}(\ln C)_{,\phi}\left(\frac{1-3w_c}{1+w_c}\right)\delta\phi\right]\end{aligned} \tag{3.39}$$

for the coupled DM fluid and

$$\begin{aligned}\delta\phi''+2\mathcal{H}\delta\phi'+\left[k^2+a^2V_{,\phi\phi}+\frac{1}{2}a^2\rho_c(1-3w_c)(\ln C)_{,\phi\phi}\right]\delta\phi = \\ (\Psi'+3\Phi')\phi'-\frac{1}{2}a^2\rho_c(\ln C)_{,\phi}\left(1-3\frac{\delta p_c}{\delta\rho_c}\right)\delta_c \\ -a^2\left[2V_{,\phi}+(\ln C)_{,\phi}(1-3w_c)\rho_c\right]\Psi,\end{aligned} \tag{3.40}$$

for the coupled DE fluid.

3.3 SMALL SCALE LIMIT

Let us now look at the small-scale Newtonian limit for the perturbation equations. In particular, let us look at the general case for a coupled fluid with vanishing anisotropic stress, such that $\Psi = \Phi$, and in the Newtonian limit $\hat{\lambda} = \mathcal{H}/k \ll 1$. We arrive at the following equations for the potential Φ and its conformal time

derivative Φ' [195]

$$\Phi \approx -\frac{\hat{\lambda}^2}{2}\left[\frac{\kappa^2}{\mathcal{H}^2}(3\mathcal{H}\phi'\delta\phi + \phi'\delta\phi' + a^2 V_{,\phi}\delta\phi) + 3\sum \Omega_i \delta_i\right], \tag{3.41}$$

$$\Phi' \approx \frac{1}{2}\left(\kappa^2\phi'\delta\phi - 2\mathcal{H}\Phi\right), \tag{3.42}$$

where the sum is over the radiation (r), baryon (b), and coupled DM (c) fluids. In this limit, the coupled DE fluid follows the perturbation equation

$$\delta\phi'' + 2\mathcal{H}\delta\phi' + \mathcal{H}^2\hat{\lambda}^{-2}\delta\phi \approx a^2\delta Q. \tag{3.43}$$

If we apply the small-scale limit to the homogeneous solution of eq. (3.43), we find that this solution has a vanishing contribution after averaging out. Furthermore, if we average over the rapid oscillations of $\delta\phi$, and hence neglect the $\delta\phi'$ and $\delta\phi''$ terms, we are left with an approximate inhomogeneous solution [192]

$$\delta\phi \approx \hat{\lambda}^2 a^2 \mathcal{H}^{-2}\delta Q. \tag{3.44}$$

The perturbation of the coupling Q is now approximated by [188, 196]

$$\delta Q \approx Q\delta_c, \tag{3.45}$$

in this limit, and the gravitational potential Φ by

$$\Phi \approx -\frac{3}{2}\hat{\lambda}^2 \sum \Omega_i \delta_i, \tag{3.46}$$

where the sum is over the radiation (r), baryon (b), and coupled DM (c) fluids.

The density contrast perturbation equation for the coupled DM fluid now reads

$$\delta_c'' + \mathcal{H}_{\rm eff}\delta_c' - \frac{3}{2}\mathcal{H}^2\frac{G_{\rm eff}}{G}\Omega_c\delta_c = \frac{3}{2}\mathcal{H}^2(\Omega_b\delta_b + \Omega_r\delta_r), \tag{3.47}$$

where the coupled DM fluid experiences an effective Hubble parameter and effective gravitational constant given by [188]

$$\mathcal{H}_{\rm eff} = \mathcal{H} - \frac{Q}{\rho_c}\phi', \quad G_{\rm eff} = G\left(1 + \frac{2}{\kappa^2}\frac{Q^2}{\rho_c^2}\right), \tag{3.48}$$

thus the damping term in the evolution equation for the coupled DM density contrast perturbations (eq. (3.47)) and the effective gravitational constant are altered in the presence of a dark sector interaction and depend on the strength of the coupling. One feature to note is that the effective gravitational constant $G_{\rm eff}$ is enhanced regardless of the sign of Q, meaning that the fifth-force between DM particles is always attractive.

3.4 General imprints on background and perturbation level cosmology

Let us now briefly discuss some of the intriguing features of the coupled quintessence (CQ) model, how it differs from ΛCDM and uncoupled quintessence (UQ) models, and how it may be constrained using cosmological observations. To begin, we must first specify the two new functions that the coupled quintessence field introduces, namely the conformal coupling function $C(\phi)$ and the scalar field potential $V(\phi)$. A widely-studied form for the conformal coupling function and scalar field potential that arises naturally in many fundamental theories, such as in supergravity [197, 198] and string theory [199], is the exponential form. These read

$$C(\phi) = e^{2\alpha\phi/M_{\rm Pl}}, \quad V(\phi) = V_0^4 e^{-\lambda\phi/M_{\rm Pl}}, \tag{3.49}$$

where the conformal coupling constant α, the slope of the scalar field potential $\lambda > 0$, and the mass scale V_0 are all constants. In this setup, the effective gravitational constant between DM particles (eq. (3.48)) is constant, and the mass scale for the potential V_0 is obtained via a shooting mechanism in order to satisfy the constraint equation (eq. (1.42)). Therefore, the IDE model introduces two new independent parameters, the coupling constant α and slope of the potential λ. We have implemented the background and perturbation equations for the interacting dark energy model into a modified version of the `CLASS` [61] Boltzmann code and

use cosmological parameter values from the 2018 *Planck* [50] bestfit results for the baseline model where appropriate in order to obtain the numerical results for the plots and tables in this section. Note that although we have implemented the perturbation equations in both the synchronous gauge and Newtonian gauge, we use the synchronous gauge for calculations in this section and for the rest of this thesis. To be concrete, these are the present-day reduced baryon density parameter $\Omega_b h^2 = 0.02236$, the present-day reduced cold dark matter density parameter $\Omega_{\rm cdm} h^2 = 0.1202$, the angular size of the sound horizon at decoupling $100\theta_s = 1.04090$, the amplitude of the primordial curvature power spectrum $\ln(10^{10} A_s) = 3.045$, the spectral index of the primordial curvature power spectrum $n_s = 0.9649$, and the optical depth at reionisation $\tau_{\rm reio} = 0.0544$, where h is the reduced Hubble constant defined by $H_0 = 100h\,{\rm kms}^{-1}{\rm Mpc}^{-1}$ and where the cosmological parameters are as defined in section 1.2.3.

First, let us look at the background dynamics of the theory. One of the key features of the coupled quintessence model is that the interaction between the scalar field and dark matter can be seen to result in an energy exchange between the two components (eqs. (3.13) and (3.14)). Through the Friedmann equations (eqs. (3.15) and (3.16)), the coupled quintessence model can be seen to affect expansion history as shown in Figure 3.1, where we plot the ratio of the Hubble parameter to its present-day value H_0 for the ΛCDM, UQ, and CQ models. In the upper panel we plot the CQ model in the $\alpha > 0$ regime and in the lower panel we plot the CQ model in the $\alpha < 0$ regime. The slope of the potential λ is set to $\lambda = 0.5$ in the UQ and CQ models, with the uncoupled quintessence model being equivalent to a coupled quintessence model with $\alpha = 0$. We see in Figure 3.1 that the uncoupled quintessence model deviates only slightly from the ΛCDM model, whereas in the CQ models, both in the $\alpha > 0$ and $\alpha < 0$ case, the expansion history deviates more significantly, with the deviation increasing with coupling strength $|\alpha|$. This altered expansion history directly affects background measurements such as distance measurements. Relevant background measurements that are impacted by the presence of a dark sector interaction include the angular diameter distance $D_A(z)$ (eq. (1.55)) and the luminosity distance $D_L(z)$,

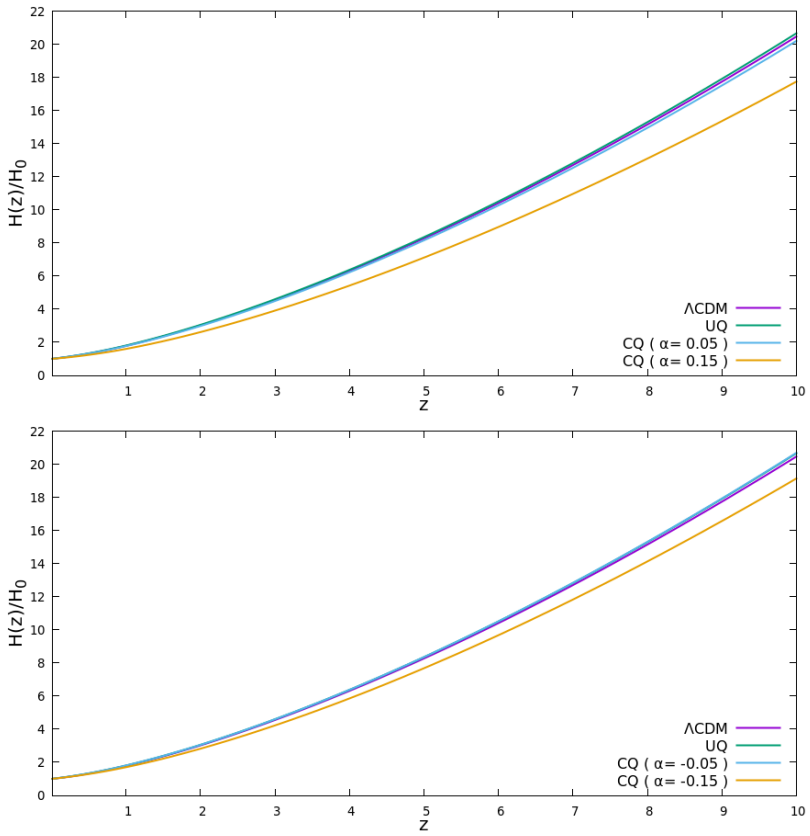

Figure 3.1: The evolution of the Hubble parameter $H(z)$ normalised by its present-day value H_0 for the ΛCDM, UQ, and CQ models. Four CQ models are chosen with different values picked for the conformal coupling constant α as appearing in eq. (3.49). In the upper panel we plot the $\alpha > 0$ case and in the lower panel we plot the $\alpha < 0$ case for the CQ models. The slope of the scalar field potential is set to $\lambda = 0.5$ in the UQ and CQ models.

which is related to the angular diameter distance by

$$D_L(z) = (1+z)^2 D_A(z). \tag{3.50}$$

Background observations such as BAO measurements [93] and SNIa distance measurements [94] can therefore help to constrain this interacting dark energy model and indeed will be used in subsequent chapters where we perform data analysis on variety of IDE models.

Owing to an energy exchange in the dark sector, the DM fluid no longer scales

like the baryon fluid. From the viewpoint of the action, the introduction of this coupling results in the masses of the DM particles m_{DM} to become dependent on the scalar field [171] such that

$$m_{DM}(\phi) \propto \sqrt{C(\phi)}, \tag{3.51}$$

and so if $C(\phi)$ grows then the masses of the DM particles grow and if $C(\phi)$ decreases, then the masses of the DM particles also decrease. Alternatively, we may look at the continuity equation for the coupled DM fluid (eq. (3.14)) and find that

$$\rho_c = \rho_{c,0}\sqrt{C(\phi)}\, a^{-3}, \tag{3.52}$$

in contrast to uncoupled baryonic matter where the energy density scales like $\rho_b = \rho_{b,0}\, a^{-3}$. If the conformal coupling function decreases with the scale factor, then the DM fluid dilutes faster than baryons, whereas if the coupling increases with the scale factor, then the DM fluid dilutes slower than baryons.

One of the effects this altered scaling of the DM energy density has on the background level is that if one assumes the interacting DM fluid scales like baryons, then the effective DE fluid can appear to have phantom-like behaviour with an equation of state $w < -1$ [200]. In the context of the Friedmann equation (eq. (3.15)), we may define an effective DE fluid which absorbs the part of the DM fluid that does not scale like $\rho \propto a^{-3}$ and then investigate its equation of state. Writing out the first Friedmann equation (eq. (3.15)) we have

$$\begin{aligned}
\mathcal{H}^2 &= \frac{\kappa^2}{3}a^2\left(\rho_r + \rho_b + \rho_c + \rho_\phi\right) \\
&= \frac{\kappa^2}{3}a^2\left(\rho_r + \rho_b + \rho_{c,0}a^{-3} + \rho_\phi + \rho_c - \rho_{c,0}a^{-3}\right) \\
&= \frac{\kappa^2}{3}a^2\left(\rho_r + \rho_b + \rho_{c,0}a^{-3} + \rho_{DE}\right),
\end{aligned} \tag{3.53}$$

where we have defined the energy density of the effective DE fluid to be $\rho_{DE} :=$

$\rho_\phi + \rho_c - \rho_{c,0}a^{-3}$. The equation of state for this effective DE fluid is

$$\begin{aligned} w_{DE} &= \frac{p_\phi}{\rho_{DE}} \\ &= \frac{p_\phi}{\rho_\phi + \rho_c - \rho_{c,0}a^{-3}}, \end{aligned} \tag{3.54}$$

and so, in the presence of a dark sector interaction, the equation of state of the effective DE fluid, w_{DE}, deviates from the equation of state of the scalar field $w_\phi = p_\phi/\rho_\phi$ in the general case. The equation of state of the quintessence scalar field is given by

$$\begin{aligned} w_\phi &= p_\phi/\rho_\phi \\ &= \frac{\phi'^2/(2a^2) - V(\phi)}{\phi'^2/(2a^2) + V(\phi)}, \end{aligned} \tag{3.55}$$

where we have used $p_\phi = \phi'^2/(2a^2) - V(\phi)$ and $\rho_\phi = \phi'^2/(2a^2) + V(\phi)$ for the pressure and energy density of the scalar field respectively. One can see that, for a general quintessence scalar field, the equation of state is bounded below by $w_\phi \geq -1$ and therefore avoids the phantom condition $w < -1$. However, for the effective DE fluid, the equation of state w_{DE} now has an altered lower bound depending on how the coupled DM fluid scales. In the case where $\alpha > 0$, it is possible to achieve $w_{DE} < -1$ for the effective DE fluid at some earlier point in cosmic history.

In Figure 3.2 we plot the effective DE equation of state parameter w_{DE} for the ΛCDM model which we define to be $w_{DE} := -1$, the uncoupled quintessence, and the coupled quintessence models. We see that in the lower panel of Figure 3.2, that the CQ($\alpha < 0$) models have a less negative equation of state when compared to the UQ model, however, in the upper panel of Figure 3.2, for the CQ($\alpha > 0$) model, the effective equation of state for the CQ models crosses the phantom line $w_{DE} < -1$ in both cases. Note that the possibility of an actual phantom fluid existing is disfavoured because it would violate the null energy condition [201]. It has therefore been suggested [200] that if cosmological observations seem to indicate a preference for a phantom-like dark energy fluid in earlier cosmic history

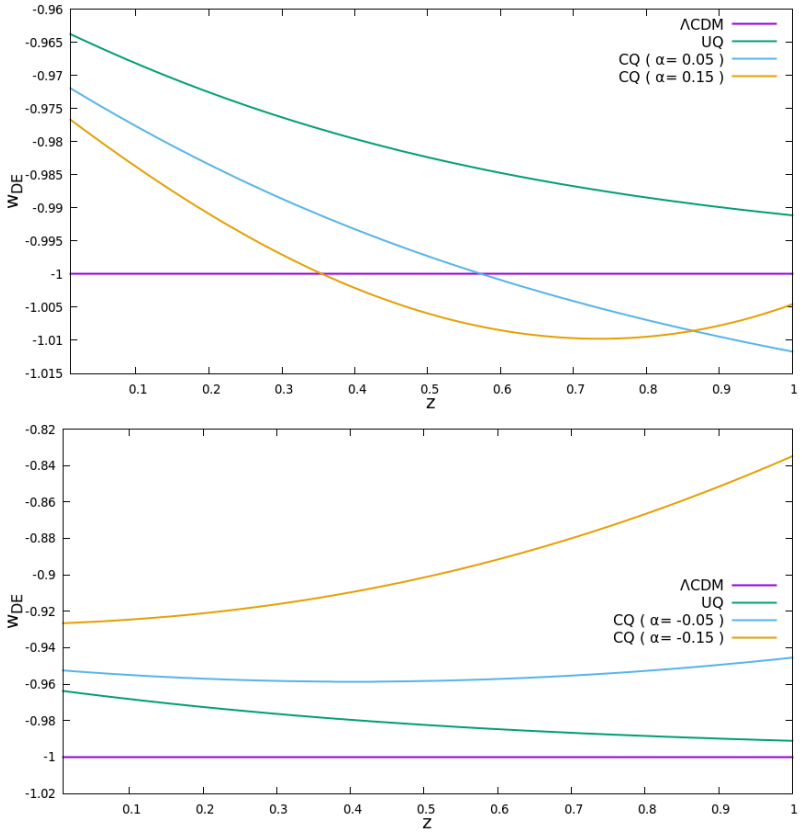

Figure 3.2: The evolution of the effective DE equation of state parameter $w_{DE}(z)$ for the ΛCDM, UQ, and CQ models. Four CQ models are chosen with different values picked for the conformal coupling constant α as appearing in eq. (3.49). In the upper panel we plot the $\alpha > 0$ case and in the lower panel we plot the $\alpha < 0$ case for the CQ models. Note that the effective DE equation of state, w_{DE}, in the CQ($\alpha > 0$) models crosses the phantom line $w = -1$. The slope of the scalar field potential is set to $\lambda = 0.5$ in the UQ and CQ models.

$w(z) < -1$, then this is strongly indicative of an interacting dark sector, thus making the determination of the evolution history of the dark energy equation of state parameter an area of utmost importance in present-day cosmology [202].

The DE-dependent scaling of the DM energy density alters the ratio of the baryon to DM energy density throughout cosmic history, including at photon decoupling, and therefore the DE-DM coupling directly affects the CMB anisotropies [162]. Some of the immediate effects the coupling has on the CMB temperature anisotropies power spectrum include a shifting of peaks due to an altered sound

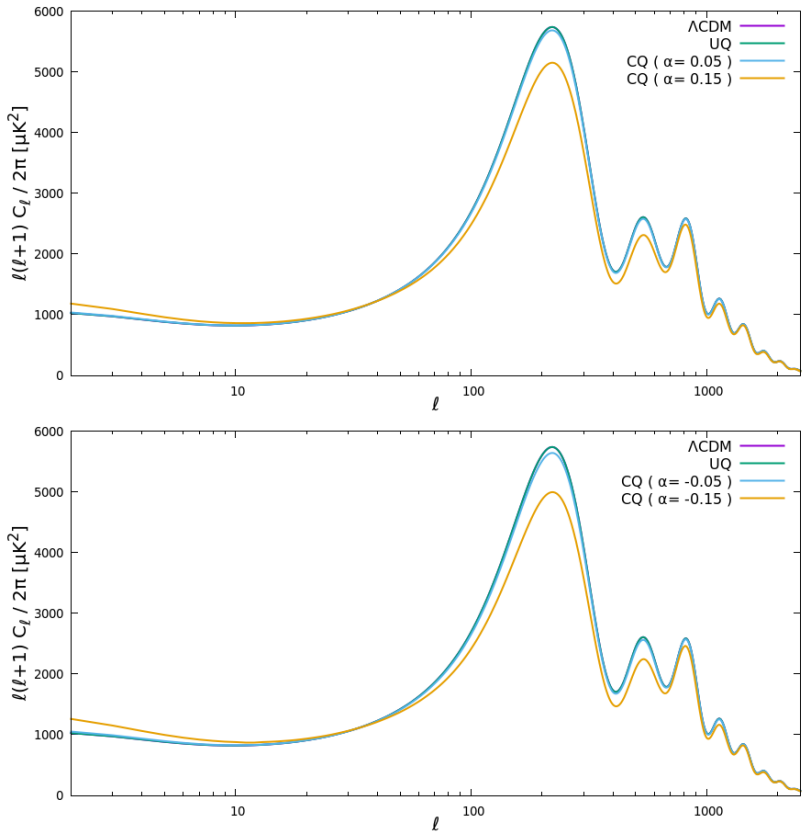

Figure 3.3: The CMB temperature anisotropy power spectrum for the ΛCDM, UQ, and CQ models where C_ℓ is the power spectrum of the anisotropies in units μK^2 and ℓ is the multipole moment [3]. Four CQ models are chosen with different values picked for the conformal coupling constant α as appearing in eq. (3.49). In the upper panel we plot the $\alpha > 0$ case and in the lower panel we plot the $\alpha < 0$ case for the CQ models. The slope of the scalar field potential is set to $\lambda = 0.5$ in the UQ and CQ models.

horizon and a change in amplitude of the peaks due to change in growth history, as well as an integrated Sachs-Wolfe effect [203, 193]. In Figure 3.3 we plot the CMB temperature anisotropies for the ΛCDM, uncoupled quintessence, and coupled quintessence models. We clearly see in Figure 3.3 that the coupling has a distinctive effect on the CMB temperature anisotropy power spectrum. The uncoupled quintessence model is in good agreement with ΛCDM, however, the CQ models deviate from the ΛCDM model with the deviation increasing with coupling strength $|\alpha|$ in both the $\alpha > 0$ and $\alpha < 0$ case. Through the distinctive

Model	ΔG %	σ_8
ΛCDM	0	0.824
UQ	0	0.818
CQ ($\alpha = -0.05$)	0.50	0.854
CQ ($\alpha = 0.05$)	0.50	0.853
CQ ($\alpha = -0.15$)	4.5	1.23
CQ ($\alpha = 0.15$)	4.5	1.21

Table 3.1: The values of ΔG and σ_8 for the ΛCDM, UQ, and CQ models where $\Delta G := (G_{\text{eff}}/G) - 1$ describes the enhancement of the effective gravitational constant compared to the Newtonian gravitational constant. Four CQ models are chosen with different values picked for the conformal coupling constant α as appearing in eq. (3.49). Note that the effective gravitational constant experienced between DM particles, G_{eff}, does not depend on the direction of energy transfer between DE and DM, and that the stronger the coupling, the greater the amount of matter clustering. The slope of the scalar field potential is set to $\lambda = 0.5$ in the UQ and CQ models.

imprints coupled quintessence has on the CMB anisotropies, we may use observations of the CMB anisotropies, as measured by *Planck* [50] for example, to constrain this coupled quintessence model.

The introduction of the coupling results in the growth of matter being enhanced at small scales, thus resulting in a larger σ_8 when compared to uncoupled models [193]. We may see this effect by comparing the matter power spectrum for the ΛCDM, uncoupled quintessence, and coupled quintessence models as in Figure 3.4. We can see that when compared to ΛCDM and uncoupled quintessence, the coupled quintessence models have an enhancement in power at smaller scales, with the enhancement increasing with an increase in coupling strength $|\alpha|$. One measure of the amplitude of structure is the σ_8 parameter mentioned in section 2.2 which provides a normalisation for the linear-theory matter power spectrum.

In Table 3.1 we report the derived values of σ_8 for the ΛCDM, UQ, and CQ models, as well as the percentage enhancement of the effective gravitational constant compared to the Newtonian gravitational constant where $\Delta G := (G_{\text{eff}}/G) - 1$. We see that the coupled models have an enhanced σ_8 compared to the uncoupled quintessence model, with the enhancement increasing with $|\alpha|$ in both the $\alpha < 0$ and $\alpha > 0$ case, therefore the introduction of the coupling has

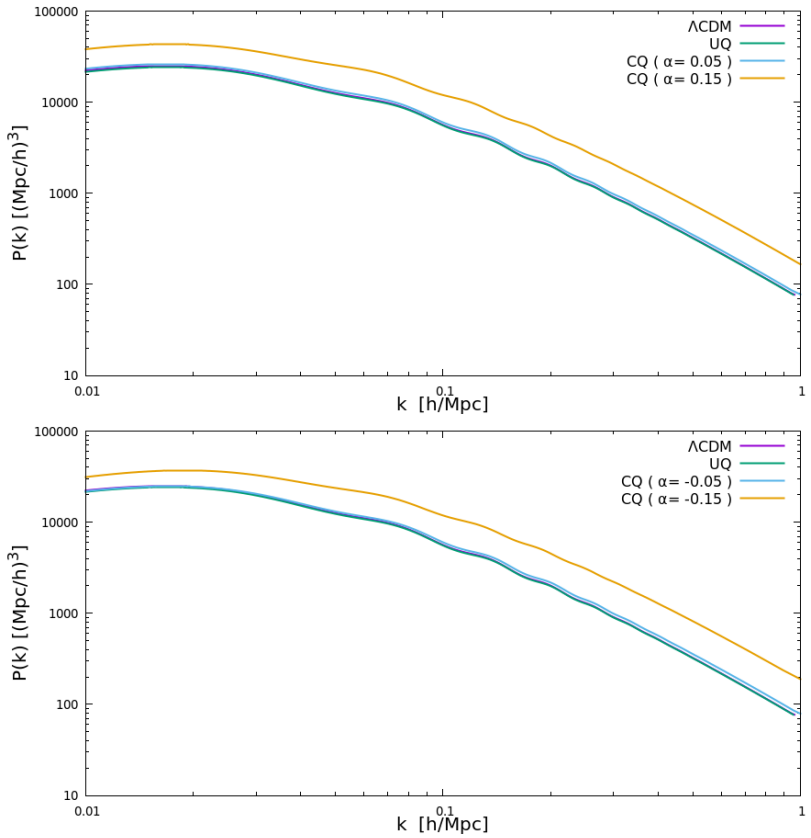

Figure 3.4: The present-day matter power spectrum for the ΛCDM, UQ, and CQ models where $P(k)$ is the matter power spectrum in units $(\mathrm{Mpc}/h)^3$ and k is the wavenumber in units h/Mpc with h being the dimensionless Hubble parameter defined in eq. (1.50). Four CQ models are chosen with different values picked for the conformal coupling constant α as appearing in eq. (3.49). In the upper panel we plot the $\alpha > 0$ case and in the lower panel we plot the $\alpha < 0$ case for the CQ models. Note the enhancement in power for the CQ models in both the $\alpha > 0$ and $\alpha < 0$ case. The slope of the scalar field potential is set to $\lambda = 0.5$ in the UQ and CQ models.

a distinctive effect on large-scale structure (LSS) in the universe. Cosmological observations providing information on the growth and amplitude of structure, such as LSS data from cosmic shear experiments [72, 73, 74] and galaxy cluster measurements [204], may therefore be used in cosmological data analysis in order to further constrain this IDE model.

We have briefly seen how the introduction of a coupling between DM and DE affects cosmological imprints on the background and perturbation level, and

how these imprints can help us to constrain the IDE model using cosmological observations such as from CMB, BAO, SNIa, and LSS measurements. Although we have only briefly examined these effects at a surface level, more in-depth and thorough treatments on the imprints of IDE exist in literature, for example in [193, 205, 206, 192, 207, 208, 209, 210, 211, 212, 196, 188, 213, 214, 215].

3.5 Conclusions

In this chapter, we introduced a general coupled quintessence model where the DE scalar field is coupled directly to DM. In our formulation, we begin with an action where the DM sector is described by a DE-dependent metric which is related to the minimally-coupled metric through a conformal coupling. The evolution equations for the uncoupled radiation and baryon fluids are unaltered, however, the conservation equations for the coupled DM and DE fluids are modified thus reflecting an energy exchange between the two fluids.

We then looked at the evolution of perturbations in the case of an uncoupled radiation and baryonic sector, and a DM sector coupled to a quintessence scalar field, finding that at small scales, the damping term in the density contrast evolution equation for the coupled DM fluid is altered and the effective Newtonian gravitational constant is enhanced.

Finally, we looked at some of the cosmological imprints of the IDE model at the background and perturbation level, finding that distinctive observationally relevant imprints exist, for example, in the CMB anisotropies, distance measurements, and LSS measurements. We are now at a stage where we may probe these interacting dark energy models using cosmological observations and constrain them to see if indeed there are any hints of an interaction in the dark sector.

4 — Constraints on interacting dark energy

Given the current bounty of high precision cosmological data, we are able to comprehensively explore cosmological models at a wide range of different points in the cosmic history of our universe [216]. From these observations, we discovered the need for two new ingredients in its makeup, the cosmological constant Λ and cold dark matter (CDM), together forming two vital components in the standard model of cosmology, the ΛCDM model [50]. In chapter 2, we saw that, despite its many successes, this model is plagued by some issues surrounding Λ which has led cosmologists to search for alternative explanations for dark energy.

One of the most well-motivated explanations for dark energy is a quintessence scalar field [165], which should theoretically be allowed to couple to the various energy species of our universe if it exists [155]. We saw that whilst couplings to baryons have been heavily constrained [186], the same is not true with couplings to dark matter [187]. We therefore introduced an interacting dark energy model with an interacting dark sector in chapter 3 and explored its evolution at the background and perturbation level, as well as some imprints it may have on observationally relevant cosmological probes. We found that the IDE model does affect background and perturbation level probes in a distinct way, and therefore it is natural that we should seek to constrain this model using cosmological data to see if there are any signals of a dark sector interaction.

In section 4.1 we introduce the interacting dark energy model and then in section 4.2 we describe our methodology and the data sets used in our cosmological

data analysis. We present the results of our parameter exploration in section 4.3, finally concluding in section 4.4.

4.1 Interacting dark energy model

In this chapter, we consider two specific models based on the general IDE model introduced in chapter 3. The first is the IDE model seen in section 3.4 where the conformal coupling function and scalar field potential take on an exponential form. This model will be denoted as **M1** henceforth and is specified by

$$C(\phi) = e^{2\alpha\phi/M_{\rm Pl}} \,, \quad V(\phi) = V_0^4 e^{-\lambda\phi/M_{\rm Pl}} \,, \tag{4.1}$$

where the conformal coupling constant α, the slope of the scalar field potential $\lambda > 0$, and the mass scale V_0 are all constants. In the case where $\alpha > 0$, this model is called $\mathbf{M1}^+$, and in the case where $\alpha < 0$, this model is called $\mathbf{M1}^-$.

The second model we consider is where the conformal coupling function takes on an exponential form, however, the scalar field potential is now of an inverse power-law form. This form of potential has a long history in quintessence models, appearing in one of the seminal 1988 papers by Peebles and Ratra [217]. The inverse power-law potential admits "tracker" solutions [218] which help to alleviate the coincidence problem, and further, this form of potential can be motivated from fundamental particle physics theories such as in supersymmetry [219]. To be concrete, this IDE model, which will be denoted as **M2** henceforth, is specified by

$$C(\phi) = e^{2\alpha\phi/M_{\rm Pl}}, \quad V(\phi) = V_0^4 \left(\frac{\phi}{M_{\rm Pl}}\right)^{-\lambda} \,, \tag{4.2}$$

where the conformal coupling constant α, the slope of the scalar field potential $\lambda > 0$, and the mass scale V_0 are all constants. In the case where $\alpha > 0$, this model is called $\mathbf{M2}^+$, and in the case where $\alpha < 0$, this model is called $\mathbf{M2}^-$.

In this setup, the effective gravitational constant between DM particles is constant and the mass scale for the potential V_0 is obtained via a shooting mechanism in order to satisfy the constraint equation (eq. (1.42)) in both IDE models.

Note that in M1, the initial value of the scalar field when simulations begin, $\phi_{\rm ini} = \phi(a_{\rm ini})$ where $a_{\rm ini} = 10^{-14}$, plays no role in the evolution equations, with varying $\phi_{\rm ini}$ being equivalent to varying V_0 which is shot for, therefore we fix $\phi_{\rm ini} = 1 M_{\rm Pl}$ without loss of generality. Hence M1 introduces two extra parameters, the conformal coupling parameter α and slope of the potential λ. In M2, however, $\phi_{\rm ini}$ does play a role and so is allowed to vary as an independent parameter. Thus M2 introduces three extra parameters, the coupling parameter α, slope of the potential λ, and initial scalar field value $\phi_{\rm ini}$.

4.2 METHODOLOGY AND OBSERVATIONAL DATA

In order to numerically study the evolution of the background and cosmological perturbations for the IDE model, we use a modified version of the `CLASS` code [61] as seen in section 3.4. We confront the IDE model with data through cosmological parameter exploration using the Markov Chain Monte Carlo (MCMC) sampling package `MontePython` [220, 221], interfaced with `CLASS`, in conjunction with the observational data sets outlined below. In addition to this, the `GetDist` [222] Python package is used to analyse the MCMC chains and produce the values and plots of the parameter constraints in section 4.3. Finally, in order to statistically compare the different cosmological models and determine which model has the greatest support for it in light of data, we calculate the Bayes factor of an IDE model relative to the ΛCDM model by using the `MCEvidence` code [223].

The Bayes factor gives a measure of the level of support for one model over another and intrinsically accounts for additional degrees of freedom, therefore making it a useful tool in statistical model comparison [224]. The Bayes factor of a model i relative to the ΛCDM model is given by [224]

$$B_{i,\,\Lambda\rm CDM} = \frac{P(\mathcal{D}|\, i\,)}{P(\mathcal{D}|\Lambda\rm CDM)}\,, \tag{4.3}$$

where $\mathcal{D}$ is a given data set, and where $P(\mathcal{D}|\, i\,)$ and $P(\mathcal{D}|\Lambda\rm CDM)$ are the so-called evidences for models i and ΛCDM respectively. Therefore, the greater

$\ln B_{i,\Lambda\mathrm{CDM}}$	Evidence
0 to 1.1	Weak
1.1 to 3.0	Definite
3.0 to 5.0	Strong
> 5.0	Very strong

Table 4.1: Jeffreys' scale, which is used here to interpret the strength of evidence for model i over ΛCDM.

the evidence for model i relative to ΛCDM, the greater the Bayes factor. We may translate the numerical Bayes factor into a qualitative statement about the strength of evidence against ΛCDM by using Jeffreys' scale [225], which is a scale giving an interpretation based on the size of the Bayes factor. Often, this is quantified in terms of the natural logarithm of the Bayes factor and we will be adopting this convention in this chapter. We display Jeffreys' scale in Table 4.1, where we note that if $\ln B_{i,\Lambda\mathrm{CDM}} < 0$ for a model, then there is no evidence of support for that model over ΛCDM.

In our analysis, M1 is described by a set of eight parameters and M2 by a set of nine parameters. The six ΛCDM parameters are the reduced baryon energy density $\Omega_b h^2$, the reduced CDM energy density $\Omega_{cdm} h^2$, the ratio of the sound horizon to the angular diameter distance at decoupling θ_s, the scalar amplitude of the primordial power spectrum A_s, the scalar spectral index n_s, and the reionisation optical depth τ_{reio}, where h is the reduced Hubble constant defined by $H_0 = 100h\mathrm{kms}^{-1}\mathrm{Mpc}^{-1}$. The IDE models introduce the conformal coupling parameter α, the slope of the scalar field potential λ, and the initial value of the scalar field ϕ_{ini}. The flat priors for the ΛCDM, M1$^{\pm}$, and M2$^{\pm}$ model parameters are shown in Table 4.2. We also report constraints on several important derived parameters in section 4.3. The derived parameters of interest are the Hubble constant H_0, the present-day mass fluctuation amplitude in spheres of radius $8h^{-1}\mathrm{Mpc}$ σ_8, and the total matter density parameter Ω_m.

We use combinations of the following recent observational data sets in order

Parameter	Prior (ΛCDM)	Prior (M1$^-$)	Prior (M1$^+$)	Prior (M2$^-$)	Prior (M2$^+$)
$\Omega_b h^2$	$[0.005, 0.1]$	$[0.005, 0.1]$	$[0.005, 0.1]$	$[0.005, 0.1]$	$[0.005, 0.1]$
$\Omega_c h^2$	$[0.001, 0.99]$	$[0.001, 0.99]$	$[0.001, 0.99]$	$[0.001, 0.99]$	$[0.001, 0.99]$
$100\theta_s$	$[0.5, 10]$	$[0.5, 10]$	$[0.5, 10]$	$[0.5, 10]$	$[0.5, 10]$
$\tau_{\rm reio}$	$[0.01, 0.8]$	$[0.01, 0.8]$	$[0.01, 0.8]$	$[0.01, 0.8]$	$[0.01, 0.8]$
n_s	$[0.7, 1.3]$	$[0.7, 1.3]$	$[0.7, 1.3]$	$[0.7, 1.3]$	$[0.7, 1.3]$
$\ln(10^{10} A_s)$	$[1.7, 5.0]$	$[1.7, 5.0]$	$[1.7, 5.0]$	$[1.7, 5.0]$	$[1.7, 5.0]$
α	–	$[-1, 0]$	$[0, 1]$	$[-1, 0]$	$[0, 1]$
λ	–	$[0, 5]$	$[0, 5]$	$[0, 5]$	$[0, 5]$
$\phi_{\rm ini}/M_{\rm Pl}$	–	–	–	$[0, 50]$	$[0, 50]$

Table 4.2: Flat priors for the cosmological parameters sampled in our analysis in the ΛCDM, M1$^\pm$ and M2$^\pm$ models.

to analyse and constrain the models in question:

- **Cosmic Microwave Background:**

  We use the full TTTEEE+lowE CMB likelihood from the latest Planck 2018 release [50]. This includes temperature (TT) and polarisation (EE) anisotropy data as well as cross-correlation data between temperature and polarisation (TE) at high and low multipoles. We denote this dataset as **PL18** in this chapter.

- **Baryon Acoustic Oscillations:**

  We saw in section 1.2.3 that prior to photon decoupling, baryons and photons were tightly coupled to form a single oscillating fluid. These oscillations left distinct imprints in the baryon density field which can be seen today in the clustering of galaxies as measured by large-scale surveys [226]. Since the physical size of these oscillations can be theoretically predicted and the angular size measured, a distance to BAO signals can be inferred, thus

BAO can be used as standard rulers in cosmology [226]. If we measure the redshift of a given BAO signal, then we are able to map out points in the redshift-distance relation of our universe and hence use BAO data to help constrain cosmological models. We consider BAO measurements coming from BOSS DR12 [227], 6dFGS [228], and SDSS-MGS [229] surveys for use in our analysis. We denote this dataset as **BAO** in this chapter.

- **Type Ia Supernovae:**

  Type Ia Supernovae can be used as standard candles through the fact that their absolute magnitude M can be inferred through theoretical predictions and physical measurements [230]. We may then measure the apparent magnitude m of the supernovae and deduce a luminosity distance [231]. If we measure the redshift of a given type Ia supernovae signal, then we are able to map out points in the redshift-distance relation of our universe and hence use supernovae type Ia data to help constrain cosmological models. We use the Pantheon data catalog consisting of 1048 points in the region $z \in [0.01, 2.3]$ of SNIa luminosity distance data as provided by [232]. We denote this dataset as **Pantheon** in this chapter.

4.3 Results

The results of our data analysis are shown in Tables 4.3 to 4.7 where we report the parameter constraints for the ΛCDM, M1$^{\pm}$, and M2$^{\pm}$ models using the PL18, PL18+BAO, PL18+Pantheon, and PL18+BAO+Pantheon data set combinations for each model, apart from in the M2^{+} model where the PL18 only run did not converge. In Figures 4.1 and 4.3 we display 2D marginalised posterior distributions for the conformal coupling parameter α in the M1 and M2 models where in the upper and lower panels, we display the $\alpha < 0$ and $\alpha > 0$ cases respectively. Furthermore, in Figures 4.2 and 4.4 we plot the 1D marginalised posterior distributions for the conformal coupling parameter α and slope of the potential λ in the M1 and M2 models, where again in the upper and lower panels we display the $\alpha < 0$ and $\alpha > 0$ cases respectively. For the $\alpha < 0$ models in

Parameter	PL18	PL18+BAO	PL18 + Pantheon	PL18 + BAO + Pantheon
$\Omega_b h^2$	0.02237±0.00015	0.02242±0.00013	0.02239±0.00014	0.02243±0.00013
$\Omega_{cdm} h^2$	0.1202 ± 0.0014	0.1193 ± 0.0010	0.1199 ± 0.0013	0.11923±0.00097
$100\theta_s$	1.04188±0.00029	1.04197±0.00028	1.04192±0.00029	1.04196±0.00028
τ_{reio}	$0.0547^{+0.0071}_{-0.0080}$	$0.0557^{+0.0072}_{-0.0081}$	0.0551 ± 0.0079	0.0560 ± 0.0079
n_s	0.9654 ± 0.0044	0.9673 ± 0.0038	0.9660 ± 0.0042	0.9676 ± 0.0037
$\ln(10^{10} A_s)$	3.046 ± 0.016	3.046 ± 0.016	3.046 ± 0.016	3.047 ± 0.017
H_0	67.33 ± 0.60	67.70 ± 0.44	67.47 ± 0.57	67.75 ± 0.43
σ_8	0.8118 ± 0.0075	0.8094 ± 0.0072	0.8109 ± 0.0075	0.8093 ± 0.0073
Ω_m	0.3160 ± 0.0084	0.3107 ± 0.0060	0.3141 ± 0.0079	0.3101 ± 0.0058

Table 4.3: Observational constraints at a 68% confidence level on the independent and derived cosmological parameters for the ΛCDM model using the PL18, PL18+BAO, PL18+Pantheon, PL18+BAO +Pantheon data set combinations. The quantities in the second half of this table are the derived parameters of our analysis which are the Hubble constant H_0 in units $\mathrm{km\,s^{-1}\,Mpc^{-1}}$, the present-day mass fluctuation amplitude in spheres of radius $8h^{-1}$Mpc σ_8, and the total matter density parameter Ω_m.

Figures 4.1 to 4.4, we plot the absolute value of the conformal coupling constant, $|\alpha|$, for ease of comparison with constraints coming from the $\alpha > 0$ case. In Figure 4.5 we combine into single plots the 1D marginalised posterior distributions for the absolute value of the coupling parameter $|\alpha|$ and slope of the potential λ in all the M1 and M2 models, using the full PL18+BAO+Pantheon data set combination. In Figure 4.6 we plot the 1D marginalised posterior distributions of the Hubble constant, H_0, in the ΛCDM, M1$^{\pm}$, and M2^{-} models using the PL18 data set, and also a recent local distance ladder measurement of H_0 [4]. Finally, in Table 4.8 we report the percentage enhancement of the present-day effective gravitational constant for the ΛCDM, M1$^{\pm}$, and M2$^{\pm}$ models using the 95% confidence limit of the conformal coupling parameter α from runs using the full PL18+BAO+Pantheon data set combination.

We run the MCMC chains until they have converged, with all parameters

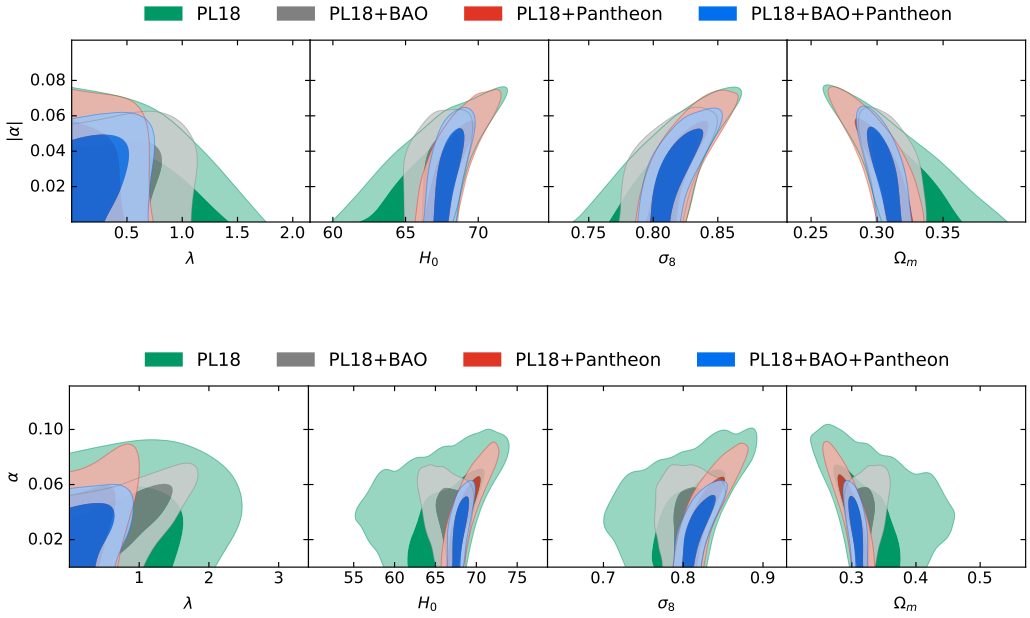

Figure 4.1: 2D marginalised posterior distributions of parameters in the M1$^-$ model (upper panel) and M1$^+$ model (lower panel) using the PL18, PL18+BAO, PL18+Pantheon, PL18+BAO+Pantheon data set combinations. We plot the 2D marginalised posterior distributions of the conformal coupling parameter, α, against the slope of the potential, λ, the Hubble constant in units $\mathrm{km\,s^{-1}\,Mpc^{-1}}$, H_0, the present-day mass fluctuation amplitude in spheres of radius $8h^{-1}$Mpc, σ_8, and the total matter density parameter, Ω_m. The shaded contours indicate the 1σ and 2σ confidence limits.

achieving a Gelman-Rubin statistic [233] of $|R-1| < 0.03$, where R is the Gelman-Rubin statistic. All the chains converged except in the case of the M2$^+$ model using the PL18 data set, therefore, we exclude this run from our results. We will first discuss the M1 model, which possesses an exponential conformal coupling function and exponential potential, then look at the M2 model, which possesses an exponential conformal coupling function and inverse power-law potential, finally concluding by comparing the two models and assessing their viability in light of our analysis.

4.3.1 Exponential coupling and exponential potential

We begin by observing that the ΛCDM model is excellently constrained by PL18 data alone, as well as with the addition of background data sets, with the six

Parameter	PL18	PL18+BAO	PL18 + Pantheon	PL18 + BAO + Pantheon
$\Omega_b h^2$	0.02235 ± 0.00015	0.02239 ± 0.00015	0.02237 ± 0.00015	0.02239 ± 0.00015
$\Omega_{cdm} h^2$	$0.1185^{+0.0027}_{-0.0015}$	$0.1178^{+0.0018}_{-0.0012}$	$0.1179^{+0.0026}_{-0.0015}$	$0.1179^{+0.0016}_{-0.0011}$
$100\theta_s$	1.04187 ± 0.00030	1.04191 ± 0.00029	1.04189 ± 0.00030	1.04190 ± 0.00028
τ_{reio}	0.0550 ± 0.0080	0.0554 ± 0.0081	$0.0547^{+0.0071}_{-0.0080}$	0.0554 ± 0.0077
n_s	0.9656 ± 0.0044	0.9671 ± 0.0039	0.9666 ± 0.0043	0.9670 ± 0.0040
$\ln(10^{10} A_s)$	3.047 ± 0.016	3.047 ± 0.017	3.046 ± 0.016	3.047 ± 0.016
λ	< 0.829	< 0.659	< 0.364	< 0.408
α	> -0.0322	$-0.028^{+0.022}_{-0.013}$	> -0.0409	-0.030 ± 0.016
H_0	$66.5^{+2.2}_{-1.8}$	$67.3^{+1.1}_{-0.80}$	$68.14^{+0.77}_{-1.3}$	67.98 ± 0.69
σ_8	0.808 ± 0.023	0.811 ± 0.015	$0.820^{+0.010}_{-0.018}$	$0.817^{+0.011}_{-0.015}$
Ω_m	$0.321^{+0.021}_{-0.024}$	$0.3110^{+0.0094}_{-0.011}$	$0.304^{+0.016}_{-0.010}$	$0.3052^{+0.0087}_{-0.0079}$
$\ln B_{i,\Lambda\mathrm{CDM}}$	-4.64	-4.64	-5.58	-5.38

Table 4.4: Observational constraints at a 68% confidence level on the independent and derived cosmological parameters for the M1$^-$ model using the PL18, PL18+BAO, PL18+Pantheon, PL18+BAO+Pantheon data set combinations. The quantities in the second half of this table are the derived parameters of our analysis which are the Hubble constant H_0 in units $\mathrm{km\,s^{-1}\,Mpc^{-1}}$, the present-day mass fluctuation amplitude in spheres of radius $8h^{-1}$Mpc σ_8, and the total matter density parameter Ω_m. In the last row, we report the natural logarithm of the Bayes factor with respect to the ΛCDM model, $\ln B_{i,\Lambda\mathrm{CDM}}$, as defined by eq. (4.3).

ΛCDM parameters and derived parameters, apart from τ_{reio}, being constrained to within a few percent precision as can be seen in Table 4.3. We remark that the parameter constraints that we derived for the ΛCDM model are in agreement with the constraints as derived by the *Planck* team [50].

We see in Tables 4.4 and 4.5 that whilst PL18 data alone favours a coupling α consistent with zero at 1σ for the M1 model, the addition of background data sets, such as BAO and Pantheon, allow for greater values of the coupling $|\alpha|$ in both the M1$^\pm$ models, except for the M1$^+$ model when using the PL18+BAO+Pantheon

Parameter	PL18	PL18+BAO	PL18 + Pantheon	PL18 + BAO + Pantheon
$\Omega_b h^2$	0.02235 ± 0.00015	0.02239 ± 0.00015	0.02236 ± 0.00015	0.02238 ± 0.00014
$\Omega_{cdm} h^2$	$0.1193^{+0.0026}_{-0.0015}$	0.1190 ± 0.0011	$0.1182^{+0.0022}_{-0.0015}$	0.1188 ± 0.0010
$100\theta_s$	1.04185 ± 0.00030	1.04190 ± 0.00029	1.04187 ± 0.00030	1.04190 ± 0.00029
τ_{reio}	$0.0548^{+0.0071}_{-0.0081}$	$0.0551^{+0.0073}_{-0.0083}$	0.0553 ± 0.0080	0.0555 ± 0.0080
n_s	0.9662 ± 0.0047	0.9670 ± 0.0040	0.9667 ± 0.0042	0.9667 ± 0.0040
$\ln\left(10^{10} A_s\right)$	$3.047^{+0.015}_{-0.016}$	3.046 ± 0.017	3.047 ± 0.016	3.047 ± 0.017
λ	< 1.26	$0.81^{+0.41}_{-0.60}$	< 0.510	< 0.477
α	< 0.0464	0.035 ± 0.018	$0.038^{+0.017}_{-0.030}$	0.029 ± 0.016
H_0	$65.8^{+3.8}_{-2.3}$	$66.8^{+1.8}_{-0.94}$	$68.59^{+0.88}_{-1.6}$	$68.02^{+0.62}_{-0.74}$
σ_8	$0.801^{+0.036}_{-0.024}$	$0.807^{+0.018}_{-0.016}$	$0.826^{+0.011}_{-0.022}$	$0.818^{+0.011}_{-0.015}$
Ω_m	$0.333^{+0.022}_{-0.045}$	$0.3190^{+0.0098}_{-0.018}$	$0.301^{+0.018}_{-0.011}$	$0.3068^{+0.0084}_{-0.0074}$
$\ln B_{i,\Lambda\mathrm{CDM}}$	-4.12	-3.93	-5.21	-5.01

Table 4.5: Observational constraints at a 68% confidence level on the independent and derived cosmological parameters for the M1$^+$ model using the PL18, PL18+BAO, PL18+Pantheon, PL18+BAO+Pantheon data set combinations. The quantities in the second half of this table are the derived parameters of our analysis which are the Hubble constant H_0 in units $\mathrm{km\,s^{-1}\,Mpc^{-1}}$, the present-day mass fluctuation amplitude in spheres of radius $8h^{-1}$Mpc σ_8, and the total matter density parameter Ω_m. In the last row, we report the natural logarithm of the Bayes factor with respect to the ΛCDM model, $\ln B_{i,\Lambda\mathrm{CDM}}$, as defined by eq. (4.3).

data set combination. Indeed, for the M1$^-$ model, we are able to derive 1σ lower bounds for $|\alpha|$ using the PL18+BAO and PL18+BAO+Pantheon data sets, and for the M1$^+$ model, we are able to derive 1σ lower bounds for all combinations of the background data sets. We can see this effect in Figure 4.2 where the addition of the background data sets results in a non-zero peak for the absolute value of the conformal coupling parameter $|\alpha|$. Using the full PL18+BAO+Pantheon data set combination, the conformal coupling parameter α is constrained to be $|\alpha| = 0.030 \pm 0.016$ at 1σ in the M1$^-$ model and $\alpha = 0.029 \pm 0.016$ at 1σ in the

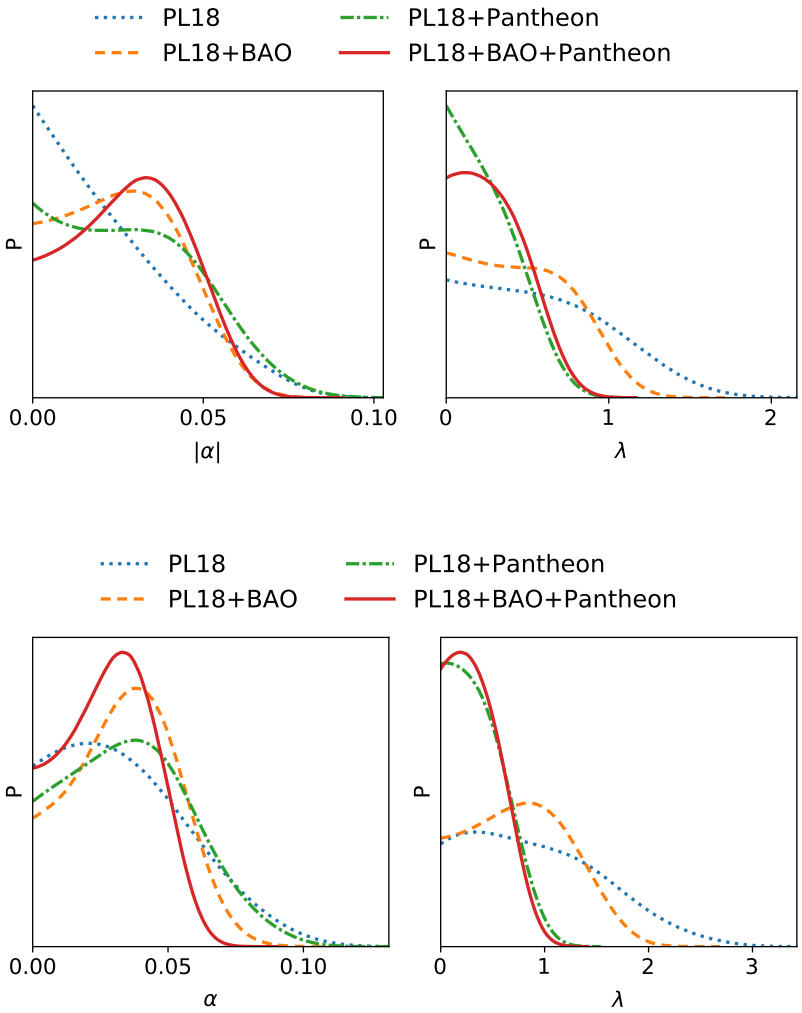

Figure 4.2: 1D marginalised posterior distributions of the coupling parameter, α, and slope of the potential, λ, in the M1$^-$ model (upper panel) and M1$^+$ model (lower panel) using the PL18, PL18+BAO, PL18+Pantheon, PL18+BAO+Pantheon data set combinations, where p is the normalised probability density.

M1$^+$ model.

We do not derive a lower bound for the slope of the potential, λ, in the M1 model except when using the PL18+BAO data set in the M1$^+$ model. We see in Tables 4.4 and 4.5 that the addition of background data sets results in λ being constrained closer to zero, with larger values of λ being allowed in the M1$^+$

model. We can see this behaviour in Figure 4.2 where the additional background data sets can be seen to have quite a strong constraining effect on λ. Using the full PL18+BAO+Pantheon data set combination, the slope of the potential λ is constrained to be $\lambda < 0.408$ at 1σ in the M1$^-$ model and $\lambda < 0.477$ at 1σ in the M1$^+$ model. So we see that the absolute value of the coupling constant, $|\alpha|$, and slope of the scalar field potential, λ, are both constrained to a similar range of values in the M1$^\pm$ models when using the full PL18+BAO+Pantheon data set combination.

In Figure 4.1 we plot the 2D marginalised posterior distributions for the conformal coupling parameter α against λ, H_0, σ_8, and Ω_m. In both the M1$^+$ and M1$^-$ models, there exists a positive correlation in the $(|\alpha|, H_0)$ and $(|\alpha|, \sigma_8)$ plane, and a negative correlation in the $(|\alpha|, \Omega_m)$ plane. Moreover, the scalar field parameters $|\alpha|$ and λ appear to be positively correlated in the M1$^\pm$ models, except in the PL18 only runs. The positive correlation between $|\alpha|$ and H_0 can help ease the H_0 tension discussed in section 2.2. The tension between a recent local measurement of $H_0 = 74.03 \pm 1.42\,\mathrm{km\,s^{-1}\,Mpc^{-1}}$ at 1σ [4] and the derived value of H_0 using PL18 data, as in Table 4.3, is a troubling $\sim 4.3\sigma$. This tension is reduced to $\sim 2.9\sigma$ in the M1$^-$ model and $\sim 2.0\sigma$ in the M1$^+$ model. Note, however, that the mean values of H_0 in the M1 models, as shown in Tables 4.4 and 4.5, are actually lower than in the ΛCDM model using PL18 data alone. The tension is reduced as a result of the error bars associated with H_0 being larger in the M1 models, since H_0 is not as well constrained in the M1 models as in ΛCDM.

Although the absolute value of the coupling constant, $|\alpha|$, is positively correlated with the σ_8 parameter, as discussed in section 3.4, the mean values of σ_8 in the M1 models are actually lower than in ΛCDM, although the 1σ error bars associated with this parameter are wider in the M1 models. We find that this decrease in σ_8 is compensated by an increase in Ω_m when using PL18 data, thus the S_8 parameter is not significantly changed in the M1$^\pm$ models. The M1$^+$ model reports a value of $S_8 = 0.839 \pm 0.022$ at 1σ and the M1$^-$ model a value of $S_8 = 0.834 \pm 0.018$ at 1σ, which do not significantly differ from the ΛCDM derived value of $S_8 = 0.833 \pm 0.016$ at 1σ. A full data analysis and comparison

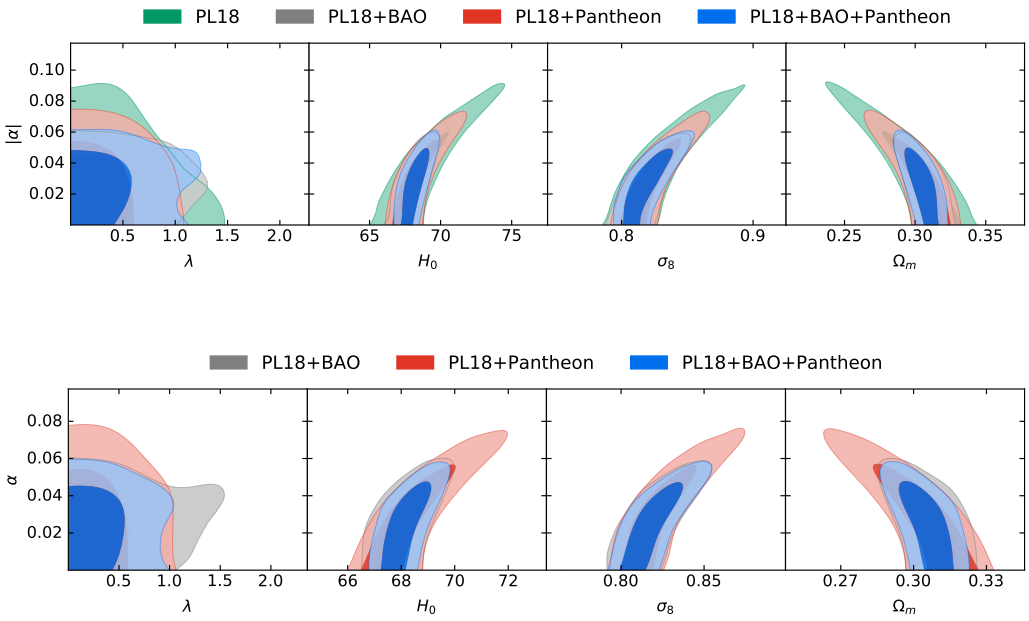

Figure 4.3: 2D marginalised posterior distributions of parameters in the M2$^-$ model (upper panel) and M2$^+$ model (lower panel) using the PL18, PL18+BAO, PL18+Pantheon, PL18+BAO+Pantheon data set combinations, excluding PL18 for the M2$^+$ model. We plot the 2D marginalised posterior distributions of the conformal coupling parameter, α, against the slope of the potential, λ, the Hubble constant in units $\mathrm{km\,s^{-1}\,Mpc^{-1}}$, H_0, the present-day mass fluctuation amplitude in spheres of radius $8h^{-1}$Mpc, σ_8, and the total matter density parameter, Ω_m. The shaded contours indicate the 1σ and 2σ confidence limits.

with cosmic shear data [72, 73, 74] is necessary, however, before anything more definitive can be said about this model's effect on the S_8 tension.

Finally, we see in Tables 4.4 and 4.5 that the logarithm of the Bayes factor, $\ln B_{i,\Lambda\mathrm{CDM}}$, is negative for all data set combinations, indicating that there is no evidence of support for the M1 models over the ΛCDM model. The M1$^+$ model has, however, a modestly less negative Bayes factor than the M1$^-$ model for all data sets, indicating a very slight preference over the M1$^-$ model. Clearly, the introduction of two extra scalar field parameters, α and λ, into the cosmological model is not enough to account for the increase in model complexity.

Parameter	PL18	PL18+BAO	PL18 + Pantheon	PL18 + BAO + Pantheon
$\Omega_b h^2$	0.02237 ± 0.00015	0.02238 ± 0.00014	0.02236 ± 0.00015	0.02238 ± 0.00014
$\Omega_{cdm} h^2$	$0.1183^{+0.0030}_{-0.0014}$	0.1188 ± 0.0012	$0.1185^{+0.0021}_{-0.0013}$	$0.1186^{+0.0012}_{-0.0011}$
$100\theta_s$	1.04187 ± 0.00030	1.04191 ± 0.00028	1.04187 ± 0.00029	1.04191 ± 0.00028
τ_{reio}	$0.0550^{+0.0072}_{-0.0084}$	0.0553 ± 0.0081	0.0551 ± 0.0076	0.0547 ± 0.0074
n_s	0.9663 ± 0.0045	0.9663 ± 0.0040	0.9662 ± 0.0041	0.9661 ± 0.0038
$\ln\left(10^{10} A_s\right)$	3.047 ± 0.016	3.047 ± 0.016	3.047 ± 0.016	3.046 ± 0.015
λ	< 0.459	< 0.484	< 0.458	< 0.463
α	> -0.0385	$-0.025^{+0.021}_{-0.011}$	> -0.0379	-0.027 ± 0.015
H_0	$68.42^{+0.72}_{-1.8}$	68.05 ± 0.71	$68.32^{+0.62}_{-1.3}$	$68.21^{+0.58}_{-0.71}$
σ_8	$0.8240^{+0.0083}_{-0.021}$	$0.8185^{+0.0096}_{-0.013}$	$0.8229^{+0.0092}_{-0.018}$	$0.8194^{+0.0092}_{-0.015}$
Ω_m	$0.303^{+0.022}_{-0.010}$	0.3063 ± 0.0084	$0.304^{+0.016}_{-0.0086}$	$0.3045^{+0.0085}_{-0.0073}$
$\ln B_{i,\Lambda\mathrm{CDM}}$	-5.22	-5.12	-5.28	-5.40

Table 4.6: Observational constraints at a 68% confidence level on the independent and derived cosmological parameters for the M2$^-$ model using the PL18, PL18+BAO, PL18+Pantheon, PL18+BAO+Pantheon data set combinations. The quantities in the second half of this table are the derived parameters of our analysis which are the Hubble constant H_0 in units $\mathrm{km\,s^{-1}\,Mpc^{-1}}$, the present-day mass fluctuation amplitude in spheres of radius $8h^{-1}$Mpc σ_8, and the total matter density parameter Ω_m. In the last row, we report the natural logarithm of the Bayes factor with respect to the ΛCDM model, $\ln B_{i,\Lambda\mathrm{CDM}}$, as defined by eq. (4.3).

4.3.2 Exponential coupling and inverse power-law potential

We see in Tables 4.6 and 4.7 that whilst PL18 data alone favours a coupling α consistent with zero at 1σ for the M2$^-$ model, the addition of the BAO and BAO+Pantheon data sets give a non-null coupling at 1σ, finding that $\alpha = -0.025^{+0.021}_{-0.011}$ and $\alpha = -0.027 \pm 0.015$ respectively. In the M2$^+$ model, we were not able to obtain convergence using PL18 data alone, however, we similarly detect a non-null coupling at 1σ with the addition of the BAO and BAO+Pantheon data sets, finding that $\alpha = 0.025^{+0.012}_{-0.020}$ and $\alpha = 0.026^{+0.014}_{-0.019}$ respectively.

Parameter	PL18+BAO	PL18 + Pantheon	PL18 + BAO + Pantheon
$\Omega_b h^2$	0.02238 ± 0.00014	0.02237 ± 0.00015	0.02238 ± 0.00015
$\Omega_{cdm} h^2$	0.1190 ± 0.0011	$0.1185^{+0.0021}_{-0.0014}$	0.1188 ± 0.0011
$100\theta_s$	1.04190 ± 0.00029	1.04189 ± 0.00029	1.04191 ± 0.00029
τ_{reio}	$0.0550^{+0.0073}_{-0.0082}$	0.0546 ± 0.0082	0.0554 ± 0.0079
n_s	0.9663 ± 0.0038	0.9664 ± 0.0041	0.9666 ± 0.0039
$\ln(10^{10} A_s)$	$3.047^{+0.015}_{-0.017}$	3.046 ± 0.017	3.047 ± 0.016
λ	< 0.500	< 0.450	< 0.451
α	$0.025^{+0.012}_{-0.020}$	< 0.0387	$0.026^{+0.014}_{-0.019}$
H_0	68.05 ± 0.70	$68.44^{+0.67}_{-1.4}$	$68.19^{+0.52}_{-0.67}$
σ_8	$0.818^{+0.010}_{-0.014}$	$0.8232^{+0.0086}_{-0.018}$	$0.8195^{+0.0091}_{-0.014}$
Ω_m	0.3068 ± 0.0083	$0.303^{+0.016}_{-0.0093}$	$0.3051^{+0.0079}_{-0.0070}$
$\ln B_{i,\Lambda\text{CDM}}$	-5.12	-5.08	-5.36

Table 4.7: Observational constraints at a 68% confidence level on the independent and derived cosmological parameters for the M2$^+$ model using the PL18+BAO, PL18+Pantheon, PL18+BAO+Pantheon data set combinations. The quantities in the second half of this table are the derived parameters of our analysis which are the Hubble constant H_0 in units $\mathrm{km\,s^{-1}\,Mpc^{-1}}$, the present-day mass fluctuation amplitude in spheres of radius $8h^{-1}$Mpc σ_8, and the total matter density parameter Ω_m. In the last row, we report the natural logarithm of the Bayes factor with respect to the ΛCDM model, $\ln B_{i,\Lambda\text{CDM}}$, as defined by eq. (4.3).

In Figure 4.4 we see that the addition of the BAO data gives rise to a strong non-zero peak in $|\alpha|$ that is preserved with the addition of the Pantheon data set in both the M2$^+$ and M2$^-$ models. Again, we see that a similar magnitude of coupling is allowed in either case, with $\alpha = -0.027 \pm 0.015$ and $\alpha = 0.026^{+0.014}_{-0.019}$ at 1σ using the full PL18+BAO+Pantheon data set combination for the M2$^-$ and M2$^+$ models respectively.

We do not derive a lower bound at 1σ for the slope of the potential, λ, in the M2$^\pm$ models in any combination of data sets. We can see in Table 4.6 that

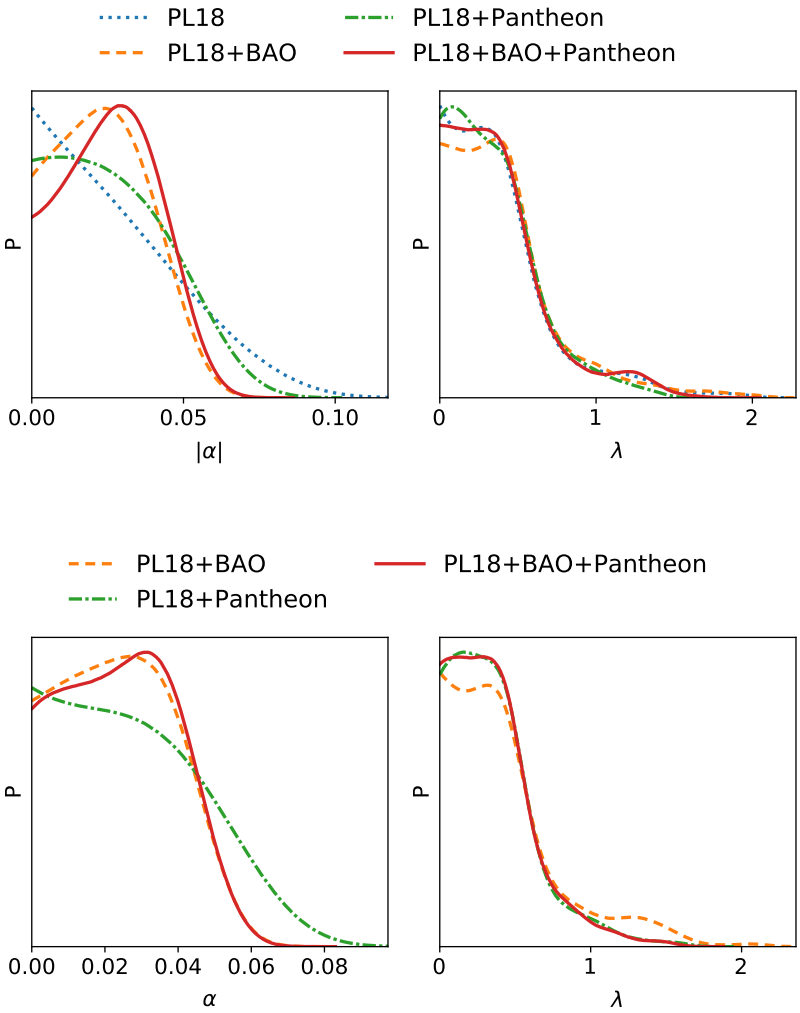

Figure 4.4: 1D marginalised posterior distributions of the coupling parameter, α, and slope of the potential, λ, in the M2$^-$ model (upper panel) and M2$^+$ model (lower panel) using the PL18, PL18+BAO, PL18+Pantheon, PL18+BAO+Pantheon data set combinations, excluding PL18 for the M2$^+$ model, where p is the normalised probability density.

the addition of background data sets has little effect in constraining λ in the M2$^-$ model, with PL18 data alone constraining the slope of the potential to be $\lambda < 0.459$ and the full PL18+BAO+Pantheon data set combination constraining the slope of the potential to be $\lambda < 0.463$ both at 1σ. For the M2$^+$ model, we find a similar constraint when using the full PL18+BAO+Pantheon data set

combination of $\lambda < 0.451$ at 1σ. We can see this behaviour for the M2$^-$ model in the upper panel of Figure 4.4 where we see that adding background data has a minimal effect on the 1D marginalised posterior distribution of λ. For the M2$^+$ model, we can look to the lower panel of Figure 4.4 and see that the distribution of λ has a similar profile to when in the M2$^-$ model. The absolute value of the coupling constant, $|\alpha|$, and slope of the scalar field potential, λ, are both constrained to a similar range of values in the M2$^\pm$ models when using the full PL18+BAO+Pantheon data set combination.

In Figure 4.3 we plot the 2D marginalised posterior distributions for the conformal coupling parameter α against λ, H_0, σ_8, and Ω_m. In both the M2$^\pm$ models, there exists a positive correlation in the $(|\alpha|, H_0)$ and $(|\alpha|, \sigma_8)$ plane, and a negative correlation in the $(|\alpha|, \Omega_m)$ plane. Unlike in the M1$^\pm$ models, the scalar field parameters $|\alpha|$ and λ do not appear to be correlated. The positive correlation between the conformal coupling parameter $|\alpha|$ and Hubble constant H_0 can help ease the H_0 tension as was the case in the M1$^\pm$ models. The M2$^-$ model reduces the tension from $\sim 4.3\sigma$ to $\sim 3.5\sigma$ when using PL18 data, thus easing the tension by a lesser degree than the M1$^\pm$ models. Note, however, that unlike the M1$^\pm$ models, the M2$^-$ model actually raises the mean value of H_0 compared to the ΛCDM model, as can be seen by comparing Table 4.3 with Table 4.6, although the constraint on H_0 derived in the M2$^-$ model has smaller error bars than in the M1$^\pm$ models, hence is not as effective at lowering the tension according to the formula given in eq. (2.12).

Unlike the M1$^\pm$ models, we derive larger mean values for the σ_8 parameter in the M2$^\pm$ models compared to ΛCDM for all data set combinations. For the M2$^\pm$ models, we find a lower mean value of the matter density Ω_m when compared to ΛCDM. The effect of the increase in σ_8 and decrease in Ω_m roughly cancel each other out in the S_8 parameter, thus the derived value of $S_8 = 0.827 \pm 0.018$ at 1σ in the M2$^-$ model does not significantly differ from the ΛCDM value of $S_8 = 0.833 \pm 0.016$ at 1σ using PL18 data. Again, data analysis using cosmic shear data [72, 73, 74] is needed before more can be said about this model's effect on the S_8 tension.

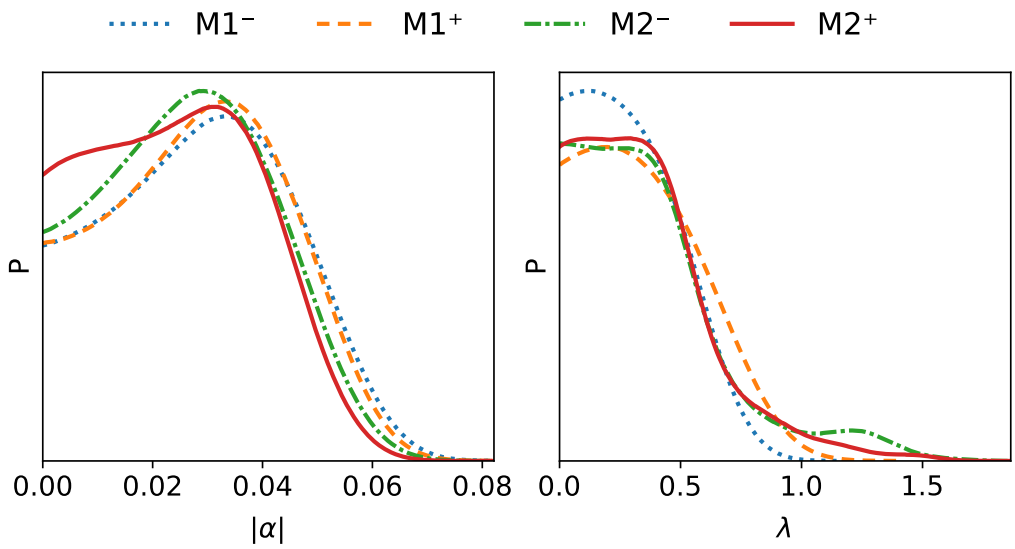

Figure 4.5: 1D marginalised posterior distributions of the coupling parameter, α, and slope of the potential, λ, in the M1$^{\pm}$ and M2$^{\pm}$ models using the PL18+BAO+Pantheon data set combination, where p is the normalised probability density.

Finally, we see in Tables 4.6 and 4.7 that the logarithm of the Bayes factor, $\ln B_{i,\Lambda\mathrm{CDM}}$, is negative for all data set combinations, indicating that there is no evidence of support for the M2 models over the ΛCDM model. The M2$^+$ model has a minutely less negative Bayes factor than the M2$^-$ model for all data sets considered, thus indicating a very small preference over the M2$^-$ model. The introduction of three extra degrees of freedom, α, λ, and ϕ_{ini}, is not enough to account for the increase in model complexity and thus the M2$^{\pm}$ models are disfavoured when compared to the six parameter ΛCDM model.

4.3.3 Comparing the two models

In Figure 4.5 we combine into single plots the 1D marginalised posterior distributions for the absolute value of the coupling parameter, $|\alpha|$, and slope of the potential, λ, in all the M1 and M2 models, using the full PL18+BAO+Pantheon data set combination. We see in Figure 4.5 that all the models have a similar profile for $|\alpha|$, with all models achieving a non-null coupling signal at 1σ when using

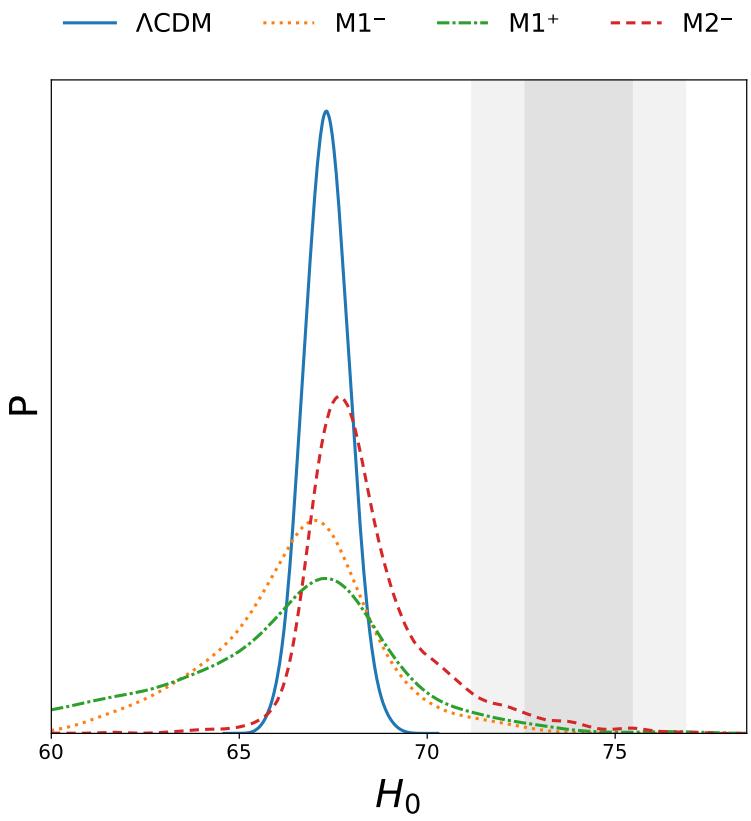

Figure 4.6: 1D marginalised posterior distributions of the Hubble constant H_0 in units $\mathrm{km\,s^{-1}\,Mpc^{-1}}$ in the ΛCDM, M1$^{\pm}$, and M2^{-} models using the PL18 data set, where p is the normalised probability density. The grey bands indicate the 1σ and 2σ errors of a recent local distance ladder measurement of $H_0 = 74.03 \pm 1.42\,\mathrm{km\,s^{-1}\,Mpc^{-1}}$ at 1σ [4]

the PL18+BAO+Pantheon data set combination. Clearly, not only does the sign of the coupling constant α not significantly change the profile of the distribution of $|\alpha|$, but neither does the form of the scalar field potential for the two models under consideration. Furthermore, we see that, despite M1 and M2 possessing different forms of potential, the profile of the distribution of λ is similar in all the models. We do not detect a non-null value of λ at 1σ for any of the models, except for the M1^{+} model when using the PL18+BAO data set combination.

In Figure 4.6 we plot the 1D marginalised posterior distributions of the Hubble constant, H_0, in the ΛCDM, M1$^{\pm}$, and M2^{-} models using the PL18 data set, and also a recent local distance ladder measurement of $H_0 = 74.03 \pm$

Model	ΔG %
ΛCDM	0
M1$^-$	0.63
M1$^+$	0.60
M2$^-$	0.54
M2$^+$	0.49

Table 4.8: Percentage enhancement of the present-day effective gravitational constant compared to the Newtonian gravitational constant for the ΛCDM, M1$^\pm$, and M2$^\pm$ models using the 95% confidence limit for coupling parameter α from PL18+BAO+Pantheon data set runs, where $\Delta G := (G_{\text{eff},0}/G) - 1$.

1.42 km s^{-1} Mpc^{-1} at 1σ [4] as indicated by the grey bands, where the grey bands depict the 1σ and 2σ errors. It can be seen in this figure that whilst it is only the M2$^-$ model that actually raises the mean value of H_0 with respect to the derived ΛCDM mean value, the M1$^\pm$ models possess a much wider error in H_0 and hence there is a greater overlap with the local distance ladder measurement distribution of H_0. The constraint on H_0 inferred from the M2$^-$ model is tighter than in the M1$^\pm$ models, however, is not as well constrained as in the ΛCDM model.

In all models, the natural logarithm of the Bayes factor with respect to the ΛCDM model, $\ln B_{i,\Lambda\text{CDM}}$, is negative, thus indicating that ΛCDM is preferred over models M1 and M2. Of all the models, the M1$^+$ model when using the PL18+BAO data set combination has the least negative Bayes factor of $\ln B_{i,\Lambda\text{CDM}} = -3.93$, and the M1$^-$ model when using the PL18+Pantheon data set combination has the most negative Bayes factor of $\ln B_{i,\Lambda\text{CDM}} = -5.58$.

As a closing remark, let us look at the magnitude of the present-day effective gravitational constant experienced between DM particles, $G_{\text{eff},0}$, for the IDE models in question. The effective gravitational constant, G_{eff}, (eq. (3.48)) is given by

$$\frac{G_{\text{eff}}}{G} = 1 + \frac{M_{\text{Pl}}^2}{2}\left(\frac{C_{,\phi}}{C}\right)^2, \tag{4.4}$$

where G is the Newtonian gravitational constant and $C = C(\phi)$ is the conformal

coupling function relating the DM metric to the minimally-coupled metric. For the choice of conformal coupling function in models M1 and M2, G_{eff} is constant and is given by $G_{\text{eff}}/G = 1 + 2\alpha^2$, where α is the conformal coupling constant. In Table 4.8 we evaluate the percentage enhancement of the effective gravitational constant for the ΛCDM, M1$^{\pm}$, and M2$^{\pm}$ models. The value chosen for the conformal coupling constant, α, in the IDE models is the upper 95% confidence limit in models M1^{+} and M2^{+} and the lower 95% confidence limit in models M1^{-} and M2^{-}, when using the full PL18+BAO+Pantheon data set. We can see that cosmological data constrains all of the IDE models to have a sub-percentage enhancement in the effective gravitational constant when using the 95% confidence limits for the coupling parameter α. Thus, if there is an interaction in the dark sector, then a coupling which results in a constant and time-independent effective gravitational constant is constrained to be quite weak at $< 1\%$ the strength of gravity.

4.4 Conclusions

In this chapter, we considered an interacting dark energy model where the DE scalar field is coupled directly to DM, as explored in chapter 3. We then considered two specific IDE models, one with an exponential coupling and exponential potential, the other with an exponential coupling and inverse power-law potential. We confronted these models with a combination of cosmological data sets and derived constraints on the cosmological parameters. We found that, when using the full PL18+BAO+Pantheon data set combination, a weak non-null signal of a DE-DM coupling was detected in all IDE models at 1σ. Furthermore, we found that in all IDE models, the slope of the potential λ was consistent with zero at 1σ when using the full PL18+BAO+Pantheon data set combination. In all the IDE models and for all data set combinations, cosmological observations are still consistent with a null coupling and flat potential at 2σ.

The IDE models were able to ease the H_0 tension, but this effect was mainly due to an increase in uncertainty surrounding the H_0 parameter in the IDE

models. If the H_0 parameter was as well constrained in the IDE models as it is in the ΛCDM model, then the IDE models would not significantly help to solve the H_0 tension. Moreover, we did not find any evidence of support for the IDE models over the ΛCDM model through our Bayesian model comparison analysis, finding that $\ln B_{i,\Lambda\mathrm{CDM}} < 0$ for all IDE models.

Finally, we looked at how large a present-day effective gravitational constant the IDE models allow compared to the Newtonian gravitational constant, using the 95% confidence limits on the conformal coupling parameter α for the full PL18+BAO+Pantheon data set combination. We found that, in all cases, the fifth-force is constrained to be quite weak at $< 1\%$ the strength of gravity.

There is no fundamental reason, however, to restrict ourselves to a dark sector coupling that results in a constant effective gravitational constant. Indeed, if we choose a conformal coupling function that results in a time-varying G_{eff}, then we will be able to escape some of the rigid constraints that cosmological data imposes on models with a constant G_{eff}, such as M1 and M2. In an effort to avoid a purely phenomenological form for the coupling function $C(\phi)$, we may look to see if fundamental theory can motivate a new class of couplings in which a fifth-force emerges at late-times. In the next chapter, we will explore such a class of couplings and will evaluate their status in light of recent cosmological observations.

5 — Couplings with minima

The quintessence scalar field is an extremely promising candidate for dark energy and its potential interactions with other matter sources, particularly dark matter, remains an exciting area of study with the search for a fifth-force in the dark sector continuing to be at the forefront of modern cosmology [234]. In chapter 4 we confronted an interacting dark energy model with recent cosmological observations of the CMB anisotropies and background distance measure data sets. We found that for an IDE model with a constant fifth-force, cosmological data constrains the strength of this fifth-force to be $< 1\%$ the strength of gravity. This rather unappealing fact leads to the question, are there any other forms of coupling that are well-motivated and do *not* lead to such strong constraints on the fifth-force? It is in this chapter that we introduce and explore such a coupling.

In section 5.1 we introduce the interacting dark energy model and new form of coupling, and explore some of its imprints at the background and perturbation level. We then confront this IDE model with cosmological data as done in chapter 4, describing the methodology and the data sets used in section 5.2, presenting our results in section 5.3, and finally concluding in section 5.4.

5.1 Interacting dark energy model

The IDE model considered in this chapter is based on the general IDE model introduced in chapter 3, where we recall that as a result of the dark sector interaction, the DM particles experience an effective gravitational constant given

by

$$G_{\text{eff}} = G\left(1 + 2\beta^2\right), \tag{5.1}$$

where G is the Newtonian gravitational constant and β is the coupling such that

$$\beta = \frac{M_{\text{Pl}}}{2}\frac{\mathrm{d}\ln C}{\mathrm{d}\phi}. \tag{5.2}$$

Whilst the exponential form for the conformal coupling function $C(\phi)$ is well-motivated and arises naturally in many fundamental theories of physics [197, 198, 199], we saw in chapter 4 that the strength of the fifth-force in the dark sector is constrained to be $< 1\%$ the strength of gravity when using a combination of cosmological data sets, making this particular form of coupling unappealing. This leads us to consider new forms of couplings, where the fifth-force is no longer constant throughout cosmic history.

In 1994, work by Thibault Damour and Alexander Polyakov [235, 236] suggested that coupling functions in string theory could possess minima, and this idea was further elaborated upon in [237] in the construction of a dark energy model. Applying these concepts to the IDE model introduced in chapter 3, let us consider a new class of couplings where the conformal coupling function $C(\phi)$ possesses a minimum at some finite field value ϕ_*.

In the search for a coupling function with a minimum, let us consider a natural extension to the exponential coupling by considering the sum of two exponentials, such is done, for example, with extensions to the scalar field exponential potential [238]. By requiring this coupling to have a minimum, this sum of exponentials reduces in a simple case to the hyperbolic cosine function such that

$$\begin{aligned} C(\phi) &= \frac{1}{2}\left(e^{\alpha(\phi-\phi_*)/M_{\text{Pl}}} + e^{-\alpha(\phi-\phi_*)/M_{\text{Pl}}}\right) \\ &= \cosh\Big(\alpha(\phi-\phi_*)/M_{\text{Pl}}\Big)\,, \end{aligned} \tag{5.3}$$

where ϕ_* is the minimum of the coupling function $C(\phi)$ and α is the conformal coupling constant. Note that the conformal coupling function $C(\phi)$ in eq. (5.3)

is symmetric under a sign change in α, so we only consider $\alpha > 0$ without loss of generality. If the field sits at the minimum of the coupling function, $\phi = \phi_*$, then the coupling β between DM and DE vanishes. However, if the field then grows $\phi > \phi_*$, then the coupling β (eq. (5.2)), which for this model is

$$\beta = \frac{\alpha}{2} \tanh\Big(\alpha(\phi - \phi_*)/M_{\rm Pl}\Big), \tag{5.4}$$

increases with ϕ such that energy flows DE $\rightarrow$ DM. This growth in the coupling β results in an effective gravitational constant $G_{\rm eff}$ (eq. (5.1)) that grows with the field value, where we note that the strength of the fifth-force depends on the magnitude of the coupling constant α *and* the distance between the field and the minimum ϕ_*. We will see that this effect of the strength of the fifth-force being determined by the evolution of the scalar field has interesting implications for cosmology.

5.1.1 General imprints on background and perturbation level cosmology

We consider an IDE model where the conformal coupling function has a minimum and the scalar field potential is of exponential form. To be concrete, this model is specified by

$$C(\phi) = \cosh\Big(\alpha(\phi - \phi_*)/M_{\rm Pl}\Big)\ , \quad V(\phi) = V_0^4 e^{-\lambda\phi/M_{\rm Pl}}\ , \tag{5.5}$$

where $\alpha > 0$ is the conformal coupling constant, $\lambda > 0$ is the slope of the scalar field potential, V_0 is the mass scale of the potential, and ϕ_* is the minimum of the coupling function which is set to $\phi_* = 1 M_{\rm Pl}$ without loss of generality. Note that in this model, the initial value of the scalar field, $\phi_{\rm ini}$, does play a role, therefore this IDE model introduces three new scalar field parameters, the coupling constant α, slope of the potential λ, and initial field value $\phi_{\rm ini}$.

Let us now briefly look at some of the background and perturbation level dynamics of this model. As in chapter 3, we use a modified version of the `CLASS` [61] Boltzmann code and use cosmological parameter values from the 2018 *Planck*

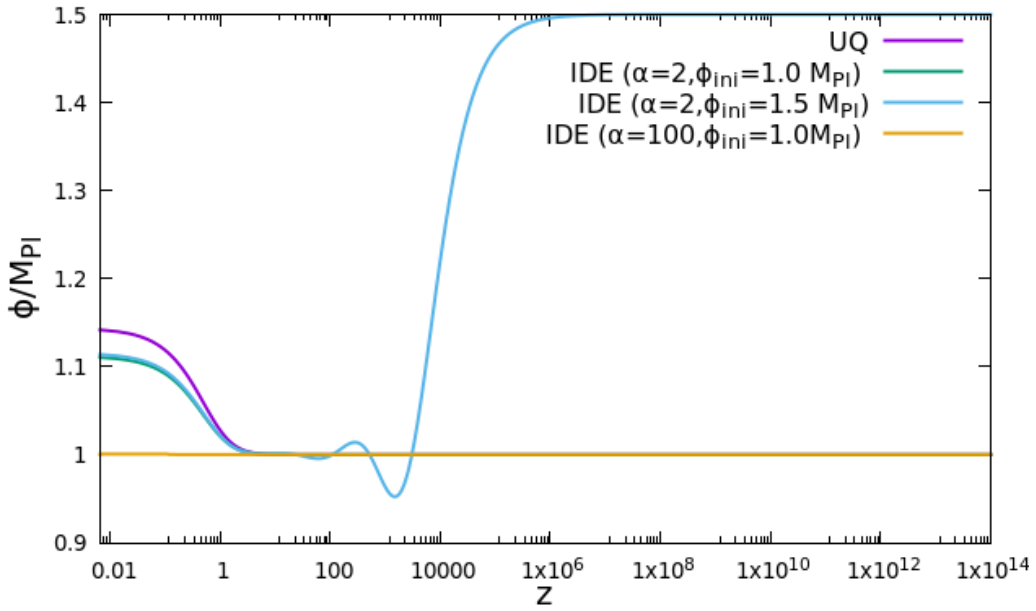

Figure 5.1: Evolution of the scalar field in units $M_{\rm Pl}$ for the UQ, IDE($\alpha = 2, \phi_{\rm ini} = 1.0M_{\rm Pl}$),IDE($\alpha = 2, \phi_{\rm ini} = 1.5M_{\rm Pl}$), and IDE($\alpha = 100, \phi_{\rm ini} = 1.0M_{\rm Pl}$) models. The slope of the scalar field potential is set to $\lambda = 0.5$ in all the models.

[50] bestfit results for the baseline model where appropriate in order to obtain the numerical results for the plots and tables in this subsection. To be concrete, these are the present-day reduced baryon density parameter $\Omega_b h^2 = 0.02236$, the present-day reduced cold dark matter density parameter $\Omega_{\rm cdm} h^2 = 0.1202$, the angular size of the sound horizon at decoupling $100\theta_s = 1.04090$, the amplitude of the primordial curvature power spectrum $\ln(10^{10} A_s) = 3.045$, the spectral index of the primordial curvature power spectrum $n_s = 0.9649$, and the optical depth at reionisation $\tau_{\rm reio} = 0.0544$, where h is the reduced Hubble constant defined by $H_0 = 100h\ {\rm kms}^{-1}{\rm Mpc}^{-1}$ and where the cosmological parameters are as defined in section 1.2.3. In this subsection, the uncoupled quintessence (UQ) model we consider possesses an exponential potential, and the IDE model we consider is as defined in eq. (5.5), where the coupling has a minimum and the potential is of exponential form.

The first thing to notice is that this model only differs from an uncoupled quintessence (UQ) model when $\phi \neq \phi_*$, therefore making the cosmological evolu-

tion of the scalar field a determining factor in this model. In Figure 5.1 we plot the evolution of the scalar field for the UQ model and three IDE models which are specified by their choice for conformal coupling constant α and initial field value $\phi_{\rm ini}$, where the slope of the potential is the same in all models, $\lambda = 0.5$. In the IDE($\alpha = 2, \phi_{\rm ini} = 1.0 M_{\rm Pl}$) model, we see that this model behaves similarly to the UQ model in its evolution of ϕ. In both models, the field is frozen at the minimum by Hubble friction, but then at late-times, when the potential becomes dynamically important, the field begins to roll. One difference that the coupling makes, however, is that when the field switches on at $z \sim 1$, the field does not evolve as far as in the UQ model. This is because the coupling term in the modified Klein-Gordon equation also grows, and thus slows down the evolution of ϕ. In the extreme case of the IDE($\alpha = 100, \phi_{\rm ini} = 1.0 M_{\rm Pl}$) model, we see that the late-time growth in ϕ is heavily suppressed due to a stronger coupling, growing only by $\sim 10^{-4} M_{\rm Pl}$ compared to the $\sim 10^{-1} M_{\rm Pl}$ growth in the IDE($\alpha = 2, \phi_{\rm ini} = 1.0 M_{\rm Pl}$) and UQ models.

In the IDE($\alpha = 2, \phi_{\rm ini} = 1.5 M_{\rm Pl}$) model where the field does not initially sit at the minimum, we see that it is initially frozen at $\phi = 1.5 M_{\rm Pl}$ but then is driven towards the minimum by the coupling term in the Klein-Gordon equation when the matter density becomes dynamically important. After the field has finally settled at $z \sim 100$, its evolution is very similar to the IDE($\alpha = 2, \phi_{\rm ini} = 1.0 M_{\rm Pl}$) model. So we see that the IDE($\phi_{\rm ini} = \phi_*$) models do not differ too drastically from the uncoupled quintessence model, except at late-times and depending on the magnitude of the coupling constant α. However, if the field does not initially sit at the minimum, the evolution history of the scalar field is quite different compared to the UQ and IDE($\phi_{\rm ini} = \phi_*$) models.

We mentioned that a particularly intriguing feature of this IDE model is that the dark sector coupling can be switched on and off depending on whether or not the scalar field sits at the minimum of the coupling. In Figure 5.2 we plot the evolution of the ratio of the effective gravitational constant to the Newtonian gravitational constant for the UQ and three IDE models that appear in Figure 5.1. We see in this figure that for the IDE($\alpha = 2, \phi_{\rm ini} = 1.5 M_{\rm Pl}$) model where the field

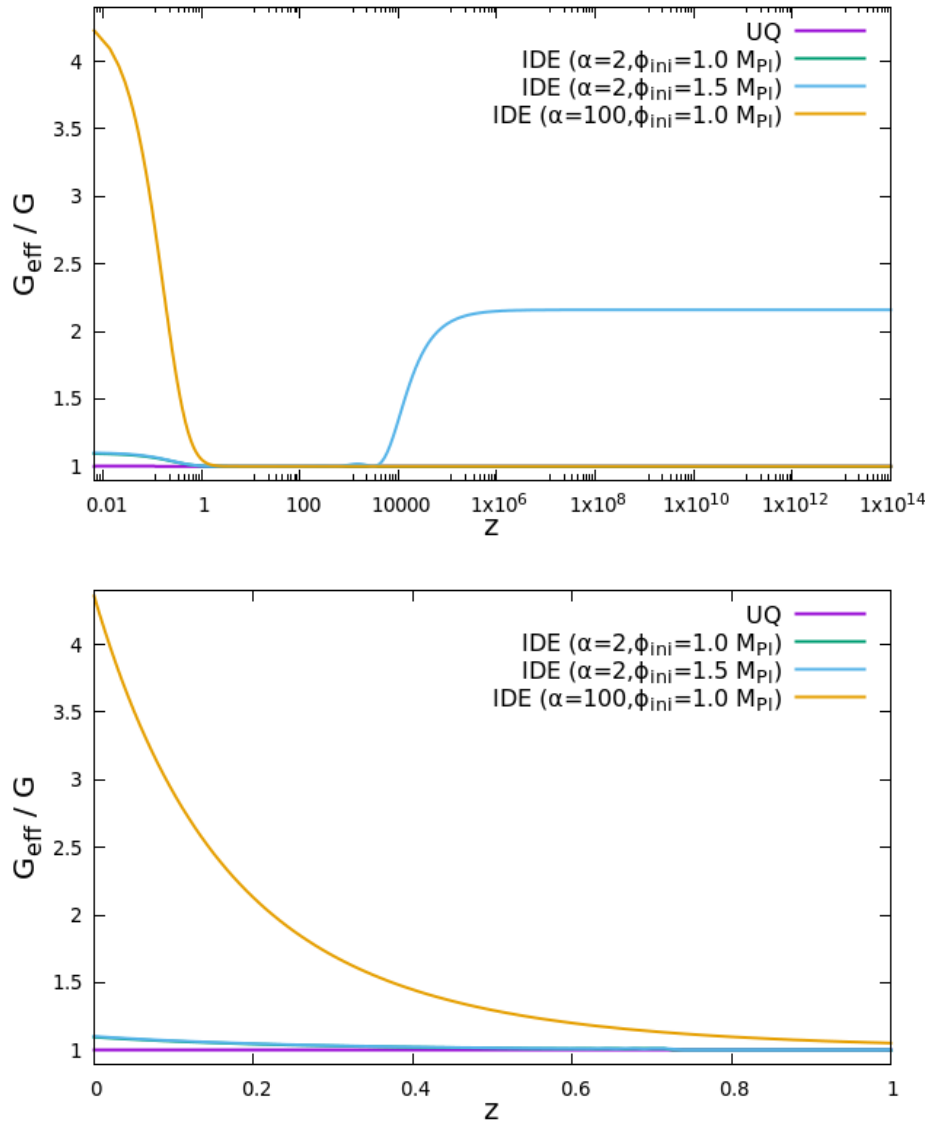

Figure 5.2: Evolution of the ratio of the effective gravitational constant $G_{\rm eff}$ (eq. (4.4)) to the Newtonian gravitational constant G for the UQ and IDE models. In the upper panel we plot in the redshift range $z \in (0, 10^{14})$ and in the lower panel we plot in the redshift range $z \in (0, 2)$. The slope of the scalar field potential is set to $\lambda = 0.5$ in all the models.

does not initially sit at the minimum, the DM particles initially experience a constant fifth-force approximately the strength of gravity. Then, as the field is driven towards the minimum ϕ_* due to the matter density becoming important,

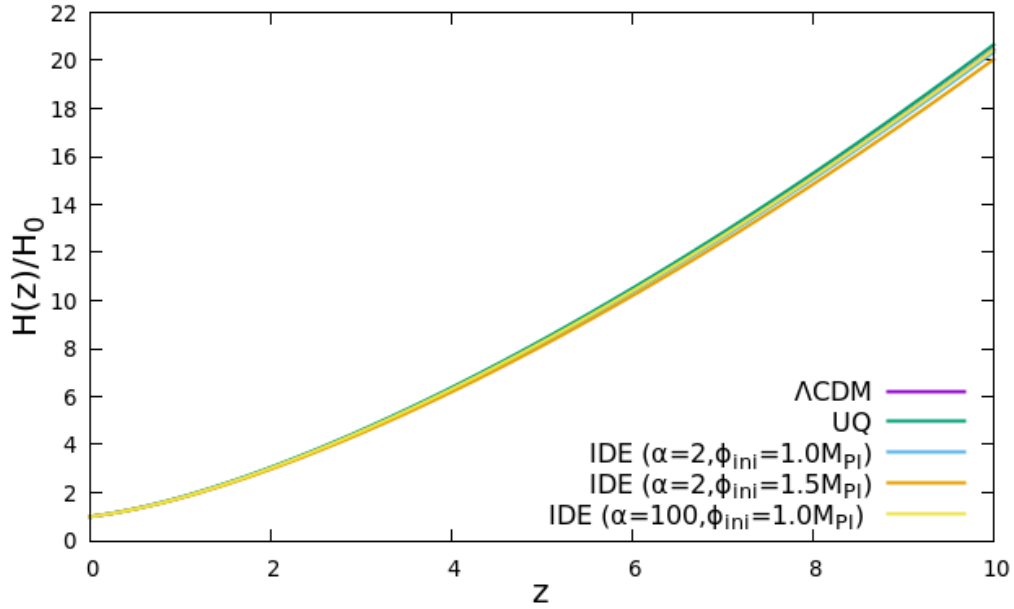

Figure 5.3: The evolution of the Hubble parameter $H(z)$ normalised by its present-day value H_0 for the ΛCDM, UQ, and IDE models. The slope of the scalar field potential is set to $\lambda = 0.5$ in the UQ and IDE models.

the fifth-force disappears. Only at late-times, when the scalar field potential becomes dynamically important at $z \sim 1$, does this fifth-force reemerge, giving a present-day strength $\sim 10\%$ the strength of gravity. In Figure 5.2 we also plot the evolution of the effective gravitational constant for the more extreme IDE($\alpha = 100, \phi_{\rm ini} = 1.0 M_{\rm Pl}$) model. In this model, the field initially sits at the minimum and is frozen there, however, when the field switches on at late-times, a fifth-force in the dark sector emerges with a present-day strength over three times the strength of gravity.

Let us now look at some of the effects this interacting dark energy model has on the evolution history $H(z)$. In Figure 5.3 we plot the evolution of the Hubble parameter $H(z)$ normalised by its present-day value H_0 for the ΛCDM, UQ, and IDE models. In the IDE models where the field initially sits at the minimum, the models are indistinguishable from the uncoupled quintessence model until late-times. Since the fifth-force in these models has only had a short time, cosmologically speaking, to act, they do not differ too drastically in their late-time

evolution of $H(z)$ when compared to the UQ model.

Recall that the mass of a DM particle m_{DM} becomes field-dependent as a result of the coupling with the DE scalar field and scales like $m_{DM}(\phi) \propto \sqrt{C(\phi)}$. We find that in the IDE($\alpha = 2, \phi_{\rm ini} = 1.0 M_{\rm Pl}$) model the mass increases by $\sim 1.25\%$ and in the more extreme IDE($\alpha = 100, \phi_{\rm ini} = 1.0 M_{\rm Pl}$) model, the mass actually increases less by $\sim 0.02\%$ as a result of the motion of the scalar field being slowed down. Comparing this to a constant fifth-force model, such as those with an exponential coupling and exponential potential seen in chapter 3, we find that the masses of DM particles in these models change by $\sim 25\%$ despite only increasing $G_{\rm eff,0}$ by $\sim 5\%$, when the slope of the potential is $\lambda = 0.5$ and the conformal coupling constant is $|\alpha| = 0.15$.

Therefore, in the IDE models where the field initially sits at the minimum, we do not expect the evolution of the energy densities to differ too greatly from the UQ model and hence the evolution of $H(z)$ is quite similar in these models. In the IDE($\alpha = 2, \phi_{\rm ini} = 1.5 M_{\rm Pl}$) model, we can see in Figure 5.3 that this model has the greatest deviation from ΛCDM. The mass of DM particles in this model differ from the uncoupled case at early times, and therefore the evolution history of the DM energy density is altered in a distinct way, thus affecting the evolution history of this model more significantly than in the IDE($\phi_{\rm ini} = \phi_*$) models. We can expect, therefore, that background data, such as from BAO [227] and SNIa [232] distance measurements, may not be so effective in constraining the coupling parameter α when compared to the initial field value $\phi_{\rm ini}$.

As we saw in chapter 3, the coupling between DE and DM results in the DM energy density scaling differently to baryons which, if not accounted for, results in an effective DE fluid whose energy density ρ_{DE} absorbs the part of the DM fluid which does not scale like baryons. The equation of state for the effective DE fluid is (eq. (3.54))

$$\begin{aligned} w_{DE} &= \frac{p_\phi}{\rho_{DE}} \\ &= \frac{p_\phi}{\rho_\phi + \rho_c - \rho_{c,0} a^{-3}}, \end{aligned} \tag{5.6}$$

where p_ϕ is the pressure of the scalar field, ρ_ϕ is the energy density of the scalar

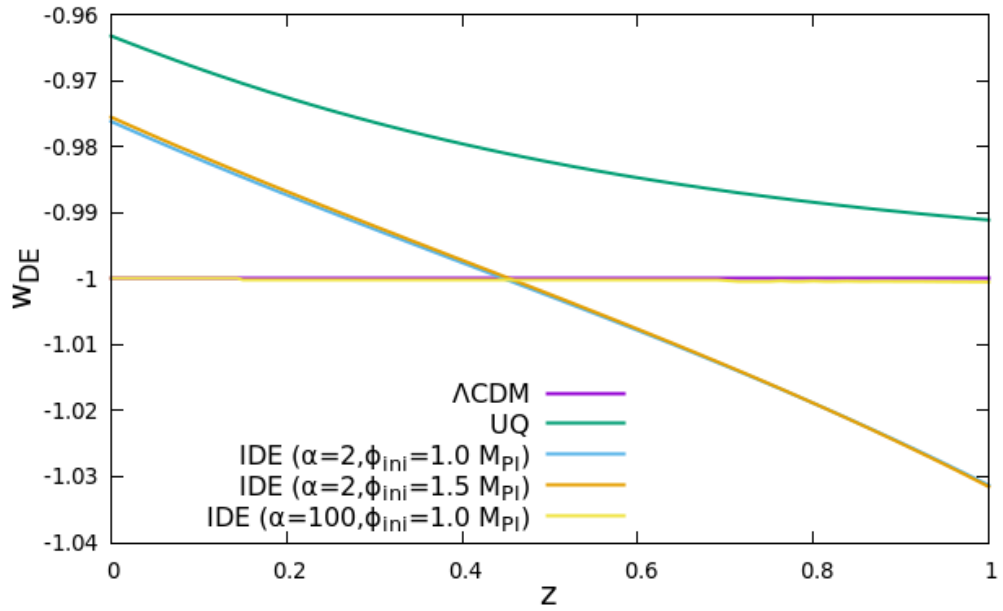

Figure 5.4: The evolution of the effective DE equation of state parameter $w_{DE}(z)$ for the ΛCDM, UQ, and IDE models, where we define $w_{DE} := -1$ for the ΛCDM model. Note that the effective DE equation of state, w_{DE}, for the IDE($\alpha = 2, \phi_{\rm ini} = 1.0 M_{\rm Pl}$) and IDE($\alpha = 2, \phi_{\rm ini} = 1.5 M_{\rm Pl}$) models crosses the phantom line $w = -1$. The slope of the scalar field potential is set to $\lambda = 0.5$ in the UQ and IDE models.

field, and ρ_c is the energy density of the coupled DM fluid. If the coupled DM fluid dilutes slower than baryons, then this can result in an equation of state for the effective DE fluid that crosses the phantom line $w = -1$. In Figure 5.4 we plot the evolution of the effective DE equation of state parameter $w_{DE}(z)$ for the ΛCDM, UQ, and IDE models. We see for the more extreme IDE($\alpha = 100, \phi_{\rm ini} = 1.0 M_{\rm Pl}$) model, the late-time evolution of the field ϕ is inhibited so strongly that its effective equation of state is very close to that of the cosmological constant, $w_\Lambda = -1$. For the less extreme IDE models, we see that they both cross the phantom line at $z \sim 0.5$, with the IDE($\alpha = 2, \phi_{\rm ini} = 1.0 M_{\rm Pl}$) and IDE($\alpha = 2, \phi_{\rm ini} = 1.5 M_{\rm Pl}$) models being largely indistinguishable.

Now let us look at some perturbation level imprints of this IDE model. In Figure 5.5 we plot the CMB temperature anisotropy power spectrum for the ΛCDM, UQ, and IDE models. We see here that all the models agree to within

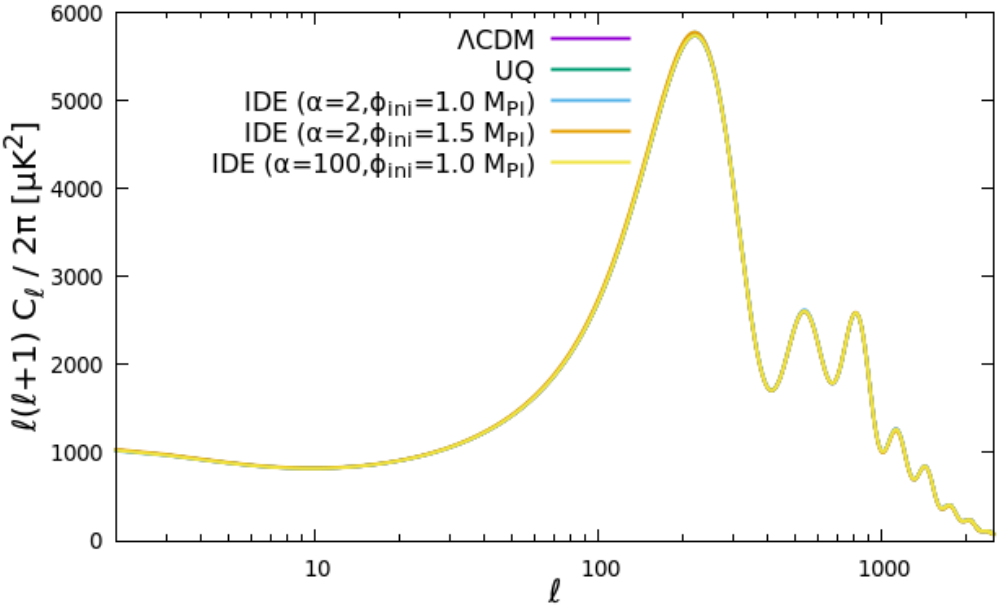

Figure 5.5: The CMB temperature anisotropy power spectrum for the ΛCDM, UQ, and IDE models where C_ℓ is the power spectrum of the anisotropies in units μK^2 and ℓ is the multipole moment [3]. The slope of the scalar field potential is set to $\lambda = 0.5$ in the UQ and IDE models.

a reasonable degree in their predictions of the power spectrum. The IDE models where the field initially sits at the minimum differ less from the UQ model than the IDE($\phi_{\rm ini} \neq \phi_*$) model. Since the IDE($\phi_{\rm ini} = \phi_*$) models only begin to differ from the UQ model at $z \sim 1$, we do not expect these models to predict a CMB anisotropy power spectrum significantly different from the UQ model. The IDE($\alpha = 2, \phi_{\rm ini} = 1.5 M_{\rm Pl}$) model deviates the most from the UQ model and therefore whilst we expect that CMB data alone will not be too effective in constraining the IDE model, it should constrain $\phi_{\rm ini}$ more effectively than the coupling parameter α.

Finally, let us look at the matter power spectrum to see what effect the IDE model has on the large-scale structure (LSS) in the universe. We see that for the IDE($\phi_{\rm ini} = \phi_*$) models, increasing the coupling constant α has the effect of increasing the power at small to intermediate scales owing to an increase in the effective gravitational constant experienced between DM particles. For the IDE($\alpha = 2, \phi_{\rm ini} = 1.5 M_{\rm Pl}$) model, the early-time enhancement of the effective

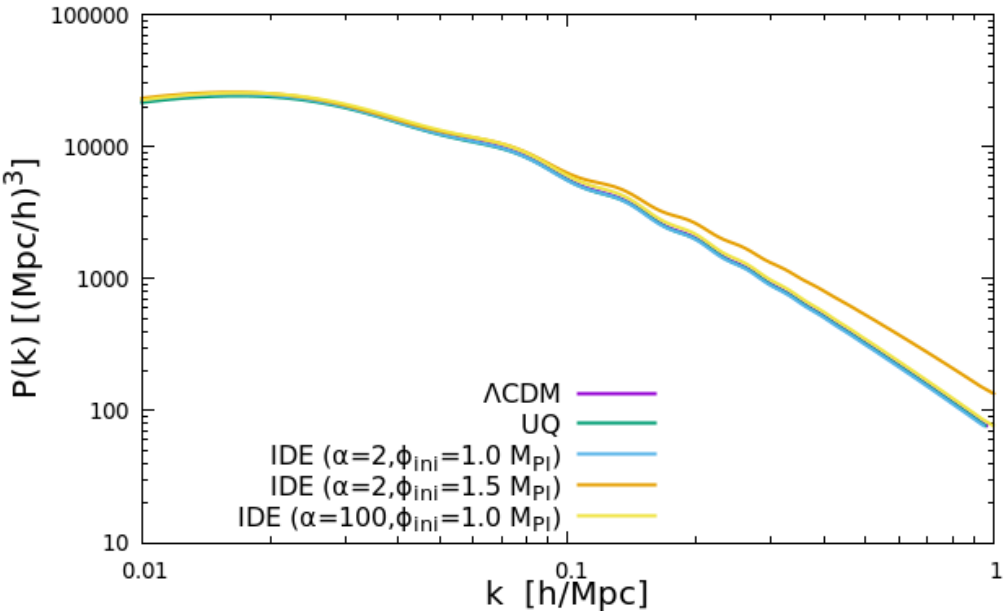

Figure 5.6: The present-day matter power spectrum for the ΛCDM, UQ, and IDE models where $P(k)$ is the matter power spectrum in units $(\mathrm{Mpc}/h)^3$ and k is the wavenumber in units h/Mpc with h being the dimensionless Hubble parameter defined in eq. (1.50). The slope of the scalar field potential is set to $\lambda = 0.5$ in the UQ and IDE models.

gravitational constant results in a more pronounced increase in power at small to intermediate scales.

A useful measure of the present-day amplitude of structure is the σ_8 parameter introduced in chapter 2. We saw in chapter 3 that the coupled quintessence models with a constant fifth-force had a larger σ_8 parameter associated with them compared to the uncoupled model, owing to the constant enhancement of G_{eff}. In Table 5.1, we report the derived values of σ_8 for the ΛCDM, UQ, and IDE models, as well as the percentage enhancement of the present-day effective gravitational constant with respect to the Newtonian gravitational constant. We see in this table that for the IDE($\phi_{\mathrm{ini}} = \phi_*$) models, increasing the coupling parameter α has the effect of increasing the amplitude of structure, as signified by the increase in σ_8. In the IDE($\alpha = 2, \phi_{\mathrm{ini}} = 1.5 M_{\mathrm{Pl}}$) model where the field does not initially sit at the minimum, we see that despite the present-day effective gravitational constant being comparable to the IDE($\alpha = 2, \phi_{\mathrm{ini}} = 1.0 M_{\mathrm{Pl}}$) model,

Model	ΔG %	σ_8
ΛCDM	0	0.824
UQ	0	0.818
IDE $(\alpha = 2, \phi_{\rm ini} = 1.0 M_{\rm Pl})$	9.7	0.815
IDE $(\alpha = 2, \phi_{\rm ini} = 1.5 M_{\rm Pl})$	10	0.926
IDE $(\alpha = 100, \phi_{\rm ini} = 1.0 M_{\rm Pl})$	340	0.852

Table 5.1: The values of ΔG and σ_8 (eq. (2.10)) for the ΛCDM, UQ, and IDE models where $\Delta G := (G_{\rm eff,0}/G) - 1$ describes the enhancement of the present-day effective gravitational constant compared to the Newtonian gravitational constant. The slope of the scalar field potential is set to $\lambda = 0.5$ in the UQ and IDE models.

the σ_8 parameter is significantly increased. This is owing to the enhancement of the effective gravitational constant $G_{\rm eff}$ at early times in the radiation-dominated epoch as depicted in the upper panel of Figure 5.2. Owing to these effects, we expect that LSS data, such as from cosmic shear [72, 73, 74] and galaxy cluster [226] measurements, which provides information on the growth and amplitude of structure may be effective in constraining the IDE model.

Now that we have established that this IDE model has a distinct effect on background and perturbation level dynamics, let us seek to constrain the model using cosmological observations, such as from CMB, BAO, SNIa, and LSS experiments, to see what bounds nature puts on the model.

5.2 Methodology and observational data

In order to numerically study the evolution of the background and cosmological perturbations for the IDE model, which will be called **M3** (eq. (5.5)) from now on, we use a modified version of the `CLASS` code [61] as seen in chapter 3. We confront the IDE model with data through cosmological parameter exploration using the Markov Chain Monte Carlo (MCMC) sampling package `MontePython` [220, 221], interfaced with `CLASS`, in conjunction with the observational data sets outlined below. In addition to this, the `GetDist` [222] Python package is used to analyse the MCMC chains and produce the values and plots of the parameter constraints in section 5.3. Finally, in order to statistically compare the different cosmological models and determine which model has the greatest support for it in light of data, we calculate the Bayes factor of an IDE model relative to the ΛCDM model by using the `MCEvidence` code [223]. For more details on the Bayes factor and its interpretation, we refer to chapter 4.

In our analysis, M3 is described by a set of nine parameters. The six ΛCDM parameters are the reduced baryon energy density $\Omega_b h^2$, the reduced CDM energy density $\Omega_{cdm} h^2$, the ratio of the sound horizon to the angular diameter distance at decoupling θ_s, the scalar amplitude of the primordial power spectrum A_s, the scalar spectral index n_s, and the reionisation optical depth τ_{reio}, where h is the reduced Hubble constant defined by $H_0 = 100h\text{kms}^{-1}\text{Mpc}^{-1}$. The M3 model introduces the conformal coupling parameter α, the slope of the scalar field potential λ, and the initial value of the scalar field ϕ_{ini}. The flat priors for the ΛCDM and M3 model parameters are shown in Table 5.2. We also report constraints on several important derived parameters in section 5.3. The derived parameters of interest are the Hubble constant H_0, the present-day mass fluctuation amplitude in spheres of radius $8h^{-1}\text{Mpc}$ σ_8, and the total matter density parameter Ω_m.

We use the PL18, BAO, and Pantheon data sets described in chapter 4 alongside the following data set in order to analyse and constrain the models in question:

- **Redshift Space Distortions:**

Parameter	Prior (ΛCDM)	Prior (M3)
$\Omega_b h^2$	$[0.005, 0.1]$	$[0.005, 0.1]$
$\Omega_{cdm} h^2$	$[0.001, 0.99]$	$[0.001, 0.99]$
$100\theta_s$	$[0.5, 10]$	$[0.5, 10]$
$\tau_{\rm reio}$	$[0.01, 0.8]$	$[0.01, 0.8]$
n_s	$[0.7, 1.3]$	$[0.7, 1.3]$
$\ln(10^{10} A_s)$	$[1.7, 5.0]$	$[1.7, 5.0]$
α	–	$[0, 500]$
λ	–	$[0, 5]$
$\phi_{\rm ini}/M_{\rm Pl}$	–	$[0, 2]$

Table 5.2: Flat priors for the cosmological parameters sampled in our analysis in the ΛCDM and M3 models.

If the spatial distributions of galaxies are plotted in redshift-space, the galaxies appear distorted due to the peculiar velocities of the galaxies along the line of sight [239]. Measurements of the peculiar velocities of galaxies allow for an inference of the growth of large-scale structure [240] and hence galaxy redshift surveys such as the Sloan Digital Sky Survey peculiar velocity (SDSS PV) survey [241] and the the 6-degree Field Galaxy Survey velocity sample (6dFGSv) [242] survey, can be used to obtain measurements on the product of the linear growth rate $f(a) = \mathrm{d}\ln D/\mathrm{d}\ln a$ where $D(a)$ is the linear growth factor [243] and the root-mean-square matter fluctuation in a sphere of radius $8h^{-1}$Mpc at a given redshift, $\sigma_8(z)$. Since predictions of the growth history of the universe depend on the cosmological model assumed, measurements of $f\sigma_8(z)$ at various redshifts allow for cosmological models to be constrained [240]. We employ the 'Gold 2018' Redshift Space Distortions (RSD) data set compilation consisting of 22 measurements as

described in [244] and a likelihood code as detailed in [244, 245]. We denote this dataset as **RSD** in this chapter.

5.3 Results

The results of our data analysis are shown in Tables 5.3 and 5.4 where we report the parameter constraints for the M3 and ΛCDM models using the PL18+BAO +Pantheon and PL18+BAO+Pantheon+RSD data set combinations for each model. The runs involving the PL18, PL18+BAO and PL18+Pantheon data set combinations did not converge for the M3 model and therefore we exclude them in our analysis. In Figure 5.8 we display 2D marginalised posterior distributions for the conformal coupling parameter, α, against the slope of the potential, λ, the initial field value, $\phi_{\rm ini}$, and the present-day mass fluctuation amplitude in spheres of radius $8h^{-1}$Mpc, σ_8 in the M3 model. In Figure 5.9 we plot the 2D marginalised posterior distribution of the σ_8 parameter against the slope of the potential λ in the M3 model. Furthermore, in Figure 5.7 we plot the 1D marginalised posterior distributions for the conformal coupling parameter α, the slope of the potential λ, and the initial field value $\phi_{\rm ini}$ in the M3 model. Finally, in Table 5.5 we report the derived σ_8 value and percentage enhancement of the present-day effective gravitational constant for the M3 model using the 68% confidence limits of the conformal coupling parameter α and slope of the potential λ from runs using the PL18+BAO+Pantheon and PL18+BAO+Pantheon+RSD data set combinations. We run the MCMC chains until they have converged, with all parameters achieving a Gelman-Rubin statistic [233] of $|R-1|<0.03$, where R is the Gelman-Rubin statistic.

We begin by observing that the ΛCDM model is excellently constrained by the PL18+BAO+Pantheon data set, with the six ΛCDM parameters and derived parameters, apart from $\tau_{\rm reio}$, being constrained to within a few percent precision as can be seen in Table 5.4. The addition of the RSD growth rate data set does not appear have a significant effect on the parameter constraints.

Turning our attention to the IDE model M3, we see in Table 5.3 that both

Parameter	PL18+BAO+Pantheon	PL18+BAO+Pantheon +RSD
$\Omega_b h^2$	0.02246 ± 0.00014	0.02248 ± 0.00014
$\Omega_{cdm} h^2$	$0.1210^{+0.0010}_{-0.0027}$	0.11875 ± 0.00095
$100\theta_s$	1.04195 ± 0.00029	1.04198 ± 0.00029
τ_{reio}	$0.0560^{+0.0071}_{-0.0080}$	0.0541 ± 0.0077
n_s	0.9682 ± 0.0038	0.9688 ± 0.0038
$\ln(10^{10} A_s)$	3.046 ± 0.016	$3.041^{+0.015}_{-0.017}$
λ	< 1.07	< 0.189
α	< 22.5	< 29.1
$\phi_{\rm ini}/M_{\rm Pl}$	$1.016^{+0.052}_{-0.084}$	$1.015^{+0.073}_{-0.11}$
H_0	67.73 ± 0.50	67.95 ± 0.45
σ_8	$0.904^{+0.055}_{-0.11}$	$0.8080^{+0.0080}_{-0.0091}$
Ω_m	$0.3142^{+0.0067}_{-0.0093}$	0.3074 ± 0.0056
$\ln B_{i,\Lambda\rm CDM}$	-6.05	-8.32

Table 5.3: Observational constraints at a 68% confidence level on the independent and derived cosmological parameters for the M3 model using the PL18+BAO+Pantheon and PL18+BAO+Pantheon+RSD data set combinations. The quantities in the second half of this table are the derived parameters of our analysis which are the Hubble constant H_0 in units $\mathrm{km\,s^{-1}\,Mpc^{-1}}$, the present-day mass fluctuation amplitude in spheres of radius $8h^{-1}$Mpc σ_8, and the total matter density parameter Ω_m. In the last row, we report the natural logarithm of the Bayes factor with respect to the ΛCDM model, $\ln B_{i,\Lambda\rm CDM}$, as defined by eq. (4.3).

the PL18+BAO+Pantheon and PL18+BAO+Pantheon+RSD data set combinations are consistent with a null-coupling at 1σ. Interestingly, rather than constraining the coupling parameter closer to zero, the addition of the RSD data set actually pushes the 1σ confidence limit up from $\alpha < 22.5$, derived from the

Parameter	PL18+BAO+Pantheon	PL18+BAO+Pantheon +RSD
$\Omega_b h^2$	0.02243 ± 0.00013	0.02247 ± 0.00013
$\Omega_{cdm} h^2$	0.11923 ± 0.00097	0.11872 ± 0.00095
$100\theta_s$	1.04196 ± 0.00028	1.04200 ± 0.00029
τ_{reio}	0.0560 ± 0.0079	0.0543 ± 0.0078
n_s	0.9676 ± 0.0037	0.9686 ± 0.0037
$\ln(10^{10} A_s)$	3.047 ± 0.017	3.041 ± 0.016
H_0	67.75 ± 0.43	67.98 ± 0.42
σ_8	0.8093 ± 0.0073	0.8057 ± 0.0069
Ω_m	0.3101 ± 0.0058	0.3070 ± 0.0056

Table 5.4: Observational constraints at a 68% confidence level on the independent and derived cosmological parameters for the ΛCDM model using the PL18+BAO+Pantheon and PL18+BAO+Pantheon+RSD data set combinations. The quantities in the second half of this table are the derived parameters of our analysis which are the Hubble constant H_0 in units $\mathrm{km\,s^{-1}\,Mpc^{-1}}$, the present-day mass fluctuation amplitude in spheres of radius $8h^{-1}$Mpc σ_8, and the total matter density parameter Ω_m.

PL18+BAO+Pantheon data set, to $\alpha < 29.1$. In Figure 5.7 we plot the 1D posterior distributions for the conformal coupling parameter α, the slope of the potential λ, and the initial field value $\phi_{\rm ini}$ using the PL18+BAO+Pantheon and PL18+BAO+Pantheon+RSD data set combinations. We see in Figure 5.7 that whilst the distribution profile for α is quite similar in both the PL18+BAO +Pantheon and PL18+BAO+Pantheon+RSD runs, the behaviour at large values of α is quite different. When using the PL18+BAO+Pantheon data set combination, the probability density of α tapers off to zero at $\alpha \sim 100$, however, when using the PL18+BAO+Pantheon+ RSD data set combination, we see that although the density does decrease as α increases, it then asymptotes to a non-zero prob-

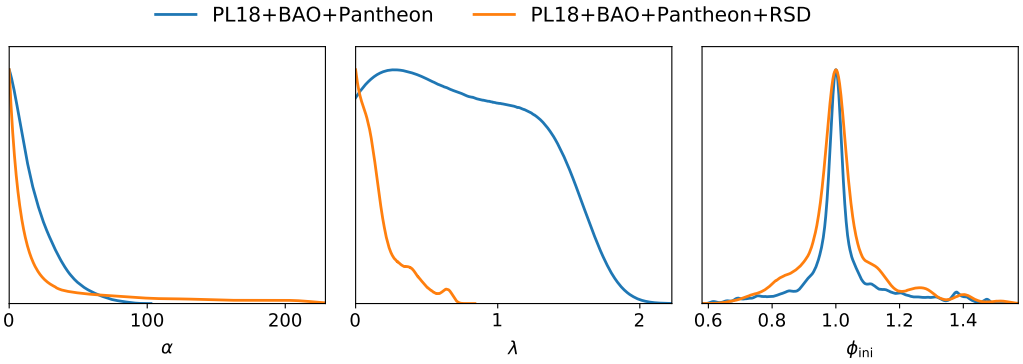

Figure 5.7: 1D marginalised posterior distributions of the coupling parameter, α, slope of the potential, λ, and initial field value in units $M_{\rm Pl}$, $\phi_{\rm ini}$, in the M3 model using the PL18+BAO+Pantheon and PL18+BAO+Pantheon+RSD data set combinations. The distributions here are scaled such that their maximum value is equal to unity in order to aid comparison.

ability density, before finally converging to zero at $\alpha \gtrsim 200$. This long tail in the distribution of α results in the 1σ confidence limit being pushed to greater values when using the PL18+BAO+Pantheon+RSD data set combination compared to the PL18+BAO+Pantheon data set combination.

We see in Table 5.3, where we report the parameter constraints for model M3, that whilst data from the CMB anisotropies and background measurements allow for a fairly large slope of the potential, $\lambda < 1.07$ at 1σ, the addition of the RSD data set heavily constrains the slope to $\lambda < 0.189$ at 1σ. In Figure 5.7, where we plot the 1D posterior distributions of the scalar field parameters, we can see the powerful constraining effect the additional RSD data set has on the distribution of the slope of the potential λ. Whilst the distribution profile for λ when using PL18+BAO+Pantheon data set appears to be fairly flat and then cuts off quickly to zero at $\lambda \sim 1.5$, the profile for λ when using the additional RSD data set decreases quite sharply to zero as λ increases. We will see why the slope of the potential, λ, is so heavily constrained by the inclusion of RSD data shortly when we explore the 2D distribution profiles and correlations between parameters, but before we do, let us look to the final scalar field parameter, the initial field value $\phi_{\rm ini}$.

In Table 5.3 we see that the inclusion of RSD data does not have a significant

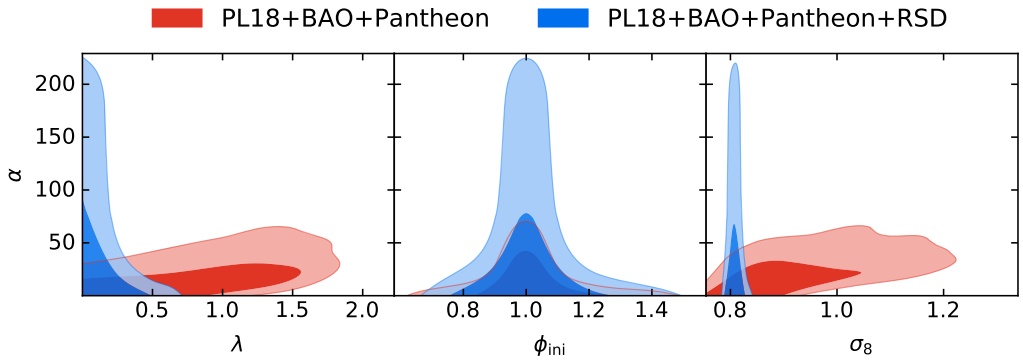

Figure 5.8: 2D marginalised posterior distributions of parameters in the M3 model using the PL18+BAO+Pantheon and PL18+BAO +Pantheon +RSD data set combinations. We plot the 2D marginalised posterior distributions of the conformal coupling parameter, α, against the slope of the potential, λ, the initial field value in units $M_{\rm Pl}$, $\phi_{\rm ini}$, and the present-day mass fluctuation amplitude in spheres of radius $8h^{-1}$Mpc, σ_8. The shaded contours indicate the 1σ and 2σ confidence limits.

effect on the constraints on the initial field value $\phi_{\rm ini}$. Constraints from the PL18+BAO+Pantheon data set give a mean value of $\phi_{\rm ini}/M_{\rm Pl} = 1.016^{+0.052}_{-0.084}$ at 1σ and constraints from the PL18+BAO+Pantheon+RSD data set give a mean value of $\phi_{\rm ini}/M_{\rm Pl} = 1.015^{+0.073}_{-0.11}$ at 1σ. We see then that the mean value of $\phi_{\rm ini}$ is not significantly changed and that $\phi_{\rm ini}$ is tightly constrained about the minimum of the conformal coupling function, in agreement with results found in [2]. This suggests that the imprints from the IDE model when the field does not initially sit at the minimum are significant enough at the background level and in the CMB anisotropy power spectrum to effectively constrain this parameter. We see how in Figure 5.7 the distribution of the initial field value, $\phi_{\rm ini}$, sharply peaks at the minimum $\phi_* = 1M_{\rm Pl}$ and then quickly drops off on either side of ϕ_*, for both of the data set combinations. It may appear then that this IDE model requires fine-tuning of the initial field value at $a_{\rm ini} \sim 10^{-14}$ to be very close to the minimum of the coupling function $C(\phi)$, however, it has been suggested [1] that there may be attractor mechanisms at work in the very early universe, before simulations begin, which efficiently drive the field towards the minimum ϕ_*, thereby helping to solve the fine-tuning problem for this model.

Let us now explore the effect the additional RSD data set has on the cosmo-

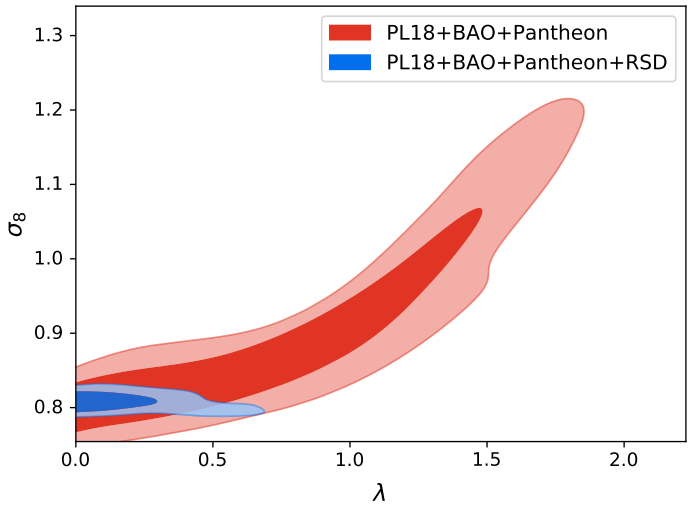

Figure 5.9: 2D marginalised posterior distribution of the present-day mass fluctuation amplitude in spheres of radius $8h^{-1}$Mpc, σ_8, against the slope of the potential, λ, in the M3 model using the PL18+BAO +Pantheon and PL18+BAO+Pantheon+RSD data set combinations. The shaded contours indicate the 1σ and 2σ confidence limits.

logical parameters at a deeper level by looking at the 2D marginalised posterior distributions in Figures 5.8 and 5.9. We see in the $(\phi_{\rm ini}, \alpha)-$plane of Figure 5.8 that the further the initial field value departs from the minimum $\phi_* = 1M_{\rm Pl}$, the lower the allowed values are for the coupling parameter α. This corresponds to what we saw in section 5.1.1 where initial departures of the scalar field from the minimum of coupling result in an early-time enhancement of the effective gravitational constant. The magnitude of the fifth-force is governed by the distance of the field from the minimum ϕ_* *and* the magnitude of the coupling constant α, therefore a degeneracy arises whereby a larger $|\phi_{\rm ini} - \phi_*|$ can be compensated by a smaller coupling constant α and such a correlation is apparent in Figure 5.8. Note that the largest values of α are allowed when the field initially sits at the minimum $\phi_{\rm ini} = 1M_{\rm Pl}$.

Turning our attention to Figure 5.9, where we plot the 2D marginalised posterior distribution in the $(\lambda, \sigma_8)-$plane, we see that when using PL18+BAO +Pantheon data there exists a strong positive correlation between the slope of the potential λ and σ_8. This correlation is due to the fact that if the steepness

Model	ΔG %	σ_8
ΛCDM (PL18+BAO+Pantheon)	0	0.827
M3 (PL18+BAO+Pantheon)	1470	0.962
M3 (PL18+BAO+Pantheon+RSD)	45.0	0.824

Table 5.5: Percentage enhancement of the present-day effective gravitational constant compared to the Newtonian gravitational constant, $\Delta G := (G_{\text{eff},0}/G) - 1$, and the derived value of σ_8 for the ΛCDM and M3 models. We use the upper 68% confidence limit for the coupling parameter α and slope of the potential λ from our data analysis using the PL18+BAO+Pantheon and PL18+BAO+Pantheon+RSD data set combinations.

of the scalar field potential increases, then the field traverses a greater distance from the minimum ϕ_*, therefore there is a stronger enhancement in the effective gravitational constant (eq. (5.1)), which subsequently enhances the amplitude of structure at small to intermediate scales. Note too in Figure 5.8, we see that there exists a positive correlation between the coupling constant α and σ_8 as was the case for the M1 and M2 models investigated in chapter 4. The reason for this degeneracy is the same, the effective gravitational constant is enhanced as the coupling parameter α is increased, therefore there is an increase in the growth of matter thus resulting in a larger value of σ_8 at present-day. The introduction of the RSD data set, which contains measurements on the growth rate and amplitude of structure, heavily constrains the σ_8 parameter as can be seen in Figure 5.9. This in turn heavily constrains the upper bound on the slope of the potential λ and breaks the degeneracy in the $(\lambda, \sigma_8)-$plane, with the degeneracy in the $(\sigma_8, \alpha)-$plane also being broken with the inclusion of this data set. Thus, the inclusion of the RSD data has a powerful constraining effect on the slope of the potential λ.

One interesting feature that the RSD data introduces is that the positive correlation that exists between the coupling constant α and slope of the potential λ when using PL18+BAO+Pantheon data becomes instead a negative correlation. The reason for this is because although the RSD data strongly constrains the present-day value of σ_8, the same value of σ_8 can be achieved by increasing α whilst decreasing λ, or by decreasing α whilst increasing λ, hence a negative correlation between α and λ arises with the addition of this data set. Note, however, that although α is allowed to extremely high values as the slope of the potential approaches zero, the same is not true in the other direction since in the limit $\alpha \to 0$ we recover an uncoupled quintessence model where the slope of the potential is readily constrained by cosmological observations [246]. This behaviour in the $(\lambda, \alpha)-$plane at small values of λ explains the large 2σ contours in Figure 5.8 and the long tail in the 1D distribution of α when using PL18+BAO+Pantheon+RSD as seen in Figure 5.7.

We remark that the IDE model M3 does not help to alleviate the H_0 tension, with the Hubble constant being constrained to $H_0 = 67.73 \pm 0.50\,\mathrm{km\,s^{-1}\,Mpc^{-1}}$ at 1σ in the M3 model compared to $H_0 = 67.75 \pm 0.43\,\mathrm{km\,s^{-1}\,Mpc^{-1}}$ at 1σ in the ΛCDM model, using the PL18+BAO+Pantheon data set combination for both models. Owing to an increase in σ_8 and matter density Ω_m compared to ΛCDM, the M3 model appears to worsen the S_8 tension, deriving a value of $S_8 = 0.925^{+0.033}_{-0.12}$ at 1σ compared to the ΛCDM derived value of $S_8 = 0.823 \pm 0.013$ at 1σ when using the PL18+BAO+Pantheon data set combination, although we note that a full data analysis and comparison with cosmic shear data [72, 73, 74] is needed before more can be said about this model's effect on the S_8 tension.

We see in Table 5.3 that the natural logarithm of the Bayes factor with respect to the ΛCDM model, $\ln B_{i,\Lambda\mathrm{CDM}}$, is negative for all data set combinations, thus indicating that ΛCDM is the preferred model over the M3. The introduction of three extra scalar field parameters, α, λ, and ϕ_{ini}, into the cosmological model is not enough to account for the increase in model complexity.

Finally, let us look at how strong the fifth-force is allowed to currently be under the cosmological data considered in our analysis. In the IDE model M3, the

enhancement of the effective gravitational constant depends on both the coupling constant α and the distance traversed by the scalar field from the minimum of the coupling ϕ_*. Therefore, for a given model, we use the best fit values of the cosmological parameters into the `CLASS` Boltzmann code to work out the field value at present-day and hence evaluate the present-day effective gravitational constant, $G_{\rm eff,0}$. For the scalar field parameters α and λ, we use the upper 1σ limits as shown in Table 5.3. In Table 5.5 we report the present-day enhancement of the effective gravitational constant, and also the derived value of σ_8, for the ΛCDM and M3 models where we display the results from the PL18+BAO+Pantheon and PL18+BAO+Pantheon+RSD data set combinations for the M3 model. We see that current cosmological observations of the CMB anisotropies and background observables allow for a fifth-force that is over ten times the strength of gravity at present-day. The addition of the RSD data sharply brings down this increase owing to a tighter constraint on the slope of the potential λ, reporting a still sizeable fifth-force that is approximately half the strength of gravity. The M3 model using PL18+BAO+Pantheon data results in a derived σ_8 parameter that is apparently at odds with inferences from large-scale structure measurements [247] and we are excited to see results from analysis using cosmic shear data [72, 73, 74] and galaxy clustering measurements [248], but leave this study for future work.

5.4 Conclusions

In this chapter, we introduced a new class of interacting dark energy models where the DE-DM coupling has a minimum at some finite field value, resulting in a fifth-force that emerges at the onset of DE domination. We explored some of the background and perturbation level effects of this model and found that effects on expansion history and the CMB anisotropies were quite small, deviating only minimally from ΛCDM and an uncoupled quintessence model for a wide range of parameters. This means that a present-day fifth-force which is potentially quite large would be allowed under standard cosmological probes. Perhaps the most

significant effect, however, was found at small scales in the linear matter power spectrum predictions.

We then confronted this IDE model with cosmological data and subsequently derived constraints on the IDE model parameters. We found that when using CMB observations and background data sets, the slope of the scalar field potential λ and coupling constant α are not heavily constrained. Indeed at 1σ they allow for a present-day fifth-force that is over ten times the strength of gravity. Since we saw that a particularly sensitive probe of this IDE model was its predictions of structure formation at small to intermediate scales, we decided to use an additional data set containing measurements on the growth rate and amplitude of large-scale structure. The addition of this data set was effective in constraining the slope of the potential λ but not the coupling constant α, because of a degeneracy that arose between the two parameters. This tighter constraint on the slope of the potential λ allows for the present-day fifth force to be approximately half the strength of gravity using the 68% confidence limits for α and λ. This is in sharp contrast to constant fifth-force models, such as those explored in chapter 4, where the fifth-force is constrained to be $< 1\%$ the strength of gravity.

The possibility of a fifth-force in the dark sector emerging at late-times due to the onset of dark energy domination remains an exciting possibility. We saw that whilst traditional data analysis techniques using background and linear perturbation level data could constrain such a model, they weren't too effective in doing so, and allow for a potentially strong long-range fifth force in the current epoch. The introduction of a gravity-like fifth-force between DM particles would result in an apparent equivalence principle violation in the dark sector [249]. Therefore, the search for dark sector equivalence principle violations at different redshifts is an important task for cosmology today. Indeed, what this work suggests is the possibility of a dark sector equivalence principle violation that is only made apparent at late-times, with the onset of dark energy domination. We expect that tests of violations of the equivalence principle in the dark sector, such as the tidal tails test [250], will be effective in constraining this model further.

We saw that a distinct imprint of this model was at small scales in structure

formation probes, and indeed, the introduction of data containing information on structure formation heavily constrained this model compared to when using only CMB and background data sets. We expect that deviations from ΛCDM and an uncoupled quintessence model will be more significant at very small scales, where perturbation theory at the linear level is no longer valid. We predict that this IDE model will leave a distinct imprint in the evolution of non-linear perturbations and in the formation of non-linear structures, such as dark matter halos [251], and will also affect the matter power spectrum at small scales. Investigations of this sort could be undertaken through the use of N-body codes [252], for example, and interacting dark energy models have been explored through these methods [253]. In the next chapter, we will look at cosmology at the smaller scale and the role that a dark sector interaction may play in it.

6 — Beyond the linear regime

With the rapid rise in computing power and increasing precision in the determination of cosmological parameters, the role of structure formation, especially at the small and non-linear scale, is making its way to the forefront of cosmology. The standard model of cosmology, ΛCDM, has been shown to be in excellent agreement with CMB observations and background measurements [50], however, in recent years some tensions have arose which seem to challenge the concordance model, a few of which we explored in chapter 2. These tensions could be potentially be down to systematic errors and statistical fluctuations, however, they could also be hints of cosmology beyond the ΛCDM model [254, 71, 247].

One such tension we saw was a discrepancy in determinations of the S_8 parameter (eq. (2.11)) from measurements of large-scale cosmic shear surveys [72, 73, 74] and the CMB as measured by *Planck* [50]. For the ΛCDM model, this tension amounts to CMB observations predicting too great an amplitude of structure at present day when compared to results from more direct probes of large-scale structure, such as cosmic shear experiments. However, there also exist tensions in the ΛCDM model at smaller scales in non-linear structures, such as the 'core-cusp' problem in predictions of the mass density of galactic dark matter halos [255]. The possibility of there being a real discrepancy between predictions of ΛCDM and astrophysical observations rests upon the accuracy of cosmological N-body simulations, therefore it is imperative that N-body codes are routinely and rigorously checked by independent teams such that their particular approximations and assumptions can be tested for validity. As cosmological simulations become increasingly sophisticated and exact, and as surveys and observations

of smaller-scale structures become increasingly more detailed, will more tensions arise in the concordance model?

It is interesting to note that results from N-body simulations have suggested that the effects of a dark sector interaction in the small-scale, non-linear regime may help to ease several tensions that are present in the ΛCDM model, with authors finding that the degree to which the tensions could be eased was correlated with the strength of the coupling [253]. The dark sector coupling, β, was assumed to be constant in those simulations, however, as we saw in chapter 4, cosmological observations put a very tight constraint on the magnitude of such a coupling and therefore strongly limit the degree to which these tensions can be alleviated.

We found in chapter 5, however, that if the dark sector coupling is allowed to vary with time such that the fifth-force is negligible until recent times, then the strength of the fifth-force today can be significantly higher than in a constant coupling model. This opens up the window again for the consideration of a dark sector interaction in the search for a solution to these problems. Indeed, promising results from N-body simulations where time-dependent couplings were considered [256] suggests that these models can help to resolve astrophysical tensions whilst not strongly effecting the background dynamics of the universe. It would be interesting to see a full data analysis of the models considered in these simulations, in the manner seen in chapters 4 and 5 for example, to see what upper bounds cosmological observations put on the strength of the couplings and therefore whether or not these models can be considered viable solutions.

The minimum strength the coupling must possess in order to resolve a particular tension must be in agreement with the maximum strength allowed by cosmological and astrophysical observations for the model to survive, and we eagerly await further results from both of these fronts. But aside from exploring extensions to ΛCDM in the search for possible solutions to current tensions, we may utilise N-body simulations in constraining cosmological models too [257, 258]. Since non-linear effects in structure formation become especially important at late-times $z \lesssim 2$ [259], we expect that IDE models where the fifth-force switches

on at late-times and then grows in magnitude will be effectively constrained when investigating its non-linear signatures.

We are not at a stage yet where N-body simulations are ubiquitously used to constrain cosmological models, partly because of their computational cost, and partly because analysis at the background and linear level is effective in constraining a wide variety of models [187, 246, 260]. However, as the abundance of high-quality large-scale cosmological data continues to increase, more and more cosmological models will be ruled out, and those that survive will need different angles of attack in order to be differentiated from one another and ultimately ruled out. N-body codes probing the non-linear regime offer, therefore, a unique insight into competing models and hopefully will be able to reveal more about the nature of the dark sector.

Due to the late-onset of the fifth-force in the model considered in chapter 5, our attention was turned to the impact of the coupling on non-linear objects in the universe, such as galaxies and galaxy clusters, that have already virialised. In particular, we were interested in whether or not the late-time coupling could affect the virialisation state of the object. Awaiting results from a fully cosmological N-body simulation, we decided to test the idea by implementing the fifth-force into a simple non-cosmological N-body code. In section 6.1, we briefly review the interacting dark energy model of interest, we discuss the implementation of the model and then explore its effects on a virialised system, finally concluding in section 6.2.

6.1 N-body simulations

In this chapter we consider the IDE model introduced in chapter 5 where the dark sector coupling switches on as the field begins to roll away from the minimum, causing energy to flow DE $\rightarrow$ DM and the masses of DM particles to increase according to $m_{DM} \propto \sqrt{C(\phi)}$. This growth in the coupling results in an effective gravitational constant G_{eff} that also grows with time.

6.1.1 The virial theorem

Since we are interested in the effect the coupling has on virialised structures, let us briefly recall that the virial theorem in the context of a self-gravitating and stable system of discrete particles states that the moment of inertia I, kinetic energy K, and potential energy W of the system can be related by [261]

$$\frac{1}{2}\frac{d^2I}{dt^2} = 2K + W. \tag{6.1}$$

Over large enough time spans, systems of this form tend to approach a steady-state such that $d^2I/dt^2 = 0$ [261], and hence we obtain the following relation for the kinetic energy and potential energy of the system

$$0 = 2K + W. \tag{6.2}$$

If this relation holds true for an object, then that object is said to be virialised. Galaxies and galaxy clusters are often considered to be virialised since they have existed long enough to approach dynamical equilibrium [262], and the virial theorem is ubiquitously applied to such structures in, for example, determinations of the virial mass [263]. We may introduce a virial ratio parameter $b_{vir} = 2K/|W|$ which measures the degree to which a system is virialised. For a perfectly virialised system, the virial theorem holds exactly and so $b_{vir} = 1$, with any deviations from the virial theorem amounting to $b_{vir} \neq 1$.

One can imagine then, that if a sudden energy exchange is introduced into the system as a result the dark sector coupling switching on, such that the DM particles begin to experience an additional fifth force and their masses begin to vary, then this could perturb the system out of virial equilibrium and therefore eq. (6.2) may no longer hold.

6.1.2 Set up of simulations

In the context of the N-body simulation we consider, the dark sector coupling introduces two features following the procedure outlined in [264, 253]. The first

is that the masses of the DM particles now vary with time and the second is that DM-DM particle interactions are now governed by an enhanced effective gravitational constant G_{eff} which accounts for the additional fifth-force, as opposed to the Newtonian gravitational constant G which governs DM-baryon and baryon-baryon interactions.

In our discrete system of particles, the equation of motion for a baryon particle is given by

$$\dot{\mathbf{v}}_i = \sum_{j \neq i} G m_j \frac{\mathbf{r}_j - \mathbf{r}_i}{|\mathbf{r}_j - \mathbf{r}_i|^3}, \tag{6.3}$$

where $\dot{\mathbf{v}}_i = d\mathbf{v}_i/dt$ is the acceleration of baryon particle i with velocity $\mathbf{v}_i$, G is the Newtonian gravitational constant, m_j is the mass of particle j, and $\mathbf{r}_i, \mathbf{r}_j$ are the position vectors of particles i, j respectively. Since the DM particle masses vary with time, the rate of change of momentum for a DM particle i is

$$\begin{aligned} \dot{\mathbf{p}}_i &= \dot{m}_i \mathbf{v}_i + m_i \dot{\mathbf{v}}_i \\ &= m_i \beta \frac{\dot{\phi}}{M_{\text{Pl}}} \mathbf{v}_i + m_i \dot{\mathbf{v}}_i. \end{aligned} \tag{6.4}$$

Moreover, DM-DM particle interactions are characterised by an enhanced gravitational constant G_{eff} and so we introduce a generalised gravitational constant G_{ij} such that $G_{ij} = G_{\text{eff}}$ for all DM-DM interactions and $G_{ij} = G$ for all baryon-baryon and baryon-DM interactions. The equation of motion for a DM particle is then

$$\dot{\mathbf{v}}_i = \sum_{j \neq i} G_{ij} m_j \frac{\mathbf{r}_j - \mathbf{r}_i}{|\mathbf{r}_j - \mathbf{r}_i|^3} - \beta \frac{\dot{\phi}}{M_{\text{Pl}}} \mathbf{v}_i, \tag{6.5}$$

where we see that the coupling has introduced an additional velocity term into the acceleration equation for DM particles. In our setup, we have $\beta > 0, \dot{\phi} > 0$, therefore this term constitutes a dragging term slowing down the acceleration of DM particles, however, if β and $\dot{\phi}$ were of opposite signs, then this term would boost the acceleration of the DM particles. Finally, if we define a generalised coupling parameter β_i such that $\beta_i = 0$ for baryons and $\beta_i = \beta$ for DM particles,

then we can write an equation of motion for a general particle i as

$$\dot{\mathbf{v}}_i = \sum_{j \neq i} G_{ij} m_j \frac{\mathbf{r}_j - \mathbf{r}_i}{|\mathbf{r}_j - \mathbf{r}_i|^3} - \beta_i \frac{\dot{\phi}}{M_{\rm Pl}} \mathbf{v}_i. \tag{6.6}$$

Therefore, in the equation of motion for a particle in the system, there are three effects in total which the coupling introduces, an enhancement in the gravitational force between DM particles, a time-varying mass in DM particles, and an additional friction term in the equation of motion for a DM particle.

In our simulations, we consider a system of n_b baryon particles and n_{dm} coupled DM particles, together making up $N = n_b + n_{dm}$ particles in total, where the masses of the baryon and DM particles are all assumed to be equal to begin with. A common feature of the constant time-step algorithm we use is that it does not behave well when the separation distance between particles is very small and furthermore, if we smooth out the potential in the equations of motion, then the graininess of the system is reduced and the system better describes one with a continuous mass distribution, that is, one characterised by the collisionless Boltzmann equation [265, 266]. Therefore, a popular remedy is to replace the Newtonian potential with the smoothed Plummer sphere potential [267] such that the acceleration of particle is now described by [268]

$$\dot{\mathbf{v}}_i = \sum_{j \neq i} G_{ij} m_j \frac{\mathbf{r}_j - \mathbf{r}_i}{(|\mathbf{r}_j - \mathbf{r}_i|^2 + \epsilon^2)^{3/2}} - \beta_i \frac{\dot{\phi}}{M_{\rm Pl}} \mathbf{v}_i, \tag{6.7}$$

where ϵ is the softening parameter. We can see from this equation that if ϵ is too large, then the force can no longer reasonably be considered Newtonian, whereas if ϵ is too small, then we encounter the same problems which led to its introduction. An optimal choice for the softening parameter should be therefore be made so as to minimise errors in force calculations. We follow the work of [268, 269] in choosing the optimal value for the softening parameter ϵ for our simulations.

We modify a simple, non-cosmological N-body Python code [270] where the equations of motion are integrated using the second-order leapfrog method in the

'kick-drift-kick' form [271] and where we adopt Hénon units [272] in the setup of our runs such that the total energy is $E_{\rm tot} = -1/4$, the Newtonian gravitational constant is $G = 1$, and the total mass is $M_{\rm tot} = 1$. The initial positions of the particles are randomly distributed with spherical symmetry and the initial velocities are taken to be zero such that the system undergoes a cold collapse before virialising. We are primarily interested in the virialisation of the system and deviations thereof, therefore, the main quantity of interest is the virial ratio b_{vir} and its evolution in time.

The simulations run until the system virialises, $b_{vir} \approx 1$, after which the coupling is switched on. The DM particles then begin to experience an enhanced gravitational constant $G_{\rm eff}$, a growth in their masses $m_{DM} \propto \sqrt{C(\phi)}$, and an additional friction term in their equations of motion, in contrast to before the switch-on, where the baryon and DM particles were indistinguishable. We allow the simulations to run further under the influence of the coupling and then end the simulations. We allow the coupling to evolve over several crossing times, with the enhancement of a DM particle mass being $\approx 10\%$ and the size of the fifth-force being approximately four times the strength of gravity by the time simulations end.

In our runs, we consider a system of $N = 10^4$ particles with a fixed time-step $\Delta t = 0.01$ and a fixed softening parameter $\epsilon = 0.01$. We set the proportion of the number of baryons in the system to be $n_b/N \approx 10\%$ and randomly distributed the baryon and DM particles in the manner outlined above.

6.1.3 RESULTS

The results for our simulations are shown in Figure 6.2 where we show the evolution of the virial ratio deviation, $\Delta b_{\rm vir} = b_{\rm vir} - 1$, during early and late phases in the simulation. We plot the evolution of $\Delta b_{\rm vir}$ over N-body time in units of crossing time t_{cr}, where one unit of crossing time is equal to $t_{cr} = 2\sqrt{2}$ in Hénon units [272]. We also provide a snapshot of our simulation in Figure 6.1 before its initial collapse phase and plot the evolution of the effective gravitational constant $G_{\rm eff}$ in Figure 6.3.

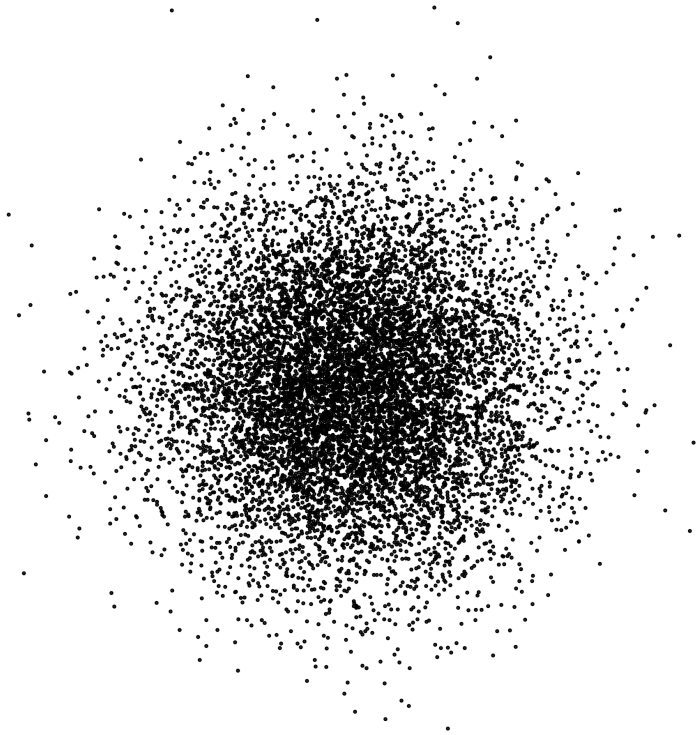

Figure 6.1: A snapshot of our simulation during its initial phase.

In the upper panel of Figure 6.2, we plot $\Delta b_{\rm vir}$ during the initial phase of the simulation, before the coupling has been switched on, spanning from $t = 0$ to $t \approx 5.5 t_{cr}$. We see in this figure that since we set up the system to initially have zero kinetic energy, the virial ratio b_{vir} is initially vanishing too. However, as the particles begin to gravitate and draw closer together, their kinetic energy increases. The system then quickly undergoes a collapse phase whereby the system rapidly contracts and the particles are densely drawn together. The system then expands briefly, with the virial ratio b_{vir} reaching a maximum at $t \approx 1.5 t_{cr}$, before the system begins contracting again. The system continues to contract be-

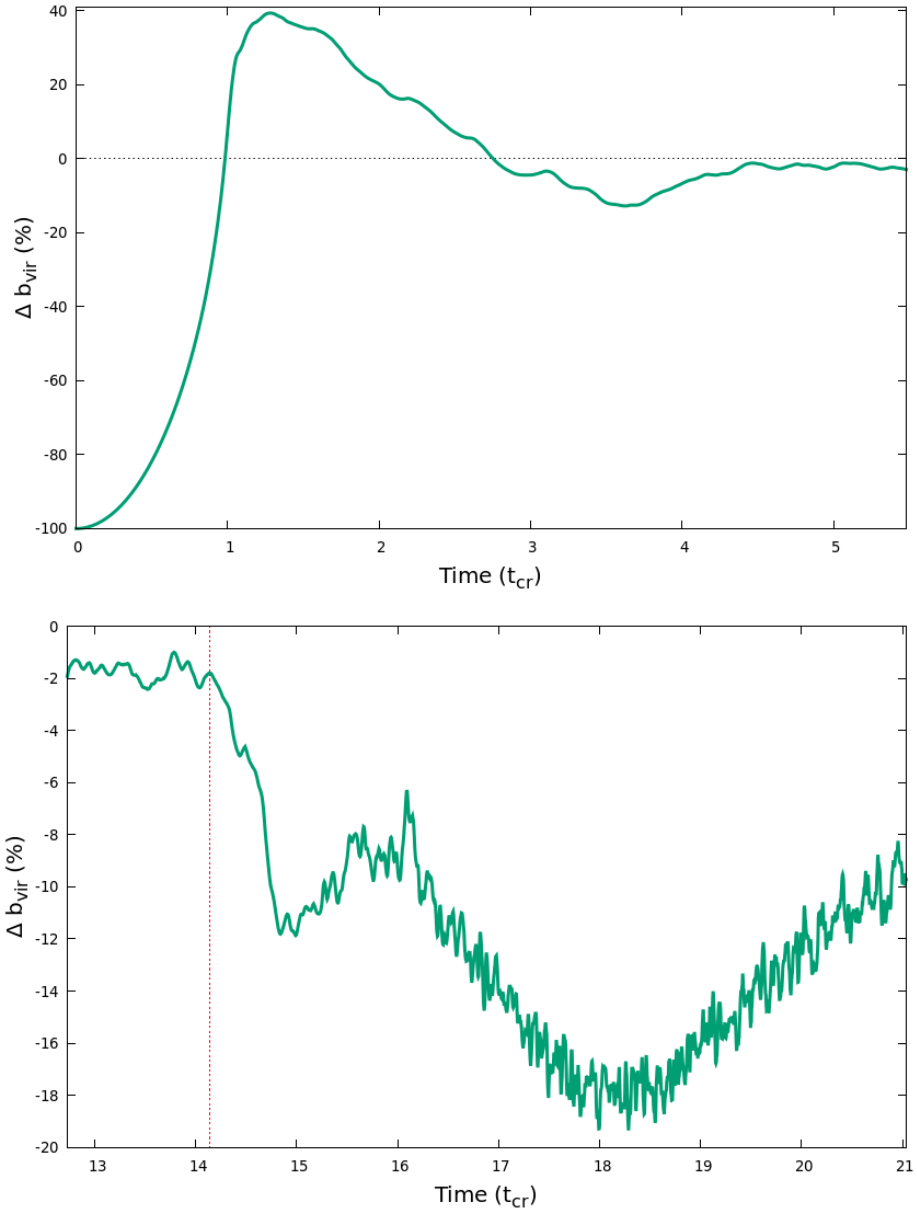

Figure 6.2: The evolution of the percentage deviation of the virial ratio from a virialised system, where $\Delta b_{\rm vir} = b_{\rm vir} - 1$ over time in units of crossing time t_{cr}. In the upper panel we plot the evolution in the initial phase of the simulation, during which the system undergoes a cold collapse and then reaches virial equilibrium. In the lower panel we plot the evolution during the latter stages of the simulation, during which the coupling is switched on. The vertical red line in the lower panel figure marks the time the coupling is switched on.

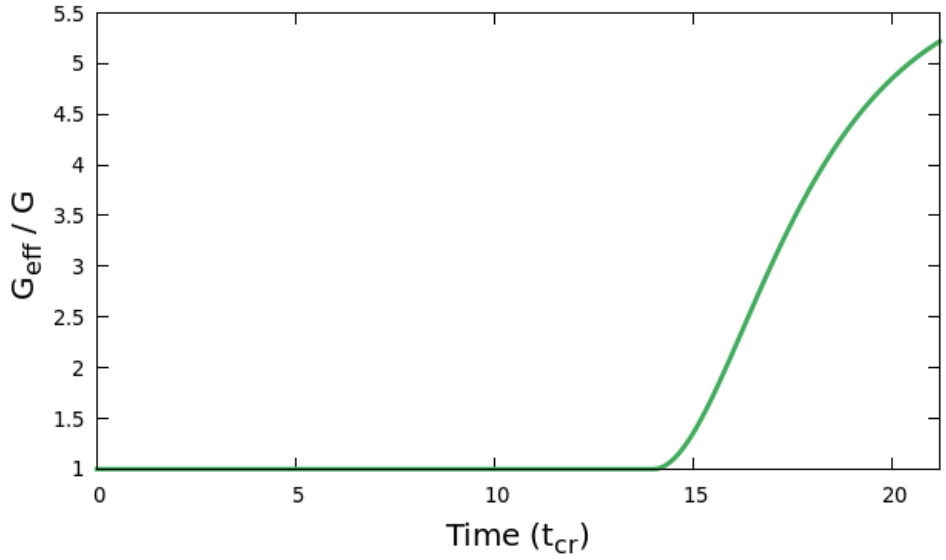

Figure 6.3: The evolution of over time of the ratio G_{eff}/G where G_{eff} is the effective gravitational constant experienced by DM particles in DM-DM interactions and G is the Newtonian gravitational constant.

fore expanding once more, then settling into a steady state by the time $t \approx 5t_{cr}$, with the deviation from a perfectly virialised state being within a few percent. We allow the system to remain in dynamical equilibrium before switching on the coupling at $t \approx 14t_{cr}$.

In the lower panel of Figure 6.2 we plot evolution of Δb_{vir} but during the latter stages of the simulation, when the coupling is switched on. The coupling is switched on at $t \approx 14t_{cr}$, as indicated by the vertical red line, and is allowed to act until the end of the simulation at $t \approx 21t_{cr}$. We see in this figure that immediately after the field is switched on, the virial ratio begins to deviate significantly from the virialised value of $b_{vir} = 1$. The additional fifth-force causes an increase in the acceleration of DM particles and thus an increase in their kinetic energy, however, the increase is diminished by the presence of the friction term seen in eq. (6.5). The potential energy also increases due to the increase in DM particle mass and increase in effective gravitational constant in DM-DM particle interactions. When the coupling first switches on, the increase in potential energy dominates

the increase in kinetic energy and so the system begins to contract, driving b_{vir} down. This is followed by a short expanding phase starting at $t \approx 15t_{cr}$ but quickly ending at $t \approx 16t_{cr}$, after which the system contracts, followed by another expansion phase starting at $t \approx 18t_{cr}$ which continues until our simulation ends at $t \approx 21t_{cr}$.

We see that this in this model, the increase in kinetic energy due to the fifth-force is not outweighed by the increase in the potential energy of system, thus having the effect of decreasing the virial ratio and causing the system to contract. One interesting area of investigation would be for IDE models where β and $\dot{\phi}$ are of opposite sign, such that the friction term in the equation of motion for DM particles changes sign and so enhances the acceleration. In this case, it may be possible for the coupling to cause the system to ultimately expand due to the increase in kinetic energy, and thus, a dark sector coupling could, for instance, predict either a greater or lower dark matter halo concentration than ΛCDM does [256].

We see in these simulations that it is possible for a dark sector coupling to disturb the virialisation state of a system previously existing in dynamical equilibrium. This could potentially have implications in the determinations of quantities which assume the virialisation state of a system, such as the virial mass of a galaxy cluster. Whether or not the coupling does indeed have a significant impact on the virialisation state of a non-linear structure in our universe will be revealed by the results of a cosmological N-body simulation, but it is an interesting and stimulating result nonetheless.

6.2 CONCLUSIONS

In this chapter, we began by motivating the need to look at smaller-scale structures in cosmology and hence the need for accurate N-body simulations. We saw in chapter 5 that background and linear perturbation level data do not strongly constrain a model whereby the dark sector coupling switches on at late-times, and so our attention turned to the small-scale, non-linear regime where we expect that

the imprints of such a model will be far more pronounced.

Due to the late-onset of the coupling in this model, our interest was particularly directed towards the effects this model may have on already virialised structures, such as galaxies and galaxy clusters. In anticipation of results coming from a cosmological N-body simulation, we decided to implement the model into a simple non-cosmological N-body code. We let the simulation run until virial equilibrium was achieved, after which we switched on the dark sector coupling. We saw that this disturbed the equilibrium state of the system and the virial ratio b_{vir} began to deviate significantly from its virialised value, thus demonstrating that a late-time dark sector coupling can have an effect on the virialisation state of an object *per se*. Although we only considered a simplified non-cosmological model in our analysis, this work promotes and motivates the need for a full and thorough treatment to be undertaken using cosmological N-body techniques, such as through the use of codes like `Gadget` [273], `Isis` [258], and `ECOSMOG` [274].

As determinations of the large-scale structure and expansion history of the universe become evermore precise, the remaining viable theories will need to be tackled in new ways in order to be constrained. The advent of next-generation surveys such as Euclid [275], LSST [276], and SKA [277] will bring fresh opportunity for cosmology at smaller scales, and will be especially relevant for fifth-force models, since the effects of a fifth-force are thought to be highly significant at these scales [278]. Beyond large-scale measurements of the matter power spectrum and halo mass function, we can look to even smaller-scales and more novel and unexplored ways of constraining extensions to ΛCDM thanks to the advances in computation, such as looking at the predicted velocity dispersion and density profiles of individual dark matter halos [279]. In one approach, a team of researchers managed to tightly constrain a modified gravity theory by comparing the gas observations and lensing measurements of the Coma galaxy cluster [280], and other novel approaches include looking for signs of equivalence principle violations in the dark sector at the galactic scale [250, 281].

Therefore, alongside data analysis techniques using large-scale cosmological observations at the background and linear level, we urge interest to be taken

in new frontiers, beyond the linear regime, so as to thoroughly investigate the cosmological standard model on all fronts and to see if any deeper insight can be gained into the mysterious nature of the dark sector of our universe.

7 — Conclusions

In this thesis we began by giving brief history of cosmology, from its theoretical foundations in General Relativity, through to its cosmological applications by virtue of the Friedmann-Lemaître-Robertson-Walker metric. After specifying the various matter species of the universe, we reflected upon the triumphant discovery of the Cosmic Microwave Background, and how together these led to the formation of the six-parameter standard model of cosmology, ΛCDM. We saw that, despite its numerous successes, there are some serious problems present in the ΛCDM model which merit sincere attention.

One of the most severe problems in the standard model is to do with one of its most fundamental ingredients, the cosmological constant Λ. The cosmological constant problem corresponds to a grave disagreement between two pillars of modern physics, General Relativity and Quantum Field Theory, and therefore it is no wonder why it has so deeply troubled the scientific community. But not only that, the cosmological constant also suffers from the problem of cosmic coincidence too, hence cosmologists began to look elsewhere to see if nature could provide any other explanation for the accelerated expansion of our universe.

Then along came the idea of quintessence, a light scalar field slowly rolling down its potential, which was proposed as an explanation for the source of dark energy and has remained an extremely promising possibility up to present day. However, if such a quintessence scalar field exists, then it should be coupled explicitly to the various matter species of our universe unless such a coupling is forbidden by some symmetry condition. We saw that, although couplings to baryons have been heavily constrained, the same is not true for couplings to

dark matter, and therefore our attention turned towards the possibility of such interactions in an interacting dark energy model.

We introduced an interacting dark energy model in the framework of a scalar-tensor theory, whereby the minimally coupled quintessence scalar field is conformally coupled to dark matter, and explored its background and perturbation level dynamics and cosmological imprints. Finding that the interacting dark energy model had a distinct effect on the imprints in our universe, we decided to confront the model with recent cosmological observations to see what bounds nature puts on it. We found that for this model, whereby the dark sector coupling is constant, the strength of the fifth-force was constrained to be very small at $< 1\%$ the strength of gravity.

This led us to consider other possible forms of couplings that had not been explored as thoroughly, and found that if we begin with the assumption that the conformal coupling function has a minimum at some finite field value, then this can lead to a fifth-force that emerges only at late-times with the onset of dark energy domination. We then investigated the background and perturbation level imprints of this model and found that it was hardly distinguishable from an uncoupled quintessence model for a large range of parameter values, despite potentially possessing a very strong fifth-force at present day. We confronted this model with the same cosmological data sets as for the constant fifth-force models and found that, in contrast, the fifth-force was allowed to be very strong at present day at over ten times the strength of gravity. In an effort to see if this model could be constrained further, we noted that it predicts a large amplitude of structure and so added observations of large-scale galaxy redshift-space distortions to our analysis. We found that this additional data set effectively constrained the model and brought down the strength of the fifth-force to approximately half the strength of gravity at present day, still fifty times stronger than in a constant fifth-force model.

Our cosmological data analysis highlighted the fact that this model was especially sensitive in its predictions of structure formation, and so our attention turned to smaller scales, where we expect that the imprints of such a model will

be highly significant. We remarked that background and linear perturbation level data may have its limitations in constraining models in the future, and therefore we must look towards new and less explored ways of testing the standard model and its extensions. We saw that tensions exist for the ΛCDM model at the small, non-linear scale too and that extensions such as an interacting dark sector can help to alleviate these tensions. Furthermore, N-body simulations suggest that models whereby the fifth-force switches on at late-times have a unique and significant impact at the non-linear scale, and we therefore expect these models to feature prominently in the future of such research. Finally, we remarked on the possibility of constraining extended models through N-body simulations, and speculated that they may be able to constrain regions of the parameter space where background and linear perturbation level data cannot reach.

In the future, we hope to see cosmological data analysis paired with N-body simulations, which together, will hopefully shine a brighter light into the darker, more obscure corners of our universe and ultimately tell us more about this place we call home.

Bibliography

[1] C. van de Bruck and C. C. Thomas. Dark Energy, the Swampland, and the Equivalence Principle. *Physical Review D*, 100(2), July 2019.

[2] C. C. Thomas and C. van de Bruck. Constraints on Late Time Violations of the Equivalence Principle in the Dark Sector. *Journal of Cosmology and Astroparticle Physics*, 2023(04):015, April 2023.

[3] W. Hu, M. Fukugita, M. Zaldarriaga, and M. Tegmark. Cosmic microwave background observables and their cosmological implications. *The Astrophysical Journal*, 549(2):669–680, March 2001.

[4] A. G. Riess, S. Casertano, W. Yuan, L. M. Macri, and D. Scolnic. Large Magellanic Cloud Cepheid Standards Provide a 1% Foundation for the Determination of the Hubble Constant and Stronger Evidence for Physics beyond ΛCDM. *The Astrophysical Journal*, 876(1):85, May 2019.

[5] M. Burnyeat, M. J. Levett, and Plato. *The Theaetetus of Plato / Myles Burnyeat ; with a translation of Plato's Theaetetus by M.J. Levett, revised by Myles Burnyeat.* Hackett Indianapolis, 1990.

[6] A. Einstein. *Die Feldgleichungen der Gravitation*, pages 88–92. John Wiley Sons, Ltd, 2005.

[7] S. Chandrasekhar. Verifying the theory of relativity. *Bulletin of the Atomic Scientists*, 31(6):17–22, 1975.

[8] U. J. Le Verrier. Theorie du mouvement de Mercure. *Annales de l'Observatoire de Paris*, 5:1, 1859.

[9] R. S. Park, W. M. Folkner, A. S. Konopliv, J. G. Williams, D. E. Smith, and M. T. Zuber. Precession of mercury's perihelion from ranging to the messenger spacecraft. *Astronomical Journal (New York, N.Y. Online)*, 153(3), 3 2017.

[10] J. Soldner S. L. Jaki. *Johann Georg von Soldner and the gravitational bending of light.* Plenum Press, New York NY, 1978.

[11] F. W. Dyson, A. S. Eddington, and C. Davidson. A Determination of the Deflection of Light by the Sun's Gravitational Field, from Observations Made at the Total Eclipse of May 29, 1919, 1920.

[12] B. P. Abbott et al. Observation of gravitational waves from a binary black hole merger. *Physical Review Letters*, 116(6), February 2016.

[13] B. P. Abbott et al. Gravitational waves and gamma-rays from a binary neutron star merger: GW170817 and GRB 170817a. *The Astrophysical Journal*, 848(2):L13, October 2017.

[14] B. P. Abbott et al. GW170817: Observation of gravitational waves from a binary neutron star inspiral. *Physical Review Letters*, 119(16), October 2017.

[15] S. Chandrasekhar. The general theory of relativity - Why 'It is probably the most beautiful of all existing theories'. *Journal of Astrophysics and Astronomy*, 5:3–11, 1984.

[16] S. Carroll. *Spacetime and Geometry: An Introduction to General Relativity.* Benjamin Cummings, 2003.

[17] M. P. Haugan and C. Lämmerzahl. Principles of equivalence: Their role in gravitation physics and experiments that test them. In *Gyros, Clocks, Inter-*

ferometers...: Testing Relativistic Graviy in Space, pages 195–212. Springer Berlin Heidelberg.

[18] D. Hilbert. Die Grundlagen der Physik. *Nachrichten von der Gesellschaft der Wissenschaften zu Göttingen, Mathematisch-Physikalische Klasse*, 1915:395–408, 1915.

[19] A. Einstein. Kosmologische Betrachtungen zur allgemeinen Relativitätstheorie. *Sitzungsberichte der Königlich Preussischen Akademie der Wissenschaften*, pages 142–152, 1917.

[20] Ya. B. Zel'dovich. The cosmological constant and the theory of elementary particles. *Sov. Phys. Usp.*, 11:381–393, 1968.

[21] B. Falkenburg and W. Rhode. *From Ultra Rays to Astroparticles: A Historical Introduction to Astroparticle Physics*. SpringerLink : Bücher. Springer Netherlands, 2012.

[22] S. W. Hawking and G. F. R. Ellis. *The Large Scale Structure of Space-Time (Cambridge Monographs on Mathematical Physics)*. Cambridge University Press, 1975.

[23] W. de Sitter. On Einstein's Theory of Gravitation and its Astronomical Consequences. Third Paper. *Monthly Notices of the Royal Astronomical Society*, 78(1):3–28, 11 1917.

[24] K. Lanczos. 24, 539-543. *Annalen der Physik*, 1922.

[25] A. Friedmann. Über die Krümmung des Raumes. *Zeitschrift fur Physik*, 10:377–386, 1922.

[26] G. Lemaître. Un Univers homogène de masse constante et de rayon croissant rendant compte de la vitesse radiale des nébuleuses extra-galactiques. *Annales de la Société scientifique de Bruxelles*, 47:49–59, 1927.

[27] E. Hubble. Extragalactic nebulae. *The Astrophysical Journal*, 64:321–369, 1926.

[28] E. Hubble. A Relation between Distance and Radial Velocity among Extra-Galactic Nebulae. *Proceedings of the National Academy of Science*, 15(3):168–173, 1929.

[29] A. S. Eddington. On the Instability of Einstein's Spherical World. *Monthly Notices of the Royal Astronomical Society*, 90(7):668–678, 05 1930.

[30] A. Einstein and W. de Sitter. On the Relation between the Expansion and the Mean Density of the Universe. *Proceedings of the National Academy of Science*, 18(3):213–214, 1932.

[31] H. Nussbaumer and L. Bieri. Discovering the expanding universe. *Cambridge: 2009*, May 2009.

[32] The New York Times. Report on the meeting with Einstein of February 11, 1931.

[33] G. Lemaître. The Beginning of the World from the Point of View of Quantum Theory. *Nature*, 127(3210):706, May 1931.

[34] S. Chandrasekhar and L. R. Henrich. An Attempt to Interpret the Relative Abundances of the Elements and Their Isotopes. *The Astrophysical Journal*, 95:288, 1942.

[35] G. Gamow. Expanding universe and the origin of elements. *Phys. Rev.*, 70:572–573, October 1946.

[36] R. A. Alpher, H. Bethe, and G. Gamow. The origin of chemical elements. *Phys. Rev.*, 73:803–804, April 1948.

[37] R. A. Alpher and R. Herman. Evolution of the universe. *Nature 162, 774–775*, 73:803–804, April 1948.

[38] H. Bondi and T. Gold. The Steady-State Theory of the Expanding Universe. *Monthly Notices of the Royal Astronomical Society*, 108(3):252–270, 06 1948.

[39] F. Hoyle. A New Model for the Expanding Universe. *Monthly Notices of the Royal Astronomical Society*, 108(5):372–382, 10 1948.

[40] F. Hoyle. On Nuclear Reactions Occuring in Very Hot Stars. I. the Synthesis of Elements from Carbon to Nickel. *APJS*, 1:121, 1954.

[41] E. M. Burbidge, G. R. Burbidge, W. A. Fowler, and F. Hoyle. Synthesis of the elements in stars. *Rev. Mod. Phys.*, 29:547–650, October 1957.

[42] A. A. Penzias and R. W. Wilson. A Measurement of Excess Antenna Temperature at 4080 Mc/s. *The Astrophysical Journal*, 142:419–421, 1965.

[43] R. H. Dicke, P. J. E. Peebles, P. G. Roll, and D. T. Wilkinson. Cosmic Black-Body Radiation. *The Astrophysical Journal*, 142:414–419, 1965.

[44] A. G. Walker. On Milne's Theory of World-Structure. *Proceedings of the London Mathematical Society*, s2-42(1):90–127, 01 1937.

[45] H. P. Robertson. Kinematics and World-Structure III. *The Astrophysical Journal*, 83:257, May 1936.

[46] A. Friedmann. Über die Möglichkeit einer Welt mit konstanter negativer Krümmung des Raumes. *Zeitschrift fur Physik*, 21(1):326–332, 1924.

[47] S. Perlmutter et al. Measurements of Ω and Λ from 42 High-Redshift Supernovae. *The Astrophysical Journal*, 517(2):565–586, June 1999.

[48] A. G. Riess et al. Observational evidence from supernovae for an accelerating universe and a cosmological constant. *The Astronomical Journal*, 116(3):1009–1038, September 1998.

[49] J. C. N. de Araujo. The dark energy–dominated universe. *Astroparticle Physics*, 23(2):279–286, March 2005.

[50] N. Aghanim et al. Planck 2018 results. *Astronomy and Astrophysics*, 641:A6, September 2020.

[51] S. Dodelson. *Modern Cosmology*. Academic Press, Elsevier Science, 2003.

[52] D. J. Fixsen. The temperature of the cosmic microwave background. *The Astrophysical Journal*, 707(2):916–920, November 2009.

[53] G. Mangano, G. Miele, S. Pastor, and M. Peloso. A precision calculation of the effective number of cosmological neutrinos. *Physics Letters B*, 534(1-4):8–16, May 2002.

[54] G. Mangano, G. Miele, S. Pastor, T. Pinto, O. Pisanti, and P. D. Serpico. Relic neutrino decoupling including flavour oscillations. *Nuclear Physics B*, 729(1-2):221–234, November 2005.

[55] M. White, D. Scott, and J. Silk. Anisotropies in the Cosmic Microwave Background. *Annual Review of Astronomy and Astrophysics*, 32(1):319–370, 1994.

[56] E. Lifshitz. Republication of: On the gravitational stability of the expanding universe. *J. Phys. (USSR)*, 10(2):116, 1946.

[57] P. J. E. Peebles and J. T. Yu. Primeval adiabatic perturbation in an expanding universe. *Astrophys. J. 162: 815-36(December 1970).*

[58] M. Sasaki, T. Tanaka, and K. Yamamoto. Euclidean vacuum mode functions for a scalar field on open de sitter space. *Physical Review D*, 51(6):2979–2995, March 1995.

[59] U. Seljak and M. Zaldarriaga. A line-of-sight integration approach to cosmic microwave background anisotropies. *The Astrophysical Journal*, 469:437, October 1996.

[60] A. Lewis and S. Bridle. Cosmological parameters from CMB and other data: A Monte Carlo approach. *Physical Review D*, 66(10), November 2002.

[61] D. Blas, J. Lesgourgues, and T. Tram. The cosmic linear anisotropy solving system (CLASS). part II: Approximation schemes. *Journal of Cosmology and Astroparticle Physics*, 2011(07):034–034, July 2011.

[62] G. F. Smoot, M. V. Gorenstein, and R. A. Muller. Detection of anisotropy in the cosmic blackbody radiation. *Phys. Rev. Lett.*, 39:898–901, October 1977.

[63] G. F. Smoot and P. M. Lubin. Southern hemisphere measurements of the anisotropy in the cosmic microwave background radiation. *The Astrophysical Journal Letters*, 234:L83–L86, 1979.

[64] E. S. Cheng, P. R. Saulson, D. T. Wilkinson, and B. E. Corey. Large-scale anisotropy in the 2.7K radiation. *The Astrophysical Journal Letters*, 232:L139–L143, 1979.

[65] G. F. Smoot et al. Structure in the COBE Differential Microwave Radiometer First-Year Maps. *The Astrophysical Journal Letters*, 396:L1, 1992.

[66] Nobel Prize Outreach AB 2022. The Nobel Prize in Physics. https://www.nobelprize.org/prizes/physics/2006/summary/, 2006.

[67] C. L. Bennett et al. First-year wilkinson microwave anisotropy probe (WMAP) observations: Preliminary maps and basic results. *The Astrophysical Journal Supplement Series*, 148(1):1–27, September 2003.

[68] D. N. Spergel et al. First-year wilkinson microwave anisotropy probe (WMAP) observations: Determination of cosmological parameters. *The Astrophysical Journal Supplement Series*, 148(1):175–194, September 2003.

[69] The Planck Collaboration. The Scientific Programme of Planck. *arXiv: 0604069*, 2006.

[70] Planck 2013 results. I. Overview of products and scientific results. *Astronomy & Astrophysics*, 571:A1, October 2014.

[71] A. G. Riess et al. A Comprehensive Measurement of the Local Value of the Hubble Constant with 1 km $s^{-1}Mpc^{-1}$ Uncertainty from the Hubble Space Telescope and the SH0ES Team. *The Astrophysical Journal Letters*, 934(1):L7, July 2022.

[72] C. Heymans et al. KiDS-1000 cosmology: Multi-probe weak gravitational lensing and spectroscopic galaxy clustering constraints. *Astronomy & Astrophysics*, 646:A140, February 2021.

[73] M. Asgari et al. KiDS-1000 cosmology: Cosmic shear constraints and comparison between two point statistics. *Astronomy & Astrophysics*, 645:A104, January 2021.

[74] T. M. C. Abbott et al. Dark energy survey year 3 results: Cosmological constraints from galaxy clustering and weak lensing. *Physical Review D*, 105(2), January 2022.

[75] E. Di Valentino, A. Melchiorri, and J. Silk. Planck evidence for a closed universe and a possible crisis for cosmology. *Nature Astronomy*, 4(2):196–203, November 2019.

[76] E. Di Valentino, A. Melchiorri, and J. Silk. Beyond six parameters. *Physical Review D*, 92(12), December 2015.

[77] DES Collaboration, T. M. C. Abbott, et al. Dark Energy Survey Year 3 Results: Constraints on extensions to ΛCDM with weak lensing and galaxy clustering, 2022.

[78] R. H. Dicke. Gravitation and the universe. *Philadelphia: American Philosophical Society*, November 1969.

[79] B. Acharya et al. Magnetic monopole search with the full MoEDAL trapping detector in 13 TeV. *Physical Review Letters*, 123(2), July 2019.

[80] G. Aad and B. Abbott. Search for magnetic monopoles and stable high-electric-charge objects in 13 tev proton-proton collisions with the ATLAS detector. *Physical Review Letters*, 124(3), January 2020.

[81] A. H. Guth and S. H. H. Tye. Phase transitions and magnetic monopole production in the very early universe. *Phys. Rev. Lett.*, 44:631–635, March 1980.

[82] A. H. Guth. Inflationary universe: A possible solution to the horizon and flatness problems. *Phys. Rev. D*, 23:347–356, January 1981.

[83] A. A. Starobinskii. Spectrum of relict gravitational radiation and the early state of the universe. *ZhETF Pisma Redaktsiiu*, 30:719–723, 1979.

[84] A.D. Linde. A new inflationary universe scenario: A possible solution of the horizon, flatness, homogeneity, isotropy and primordial monopole problems. *Physics Letters B*, 108(6):389–393, 1982.

[85] A. Albrecht and P. J. Steinhardt. Cosmology for grand unified theories with radiatively induced symmetry breaking. *Phys. Rev. Lett.*, 48:1220–1223, April 1982.

[86] Dirac Medal. https://www.ictp.it/about-ictp/prizes-awards/the-dirac-medal/the-medallists/dirac-medallists-2002.aspx, 2002.

[87] The Breakthrough Prize. https://breakthroughprize.org/Laureates/1/P1/Y2012, 2012.

[88] The Kavli Prize. https://www.kavliprize.org/prizes/astrophysics/2014, 2014.

[89] V. F. Mukhanov and G. V. Chibisov. Quantum Fluctuations and a Nonsingular Universe. *JETP Lett.*, 33:532–535, 1981.

[90] W. H. Kinney. TASI Lectures on Inflation. *arXiv: 0902.1529*, 2009.

[91] L. Senatore. Lectures on Inflation. In *New Frontiers in Fields and Strings*. World Scientific, November 2016.

[92] G. N. Remmen and S. M. Carroll. How many e-folds should we expect from high-scale inflation? *Physical Review D*, 90(6), September 2014.

[93] S. Alam et al. Completed SDSS-IV extended Baryon Oscillation Spectroscopic Survey: Cosmological implications from two decades of spectroscopic surveys at the Apache Point Observatory. *Physical Review D*, 103(8):083533, 2021.

[94] D. Scolnic et al. The Pantheon+ Analysis: The Full Data Set and Light-curve Release. *The Astrophysical Journal*, 938(2):113, October 2022.

[95] A. G. Riess, S. Casertano, W. Yuan, J. B. Bowers, L. Macri, J. C. Zinn, and D. Scolnic. Cosmic Distances Calibrated to 1% Precision with Gaia EDR3 Parallaxes and Hubble Space Telescope Photometry of 75 Milky Way Cepheids Confirm Tension with ΛCDM. *The Astrophysical Journal Letters*, 908(1):L6, February 2021.

[96] A. G. Riess, S. Casertano, W. Yuan, L. M. Macri, and D. Scolnic. Large Magellanic Cloud Cepheid Standards Provide a 1% Foundation for the Determination of the Hubble Constant and Stronger Evidence for Physics beyond ΛCDM. *The Astrophysical Journal*, 876(1):85, May 2019.

[97] E. Di Valentino et al. In the realm of the Hubble tension - a review of solutions. *Classical and Quantum Gravity*, 38(15):153001, July 2021.

[98] J. Schaffer. What not to multiply without necessity. *Australasian Journal of Philosophy*, 93(4):644–664, 2015.

[99] A. Linde. Can we have inflation with $\Omega > 1$? *Journal of Cosmology and Astroparticle Physics*, 2003(05):002–002, May 2003.

[100] G. Efstathiou and S. Gratton. The evidence for a spatially flat universe. *Monthly Notices of the Royal Astronomical Society: Letters*, 496(1):L91–L95, May 2020.

[101] T. D. Brandt. Constraints on MACHO dark matter from compact stellar systems in ultra-faint dwarf galaxies. *The Astrophysical Journal*, 824(2):L31, June 2016.

[102] A. Del Popolo. Non-baryonic dark matter in cosmology. *International Journal of Modern Physics D*, 23(03):1430005, February 2014.

[103] Lord Kelvin. Baltimore Lectures on Molecular Dynamics and the Wave Theory of Light. *C.J. Clay and Sons*, February 1904.

[104] J. C. Kapteyn. First Attempt at a Theory of the Arrangement and Motion of the Sidereal System. *The Astrophysical Journal*, 55:302, May 1922.

[105] K. Lundmark. Über die Bestimmung der Entfernungen, Dimensionen, Massen und Dichtigkeit fur die nächstgelegenen anagalacktischen Sternsysteme. *Meddelanden fran Lunds Astronomiska Observatorium Serie I*, 125:1–13, 1930.

[106] J. H. Oort. The force exerted by the stellar system in the direction perpendicular to the galactic plane and some related problems. *Bulletin of the Astronomical Institutes of the Netherlands*, 6:249, 1932.

[107] F. Zwicky. Die Rotverschiebung von extragalaktischen Nebeln. *Helvetica Physica Acta*, 6:110–127, 1933.

[108] J. Einasto, A. Kassik, and E. Saar. Dynamic evidence on massive coronas of galaxies. *Nature 250, 309–31*, 1974.

[109] J. P. Ostriker, P. J. E. Peebles, and A. Yahil. The Size and Mass of Galaxies, and the Mass of the Universe. *The Astrophysical Journal Letters*, 193:L1, 1974.

[110] S. M. Faber and J. S. Gallagher. Masses and mass-to-light ratios of galaxies. *Annual Review of Astronomy and Astrophysics*, 17(1):135–187, 1979.

[111] V. Trimble. Existence and nature of dark matter in the universe. *Annual Review of Astronomy and Astrophysics*, 25:425–472, 1987.

[112] S. Cole, S. Hatton, D. H. Weinberg, and C. S. Frenk. Mock 2df and SDSS galaxy redshift surveys. *Monthly Notices of the Royal Astronomical Society*, 300(4):945–966, November 1998.

[113] W. J. Percival et al. The 2dF Galaxy Redshift Survey: the power spectrum and the matter content of the Universe. *Monthly Notices of the Royal Astronomical Society*, 327(4):1297–1306, November 2001.

[114] J. L. Feng. Dark matter candidates from particle physics and methods of detection. *Annual Review of Astronomy and Astrophysics*, 48(1):495–545, August 2010.

[115] S. Dodelson and L. M. Widrow. Sterile neutrinos as dark matter. *Physical Review Letters*, 72(1):17–20, January 1994.

[116] L. D. Duffy and K. van Bibber. Axions as dark matter particles. *New Journal of Physics*, 11(10):105008, October 2009.

[117] L. Roszkowski, E. M. Sessolo, and S. Trojanowski. WIMP dark matter candidates and searches—current status and future prospects. *Reports on Progress in Physics*, 81(6):066201, May 2018.

[118] M. E. Peskin. Dark matter and particle physics. *Journal of the Physical Society of Japan*, 76(11):111017, November 2007.

[119] J. Aalbers et al. First Dark Matter Search Results from the LUX-ZEPLIN (LZ) Experiment. *arXiv: 2207.03764*, 2022.

[120] E. Aprile et al. The XENON1T dark matter experiment. *The European Physical Journal C*, 77(12), December 2017.

[121] A. Tan et al. Dark matter results from first 98.7 days of data from the PandaX-II experiment. *Physical Review Letters*, 117(12), September 2016.

[122] G. Gamow. My World Line: An Informal Autobiography. *Viking Press*, 03 1970.

[123] A. G. Lemaître. A Homogeneous Universe of Constant Mass and Increasing Radius accounting for the Radial Velocity of Extra-galactic Nebulæ. *Monthly Notices of the Royal Astronomical Society*, 91(5):483–490, 03 1931.

[124] H. Kragh. Cosmology and Controversy: The Historical Development of Two Theories of the Universe. *Princeton University Press*, 91(5):483–490, 03 1996.

[125] G. B. Dalrymple. Ancient Earth, Ancient Skies: The Age of Earth and its Cosmic Surroundings. *Stanford University Press*, 03 2004.

[126] A. Sandage. Current Problems in the Extragalactic Distance Scale. *The Astrophysical Journal*, 127:513, May 1958.

[127] B. Chaboyer et al. The Age of Globular Clusters in Light of Hipparcos: Resolving the Age Problem? *The Astrophysical Journal*, 494(96), March 1998.

[128] G. de Vaucouleurs. Five crucial tests of the cosmic distance scale using the Galaxy as fundamental standard. *Nature*, 03 1982.

[129] E. J. Chaisson. The Hubble Wars Astrophysics Meets Astropolitics in the Two-Billion-Dollar Struggle over the Hubble Space Telescope. *Harvard University Press*, 03 1998.

[130] R. C. Tolman. Letter to Einstein. *Albert Einstein Archives, 23-031*, 03 1931.

[131] A. S. Eddington and E. T. Whittaker. *Fundamental Theory*. The University Press, 1946.

[132] W. Lenz. Das Gleichgewicht von Materie und Strahlung in Einsteins geschlossener. *Physikalische Zeitschrift*, 27(642–645), March 1926.

[133] Ya. B. Zel'dovich. The cosmological constant and the theory of elementary particles. *Soviet Physics Uspekhi*, 11(3):381, March 1968.

[134] M. P. Hobson, G. P. Efstathiou, and A. N. Lasenby. General relativity: An introduction for physicists. *Cambridge University Press*, March 2006.

[135] R. J. Adler, B. Casey, and O. C. Jacob. Vacuum catastrophe: An elementary exposition of the cosmological constant problem. *American Journal of Physics*, 63(7):620–626, 1995.

[136] G. R. Bengochea, G. León, E. Okon, and D. Sudarsky. Can the quantum vacuum fluctuations really solve the cosmological constant problem? *The European Physical Journal C*, 80(1), January 2020.

[137] Q. Wang, Z. Zhu, and W. G. Unruh. How the huge energy of quantum vacuum gravitates to drive the slow accelerating expansion of the universe. *Physical Review D*, 95(10), May 2017.

[138] T. Aoyama, M. Hayakawa, T. Kinoshita, and M. Nio. Tenth-order electron anomalous magnetic moment: Contribution of diagrams without closed lepton loops. *Physical Review D*, 91(3), February 2015.

[139] E. Asmodelle. Tests of general relativity: A review. *arXiv: 1705.04397*, 2017.

[140] C. P. Burgess. The cosmological constant problem: Why it's hard to get dark energy from micro-physics. *arXiv: 1309.4133*, 2013.

[141] S. Weinberg. The cosmological constant problem. *Rev. Mod. Phys.*, 61:1–23, January 1989.

[142] S. M. Carroll. The cosmological constant. *Living Reviews in Relativity*, 4(1), February 2001.

[143] P. Binétruy. Cosmological Constant Versus Quintessence. *International Journal of Theoretical Physics*, 39(7):1859–1875, 2000.

[144] T. Padmanabhan. Cosmological constant—the weight of the vacuum. *Physics Reports*, 380(5-6):235–320, July 2003.

[145] J. A. Frieman, M. S. Turner, and D. Huterer. Dark energy and the accelerating universe. *Annual Review of Astronomy and Astrophysics*, 46(1):385–432, September 2008.

[146] B. Carter. Confrontation of cosmological theories with observational data. *International Astronomical Union Symposia,*, November 1974.

[147] B. Carter. Large number coincidences and the anthropic principle in cosmology. *Annual Reviews*, 1974.

[148] Editors of Encyclopaedia Britannica. The Anthropic Principle. *Encyclopedia Britannica*, 2022.

[149] S. Weinberg. Anthropic bound on the cosmological constant. *Phys. Rev. Lett.*, 59:2607–2610, November 1987.

[150] J. Yoo and Y. Watanabe. Theoretical models of dark energy. *International Journal of Modern Physics D*, 21(12):1230002, November 2012.

[151] B. Ratra and P. J. E. Peebles. Cosmological consequences of a rolling homogeneous scalar field. *Phys. Rev. D*, 37:3406–3427, June 1988.

[152] C. Wetterich. Cosmology and the fate of dilatation symmetry. *Nuclear Physics B*, 302(4):668–696, 1988.

[153] R. R. Caldwell, R. Dave, and P. J. Steinhardt. Cosmological imprint of an energy component with general equation of state. *Physical Review Letters*, 80(8):1582–1585, February 1998.

[154] V. Sahni. The cosmological constant problem and quintessence. *Classical and Quantum Gravity*, 19(13):3435–3448, June 2002.

[155] S. M. Carroll. Quintessence and the rest of the world: Suppressing long-range interactions. *Physical Review Letters*, 81(15):3067–3070, October 1998.

[156] P. J. E. Peebles and B. Ratra. The cosmological constant and dark energy. *Reviews of Modern Physics*, 75(2):559–606, April 2003.

[157] H. Y. Ip, J. Sakstein, and F. Schmidt. Solar system constraints on disformal gravity theories. *Journal of Cosmology and Astroparticle Physics*, 2015(10):051–051, October 2015.

[158] P. Brax, C. Burrage, and C. Englert. Disformal dark energy at colliders. *Physical Review D*, 92(4), August 2015.

[159] P. Brax, C. Burrage, C. Englert, and M. Spannowsky. LHC signatures of scalar dark energy. *Physical Review D*, 94(8), October 2016.

[160] B. J. Barros, L. Amendola, T. Barreiro, and N. J. Nunes. Coupled quintessence with a ΛCDM background: removing the σ_8 tension. *Journal of Cosmology and Astroparticle Physics*, 2019(01):007–007, January 2019.

[161] L. P. Chimento, A. S. Jakubi, D. Pavón, and W. Zimdahl. Interacting quintessence solution to the coincidence problem. *Physical Review D*, 67(8), April 2003.

[162] L. Amendola. Coupled quintessence. *Physical Review D*, 62(4), July 2000.

[163] E. Di Valentino, A. Melchiorri, O. Mena, and S. Vagnozzi. Interacting dark energy in the early 2020s. *Physics of the Dark Universe*, 30:100666, December 2020.

[164] G. Mangano, G. Miele, and V. Pettorino. Coupled quintessence and the coincidence problem. *Modern Physics Letters A*, 18(12):831–842, April 2003.

[165] S. Tsujikawa. Quintessence: a review. *Classical and Quantum Gravity*, 30(21):214003, October 2013.

[166] T. Rudelius. Asymptotic scalar field cosmology in string theory. *Journal of High Energy Physics*, 2022(10), October 2022.

[167] F. Rosati. Supersymmetric quintessence. *arXiv: 9906427*, 1999.

[168] K. Dutta and L. Sorbo. Confronting pseudo-Nambu-Goldstone-boson quintessence with data. *Phys. Rev. D*, 75:063514, March 2007.

[169] S. Chakraborty, N. C. Chakraborty, and U. Debnath. Quintessence Problem and Brans-Dicke Theory. *Modern Physics Letters A*, 18(22):1549–1555, July 2003.

[170] C. Wetterich. The cosmon model for an asymptotically vanishing time-dependent cosmological "constant". *arXiv: 9408025*, 1994.

[171] Y. Fujii and K. Maeda. The scalar-tensor theory of gravitation. *Class. Quantum Grav*, 2003.

[172] W. Scherrer. Zur theorie der elementarteilchen. *Verhandlungen der Schweizer Naturforschenden Gesellschaft*, 1941.

[173] P. Jordan. Zur projektiven relativitatstheori. *Nachrichten der Akademie der Wissenschaften, Mathematisch-Physikalische Klasse*, 1945.

[174] P. A. M. Dirac. The Cosmological Constants. *Nature*, 1937.

[175] P. A. M. Dirac. A New Basis for Cosmology. *Royal Society of London*, 1938.

[176] J. M. Overduin and P. S. Wesson. Kaluza-Klein gravity. *Physics Reports*, 283(5-6):303–378, April 1997.

[177] B. Fauser. Projective relativity: Present status and outlook. *General Relativity and Gravitation*, 33(5):875–887, May 2001.

[178] A. Lichnerowicz and Y. Thiry. Probl'emes de calcul des variations li es a la dynamique classique et a la theorie unitaire du cha. *Comptes Rendus de l'Academie des Sciences, 224, 529-531*, 1947.

[179] Y. Thiry. Les equations de la theorie unitaire de Kaluzcha. *Comptes rendus de l'Academie des Sciences, 226, 216-218*, 1948.

[180] Y. Thiry. Sur la regularite des champs gravitationels et electromagnetiques dans les theories unitaiha. *Comptes Rendus de l'Academie des Sciences, 226, 1881-1882*, 1948.

[181] C. Brans and R. H. Dicke. Mach's principle and a relativistic theory of gravitation. *Physical Review 124, 925-935*, 1961.

[182] G. Ludwig and Cl. Mullee. Ein Modell des Kosmos und der Sternentstehung. *Annalen der Physik Ser. 6, 2, 76-84*, 1948.

[183] G. Ludwig and Cl. Mullee. Ein Modell des Kosmos und der Sternentstehung. *Archiv der Mathematik 1 (1), 80-82*, 1948.

[184] I. Quiros, R. García-Salcedo, J. E. Madriz-Aguilar, and T. Matos. The conformal transformation's controversy: what are we missing? *General Relativity and Gravitation*, 45(2):489–518, November 2012.

[185] V. Faraoni and E. Gunzig. Einstein frame or Jordan frame? *arXiv: 9910176*, 1999.

[186] C. M. Will. The confrontation between general relativity and experiment. *Living Reviews in Relativity*, 4(1), May 2001.

[187] B. Wang, E. Abdalla, F. Atrio-Barandela, and D. Pavón. Dark matter and dark energy interactions: theoretical challenges, cosmological implications and observational signatures. *Reports on Progress in Physics*, 79(9):096901, August 2016.

[188] C. van de Bruck and J. Morrice. Disformal couplings and the dark sector of the universe. *Journal of Cosmology and Astroparticle Physics*, 2015(04):036–036, April 2015.

[189] C. van de Bruck and G. Sculthorpe. Modified gravity and the radiation dominated epoch. *Physical Review D*, 87(4), February 2013.

[190] C. Ma and E. Bertschinger. Cosmological perturbation theory in the synchronous and conformal newtonian gauges. *The Astrophysical Journal*, 455:7, December 1995.

[191] H. Kurki-Suonio. Cosmological Perturbation Theory I. https://www.mv.helsinki.fi/home/hkurkisu/CosPer.pdf, June 2022.

[192] L. Amendola. Linear and nonlinear perturbations in dark energy models. *Physical Review D*, 69(10), May 2004.

[193] J. Mifsud and C. van de Bruck. Probing the imprints of generalized interacting dark energy on the growth of perturbations. *Journal of Cosmology and Astroparticle Physics*, 2017(11):001–001, November 2017.

[194] V. F. Mukhanov, H. A. Feldman, and R. H. Brandenberger. Theory of cosmological perturbations. Part 1. Classical perturbations. Part 2. Quantum theory of perturbations. Part 3. Extensions. *Phys. Rept.*, 215:203–333, 1992.

[195] L. Amendola. Linear and nonlinear perturbations in dark energy models. *Physical Review D*, 69(10), May 2004.

[196] M. Zumalacárregui, T. S. Koivisto, and D. F. Mota. DBI Galileons in the Einstein frame: Local gravity and cosmology. *Physical Review D*, 87(8), April 2013.

[197] I. Dalianis and F. Farakos. Exponential potential for an inflaton with nonminimal kinetic coupling and its supergravity embedding. *Physical Review D*, 90(8), October 2014.

[198] A. Kehagias. Exponential and power-law hierarchies from supergravity. *Physics Letters B*, 469(1-4):123–128, December 1999.

[199] T. Barreiro, E. J. Copeland, and N. J. Nunes. Quintessence arising from exponential potentials. *Physical Review D*, 61(12), May 2000.

[200] S. Das, P. S. Corasaniti, and J. Khoury. Superacceleration as the signature of a dark sector interaction. *Phys. Rev. D*, 73:083509, April 2006.

[201] F. S. N. Lobo. Phantom energy traversable wormholes. *Physical Review D*, 71(8), April 2005.

[202] J. A. Vázquez, M. Bridges, M. P. Hobson, and A. N. Lasenby. Reconstruction of the dark energy equation of state. *Journal of Cosmology and Astroparticle Physics*, 2012(09):020–020, September 2012.

[203] R. K. Sachs and A. M. Wolfe. Perturbations of a Cosmological Model and Angular Variations of the Microwave Background. *The Astrophysical Journal*, 147:73, 1967.

[204] T. de Haan et al. Cosmological constraints from galaxy clusters in the 2500 square-degree SPT-SZ survey. *The Astrophysical Journal*, 832(1):95, November 2016.

[205] W. Zimdahl, D. Pavón, and L. P. Chimento. Interacting quintessence. *Physics Letters B*, 521(3-4):133–138, November 2001.

[206] G. R. Farrar and P. J. E. Peebles. Interacting dark matter and dark energy. *The Astrophysical Journal*, 604(1):1–11, March 2004.

[207] T. Koivisto. Growth of perturbations in dark matter coupled with quintessence. *Physical Review D*, 72(4), August 2005.

[208] E. J. Copeland, M. Sami, and S. Tsujikawa. Dynamics of dark energy. *International Journal of Modern Physics D*, 15(11):1753–1935, November 2006.

[209] Z. Guo, N. Ohta, and S. Tsujikawa. Probing the coupling between dark components of the universe. *Physical Review D*, 76(2), July 2007.

[210] A. W. Brookfield, C. van de Bruck, and L. M. H. Hall. New interactions in the dark sector mediated by dark energy. *Physical Review D*, 77(4), February 2008.

[211] E. R. M. Tarrant, C. van de Bruck, E. J. Copeland, and A. M. Green. Coupled quintessence and the halo mass function. *Physical Review D*, 85(2), January 2012.

[212] A. Pourtsidou, C. Skordis, and E. J. Copeland. Models of dark matter coupled to dark energy. *Physical Review D*, 88(8), October 2013.

[213] J. Gleyzes, D. Langlois, M. Mancarella, and F. Vernizzi. Effective theory of interacting dark energy. *Journal of Cosmology and Astroparticle Physics*, 2015(08):054–054, August 2015.

[214] C. Skordis, A. Pourtsidou, and E. J. Copeland. Parametrized post-Friedmannian framework for interacting dark energy theories. *Physical Review D*, 91(8), April 2015.

[215] C. van de Bruck, J. Mifsud, and J. Morrice. Testing coupled dark energy models with their cosmological background evolution. *Physical Review D*, 95(4), February 2017.

[216] O. Lahav and A. R. Liddle. The Cosmological Parameters. *arXiv: 2201.08666*, 2022.

[217] P. J. E. Peebles and B. Ratra. Cosmology with a Time-Variable Cosmological "Constant". *The Astrophysical Journal Letters*, 325:L17, 1988.

[218] P. J. Steinhardt, L. Wang, and I. Zlatev. Cosmological tracking solutions. *Physical Review D*, 59(12), May 1999.

[219] P. Binétruy. Models of dynamical supersymmetry breaking and quintessence. *Phys. Rev. D*, 60:063502, August 1999.

[220] T. Brinckmann and J. Lesgourgues. MontePython 3: boosted MCMC sampler and other features. *arXiv: 1804.07261*, 2018.

[221] B. Audren, J. Lesgourgues, K. Benabed, and S. Prunet. Conservative Constraints on Early Cosmology: an illustration of the Monte Python cosmological parameter inference code. *Journal of Cosmology and Astroparticle Physics*, 1302:001, 2013.

[222] A. Lewis. GetDist: a Python package for analysing Monte Carlo samples. *arXiv: 1910.13970*, 2019.

[223] A. Heavens, Y. Fantaye, A. Mootoovaloo, H. Eggers, Z. Hosenie, S. Kroon, and E. Sellentin. Marginal Likelihoods from Monte Carlo Markov Chains. *arXiv: 1704.03472*, 2017.

[224] R. Trotta. Bayes in the sky: Bayesian inference and model selection in cosmology. *Contemporary Physics*, 49(2):71–104, March 2008.

[225] S. Nesseris and J. García-Bellido. Is the Jeffreys' scale a reliable tool for Bayesian model comparison in cosmology? *Journal of Cosmology and Astroparticle Physics*, 2013(08):036–036, August 2013.

[226] B. A. Bassett and R. Hlozek. Baryon Acoustic Oscillations. *arXiv: 0910.5224*, 2009.

[227] S. Alam et al. The clustering of galaxies in the completed SDSS-III baryon oscillation spectroscopic survey: cosmological analysis of the DR12 galaxy sample. *Monthly Notices of the Royal Astronomical Society*, 470(3):2617–2652, March 2017.

[228] F. Beutler, C. Blake, M. Colless, D. H. Jones, L. Staveley-Smith, L. Campbell, Q. Parker, W. Saunders, and F. Watson. The 6df galaxy survey: baryon acoustic oscillations and the local hubble constant. *Monthly Notices of the Royal Astronomical Society*, 416(4):3017–3032, July 2011.

[229] A. J. Ross, L. Samushia, C. Howlett, W. J. Percival, A. Burden, and M. Manera. The clustering of the SDSS DR7 main galaxy sample – i. a 4 per cent distance measure at z = 0.15. *Monthly Notices of the Royal Astronomical Society*, 449(1):835–847, March 2015.

[230] W. M. Wood-Vasey et al. Type ia supernovae are good standard candles in the near infrared: Evidence from PAIRITEL. *The Astrophysical Journal*, 689(1):377–390, December 2008.

[231] H. Hossienkhani, H. Yousefi, and N. Azimi. Effect of low anisotropy on cosmological models by using supernova data. *New Astronomy*, 68:65–75, April 2019.

[232] D. M. Scolnic et al. The complete light-curve sample of spectroscopically confirmed SNe ia from pan-STARRS1 and cosmological constraints from the combined pantheon sample. *The Astrophysical Journal*, 859(2):101, May 2018.

[233] A. Gelman and D. B. Rubin. Inference from Iterative Simulation Using Multiple Sequences. *Statistical Science*, 7:457–472, 1992.

[234] H. Desmond, P. G. Ferreira, G. Lavaux, and J. Jasche. Fifth force constraints from galaxy warps. *Physical Review D*, 98(8), October 2018.

[235] T. Damour and A. M. Polyakov. The string dilation and a least coupling principle. *Nuclear Physics B*, 423(2-3):532–558, July 1994.

[236] T. Damour and A. M. Polyakov. String theory and gravity. *General Relativity and Gravitation*, 26(12):1171–1176, December 1994.

[237] P. Brax, C. van de Bruck, A. C. Davis, and D. Shaw. Dilaton and modified gravity. *Physical Review D*, 82(6), September 2010.

[238] A. A. Sen and S. Sethi. Quintessence model with double exponential potential. *Physics Letters B*, 532(3-4):159–165, April 2002.

[239] A. J. S. Hamilton. Linear redshift distortions: A review. In *Astrophysics and Space Science Library*, pages 185–275. Springer Netherlands, 1998.

[240] A. G. Kim and E. V. Linder. Complementarity of peculiar velocity surveys and redshift space distortions for testing gravity. *Physical Review D*, 101(2), January 2020.

[241] C. Howlett, K. Said, J. R. Lucey, M. Colless, F. Qin, Y. Lai, R. B. Tully, and T. M. Davis. The sloan digital sky survey peculiar velocity catalogue. *Monthly Notices of the Royal Astronomical Society*, 515(1):953–976, June 2022.

[242] L. A. Campbell et al. The 6df galaxy survey: Fundamental plane data. *Monthly Notices of the Royal Astronomical Society*, 443(2):1231–1251, July 2014.

[243] I. Achitouv. New constraints on the linear growth rate using cosmic voids in the SDSS DR12 datasets. *Physical Review D*, 100(12), December 2019.

[244] B. Sagredo, S. Nesseris, and D. Sapone. Internal robustness of growth rate data. *Physical Review D*, 98(8), October 2018.

[245] R. Arjona, J. García-Bellido, and S. Nesseris. Cosmological constraints on nonadiabatic dark energy perturbations. *Physical Review D*, 102(10), November 2020.

[246] W. Yang, M. Shahalam, B. Pal, S. Pan, and A. Wang. Constraints on quintessence scalar field models using cosmological observations. *Physical Review D*, 100(2), July 2019.

[247] E. Di Valentino et al. Cosmology intertwined III. *Astroparticle Physics*, 131:102604, September 2021.

[248] T. Tröster, A. G. Sánchez, M. Asgari, C. Blake, M. Crocce, C. Heymans, H. Hildebrandt, B. Joachimi, S. Joudaki, A. Kannawadi, C. Lin, and A. Wright. Cosmology from large-scale structure. *Astronomy & Astrophysics*, 633:L10, January 2020.

[249] J. A. Keselman, A. Nusser, and P. J. E. Peebles. Cosmology with equivalence principle breaking in the dark sector. *Physical Review D*, 81(6), March 2010.

[250] M. Kesden and M. Kamionkowski. Tidal tails test the equivalence principle in the dark-matter sector. *Physical Review D*, 74(8), October 2006.

[251] M. Baldi. Cold dark matter halos in multi-coupled dark energy cosmologies: structural and statistical properties. *arXiv: 1403.2408*, 2014.

[252] V. Springel, N. Yoshida, and S. D. M. White. GADGET: a code for collisionless and gasdynamical cosmological simulations. *New Astronomy*, 6(2):79–117, April 2001.

[253] M. Baldi, V. Pettorino, G. Robbers, and V. Springel. Hydrodynamical N-body simulations of coupled dark energy cosmologies. *Monthly Notices of the Royal Astronomical Society*, 403(4):1684–1702, April 2010.

[254] S. Gariazzo, E. Di Valentino, O. Mena, and R. C. Nunes. Late-time interacting cosmologies and the hubble constant tension. *Physical Review D*, 106(2), July 2022.

[255] W. J. G. de Blok. The core-cusp problem. *Advances in Astronomy*, 2010:1–14, 2010.

[256] M. Baldi. Time-dependent couplings in the dark sector: from background evolution to non-linear structure formation. *Monthly Notices of the Royal Astronomical Society*, 411(2):1077–1103, November 2010.

[257] H. J. Hortúa, L. Á. García, and L. C. Castaneda. Constraining cosmological parameters from N-body simulations with Variational Bayesian Neural Networks. *arXiv: 2301.03991*, 2023.

[258] C. Llinares, D. F. Mota, and H. A. Winther. ISIS: a new N-body cosmological code with scalar fields based on RAMSES. *Astronomy & Astrophysics*, 562:A78, February 2014.

[259] M. Baldi. Clarifying the effects of interacting dark energy on linear and non-linear structure formation processes. *Monthly Notices of the Royal Astronomical Society*, 414(1):116–128, May 2011.

[260] T. Clemson, K. Koyama, G. Zhao, R. Maartens, and J. Väliviita. Interacting dark energy: Constraints and degeneracies. *Physical Review D*, 85(4), February 2012.

[261] J. Binney and S. Tremaine. *Galactic Dynamics: Second Edition*. Princeton Series in Astrophysics, 2008.

[262] M. Sereno, L. Lovisari, W. Cui, and G. Schellenberger. The thermalization of massive galaxy clusters. *Monthly Notices of the Royal Astronomical Society*, 507(4):5214–5223, August 2021.

[263] R. G. Carlberg, H. K. C. Yee, E. Ellingson, R. Abraham, P. Gravel, S. Morris, and C. J. Pritchet. Galaxy Cluster Virial Masses and Omega. *The Astrophysical Journal*, 462:32, May 1996.

[264] A. V. Macciò, C. Quercellini, R. Mainini, L. Amendola, and S. A. Bonometto. Coupled dark energy: Parameter constraints from N-body simulations. *Physical Review D*, 69(12), June 2004.

[265] C. G. Böhmer, T. Harko, and F. S. N. Lobo. The generalized virial theorem in f(R) gravity. *Journal of Cosmology and Astroparticle Physics*, 2008(03):024, March 2008.

[266] T. Harko and K. S. Cheng. Virial theorem and the dynamics of clusters of galaxies in the brane world models. *Physical Review D*, 76(4), August 2007.

[267] H. C. Plummer. On the problem of distribution in globular star clusters. *Monthly Notices of the Royal Astronomical Society*, 71:460–470, 1911.

[268] S. A. Rodionov and N. Ya. Sotnikova. Optimal choice of the softening length and time step in N-body simulations. *Astronomy Reports*, 49(6):470–476, June 2005.

[269] H. Das, S. Deb, and A. Baruah. Optimal Softening for Gravitational Force Calculations in N-body Dynamics. *The Astrophysical Journal*, 911(2):83, 2021.

[270] P. Mocz. Vectorized N-body code (Python). https://github.com/pmocz/nbody-python/, 2021.

[271] W. Dehnen and J. I. Read. N-body simulations of gravitational dynamics. *The European Physical Journal Plus*, 126(5), May 2011.

[272] D. C. Heggie. Michel Henon's contributions to collisional stellar systems. *arXiv: 1411.4936*, 2014.

[273] V. Springel. The cosmological simulation code GADGET-2. *Monthly Notices of the Royal Astronomical Society*, 364(4):1105–1134, December 2005.

[274] B. Li, G. Zhao, R. Teyssier, and K. Koyama. ECOSMOG: an Efficient COde for Simulating MOdified Gravity. *Journal of Cosmology and Astroparticle Physics*, 2012(01):051–051, January 2012.

[275] R. Scaramella et al. *Euclid* preparation. *Astronomy & Astrophysics*, 662:A112, June 2022.

[276] B. Abolfathi et al. The LSST DESC DC2 Simulated Sky Survey. *The Astrophysical Journal Supplement Series*, 253(1):31, March 2021.

[277] A. Weltman et al. Fundamental physics with the Square Kilometre Array. *Publications of the Astronomical Society of Australia*, 37, 2020.

[278] A. Hammami, C. Llinares, D. F. Mota, and H. A. Winther. Hydrodynamic effects in the symmetron and $f(R)$-gravity models. *Monthly Notices of the Royal Astronomical Society*, 449(4):3635–3644, April 2015.

[279] M. B. Gronke, C. Llinares, and D. F. Mota. Gravitational redshift profiles in the $f(R)$ and symmetron models. *Astronomy & Astrophysics*, 562:A9, January 2014.

[280] A. Terukina, L. Lombriser, K. Yamamoto, D. Bacon, K. Koyama, and R. C. Nichol. Testing chameleon gravity with the Coma cluster. *Journal of Cosmology and Astroparticle Physics*, 2014(04):013–013, April 2014.

[281] N. Mohapi, A. Hees, and J. Larena. Test of the Equivalence Principle in the Dark Sector on Galactic Scales. *Journal of Cosmology and Astroparticle Physics*, 03:032, 2016.